Transmission Electron Microscopy Study of the Two-Dimensional Electron Gas at $SrTiO_3$-Based Oxide Interfaces

by

Sirong Lu

A Dissertation Presented in Partial Fulfillment
of the Requirements for the Degree
Doctor of Philosophy

Approved May 2018 by the
Graduate Supervisory Committee:

David J. Smith, Co-Chair
Martha R. McCartney, Co-Chair
Andrew Chizmeshya
Peter A. Crozier

ARIZONA STATE UNIVERSITY

May 2018

ABSTRACT

The two-dimensional electron gas (2DEG) at $SrTiO_3$-based oxide interfaces has been extensively studied recently for its high carrier density, high electron mobility, superconducting, ferromagnetic, ferrroelectric and magnetoresistance properties, with possible application for all-oxide devices. Understanding the mechanisms behind the 2DEG formation and factors affecting its properties is the primary objective of this dissertation.

Advanced electron microscopy techniques, including aberration-corrected electron microscopy and electron energy-loss spectroscopy (EELS) with energy-loss near-edge structure (ELNES) analysis, were used to characterize the interfaces. Image and spectrum data-processing algorithms, including subpixel atomic position measurement, and novel outlier detection by oversampling, subspace division based EELS background removal and bias-free endmember extraction algorithms for hyperspectral unmixing and mapping were heavily used. Results were compared with density functional theory (DFT) calculations for theoretical explanation.

For the γ-$Al_2O_3/SrTiO_3$ system, negative-Cs imaging confirmed the formation of crystalline γ-Al_2O_3. ELNES hyperspectral unmixing combined with DFT calculations revealed that oxygen vacancies, rather than polar discontinuity, were the key to the 2DEG formation. The critical thickness can be explained by shift of the Fermi level due to Ti outdiffusion from the substrate to the film.

At the $LaTiO_3/SrTiO_3$ interface, aberration-corrected imaging showed crystallinity deterioration in $LaTiO_3$ films a few unit cells away from the interface. ELNES showed that oxygen annealing did not alter the crystallinity but converted Ti^{3+} near the interface into Ti^{4+}, which explained disappearance of the conductivity.

At the $EuO/SrTiO_3$ interface, both high-resolution imaging and ELNES confirmed

EuO formation. ELNES hyperspectral unmixing showed a Ti^{3+} layer confined to within several unit cells of the interface on the $SrTiO_3$ side, confirming the presence of oxygen vacancies.

At the $BaTiO_3/SrTiO_3$ interface, spontaneous polarization and lattice parameters were measured directly in each unit cell column and compared with oxidation state mapping using ELNES with unit-cell resolution. The unusually large polarization near the interface and the polarization gradient were explained by oxygen vacancies and the piezoelectric effect due to epitaxial strain and strain gradient from relaxation.

ACKNOWLEDGMENTS

Foremost, I would like to express my sincere gratitude to my advisors, Regents' Professor David J. Smith and Professor Martha R. McCartney, for supporting me in doing advanced microscopy in their group. Under their guidance, I gained a lot of knowledge and experience in electron microscopy. Besides, I learned enthusiasm towards work and the optimistic attitude towards life.

Besides my advisors, I would like to thank the rest of my committee: Prof. Peter A. Crozier and Prof. Andrew Chizmeshya, for very helpful discussions during my research and their insightful comments, suggestions and questions.

My sincere thanks also goes to our collaborators Prof. Alexander A. Demkov, Prof. John G. Ekerdt, Dr. Agham Posadas, Kristy J. Kormondy, Thong Q. Ngo, Patrick Ponath and Bryce Edmondson in UT-Austin, for providing samples in this dissertation research and very helpful discussions on thin film growth. Also, thanks Prof. Xuan P. A. Gao and Martin D. McDaniel in Case Western Reserve University for providing electrical measurements results. Thanks Lingyuan Gao in UT-Austin for very useful discussions on DFT models. Thanks Dr. Toshihiro Aoki and Hsinwei Wu for electron microscopy experiments. Thanks Zhaofeng Gan for very useful discussions on STEM imaging and electron holography. Thanks Prof. Peter Rez and Tara Boland for very helpful discussions on EELS simulations and DFT calculations.

I appreciate all staff members in Eyring Materials Center in Arizona State University for high resolution electron microscopy experiments. Particular thanks to Mr. Karl Weiss, Dr. Katia March, Dr. Shery Chang for their technical support.

I thank all other members in our research group for help and discussions during my PhD study. I thank AFOSR (contract FA9550-12-10494) for financial support.

I thank my parents for understanding and support all through the years.

TABLE OF CONTENTS

CHAPTER Page

LIST OF TABLES

LIST OF FIGURES

Chapter 1

INTRODUCTION

1.1 Transition Metal Oxides (TMO)

Transition metal oxides have many important physical and electronic properties such as ferromagnetism, magnetoresistance, conductivity, and superconductivity,[1] because electrons in the strongly correlated metal d orbitals are close to the Fermi level and deeply involved in chemical bonding. These d electrons exhabit a wide variety of phenomena such as spin, charge and orbital ordering, metal-insulator transitions, multiferroics, spin-orbit ordering and superconductivity. The electronic structure can be tuned by manipulating the chemical composition and atomic structure.[2] The research of this dissertation has primarily focused on using oxide heterostructures to create a highly conducting layer at oxide-oxide interfaces, especially at the $SrTiO_3$ substrate surface.

The perovskite-type oxides have the chemical formula of ABO_3. They also share the same pseudo-cubic crystal structure with type A atoms at cube corners, type B atoms at body-center positions, and oxygen atoms at face-centered positions. The space group of the perovskite-type oxide structure with highest symmetry is $Pm\bar{3}m$. However, many perovskite-type oxides have different space groups because the ferroelectric distortion, the Jahn-Teller (J-T) distortion and/or octahedral distortion break the $Pm3m$ symmetry.[3]

$SrTiO_3$ is a typical ABO_3 perovskite-type oxide with lattice parameter of 3.905 Å. Figure 1.1(a) shows the cubic unit cell of $SrTiO_3$ in space group $Pm\bar{3}m$.[4]. The

coordination numbers of the Sr^{2+} and Ti^{4+} cations are 12 and 6, respectively. There is an soft optical phonon mode associated with rotation of the TiO_6 octahedra along the z axis. A cubic-to-tetragonal phase transition occurs at 105K. Below 105K, $SrTiO_3$ is in space group $I4/mcm$ and antiferroelectric.[5, 6] Figure 1.1(b) is a schematic diagram showing the antiferrodistortion in tetragonal $SrTiO_3$. $SrTiO_3$ is a band insulator with the Ti^{4+} cations in d^0 configuration. The band gap between the oxygen $2p$ and titanium $3d$ is 3.25eV. However, if $SrTiO_3$ is donor doped (e.g. by oxygen vacancies or Nb), it can become conductive. The Hall mobility of Nb-doped $SrTiO_3$ is up to $2.2 \times 10^4 \mathrm{cm}^2/\mathrm{V} \cdot \mathrm{sec}$ at low temperature, and it is about 4 times larger than $SrTiO_3$ doped with oxygen vacancies. The activation energy of donors introduced by oxygen vacancies is about 0.08eV, but very small in Nb-doped $SrTiO_3$ and the Nb donor remains fully ionized down to 1.6K.[7]

Under the octahedral crystal field, the Ti-$3d$ orbitals in cubic $SrTiO_3$, which are in $3d^0$ configuration, split into three degenerate t_{2g} orbitals (d_{xy}, d_{xz} and d_{yz}) at lower energy and two degenerate e_g orbits ($d_{x^2-y^2}$ and $d_{3z^2-r^2}$) at higher energy. Compared with the empty Ti-$3d$ orbitals in bulk $SrTiO_3$, bulk $LaTiO_3$, in which Ti reveals a $3d^1$ configuration, is more complicated. The ground state of bulk $LaTiO_3$ is under some debate. $LaTiO_3$ is a Mott insulator that has G-type anti-ferromagnetic ordering[8] with an ordered magnetic moment of 0.45-0.57μ_B[8–10] below $T_N = 146K$[10]. Under the "Goodenough-Kanamori" framework,[11] in which the orbital occupation is determined by electron-lattice interaction, orbital angular momentum of $3d^1$ configuration is quenched by Jahn-Teller distortion.[10, 12–19] However, a single electron (d^1) with quenched angular momentum should have magnetic moment of $1\mu_B$, which is significantly larger than the experimental value. Considering that the Jahn-Teller coupling in the t_{2g} orbitals is weak, the orbital moment may not be fully quenched,

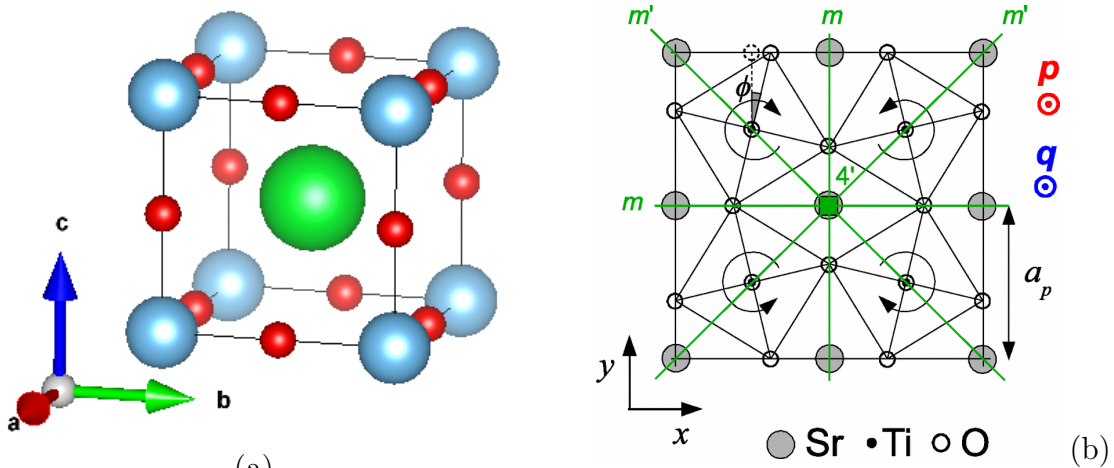

(a) (b)

Figure 1.1. Crystal structure of bulk $SrTiO_3$

(a) The cubic unit cell of $SrTiO_3$. Large green spheres represent Sr atoms. Small red spheres represent O atoms. Blue medium-size spheres represent Ti atoms.

(b) Antiferrodistortive phase of $SrTiO_3$. The neighbouring oxygen octahedra are rotated in opposite directions, resulting in the symmetry elements of the $4'mm$ point group. From Ref.[4].

which reduces the total magnetic moment.[9] An orbital liquid state is proposed for the magnetic ordered phase,[20, 21] as supported by recent RIXS[22] and Raman[23] experiments. Thermo-expansion[13] and Raman shift[24] data indirectly show orbital ordering below T_N. Thermo-conductivity data is interpreted as a transition from orbital liquid to an orbitally ordered phase at T_N.[25]

1.2 Two-Dimensional Electron Gas (2DEG) at Oxide/Oxide Interfaces

Several perovskite-type oxides, including $SrTiO_3$, $LaTiO_3$ and $LaAlO_3$ (band insulator with band gap of 5.5eV), as well as spinel-type oxide γ-Al_2O_3 (band insulator with band gap of 8.7eV), are insulators. However, it has been reported that a layer of conducting two-dimensional electron gas (2DEG) can form at the $LaTiO_3/SrTiO_3$[26],

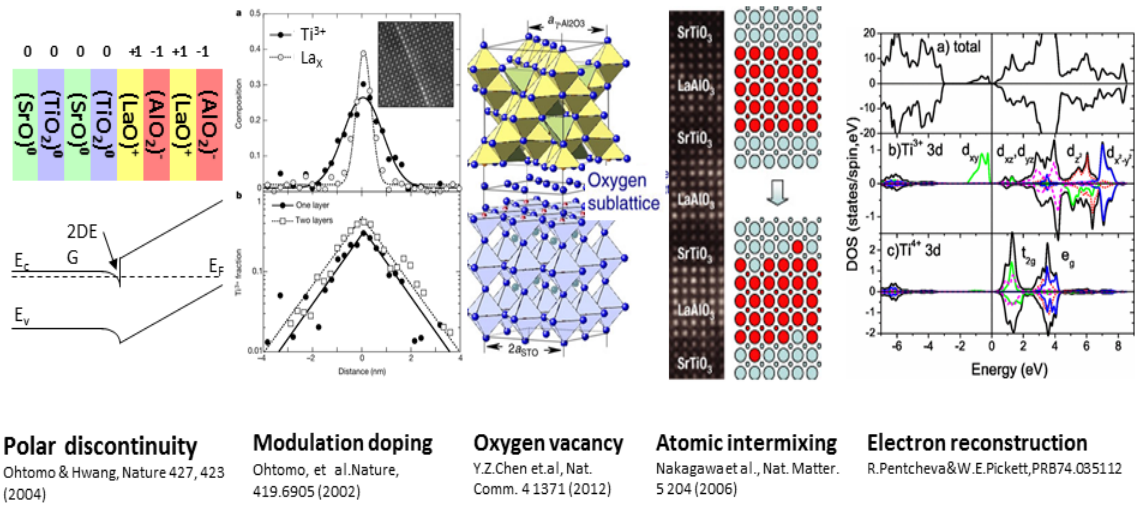

Figure 1.2. Five proposed models for the 2DEG at oxide / oxide interfaces.

(a) Polar discontinuity model.[27] Upper image shows the nominal charge of each atomic layer. Lower image shows the band diagram. The potential diverges unless compensated by a layer of negative charge. (b) Modulation doping.[26] Figure shows the spatial distribution of Ti^{3+} and La across a single $LaTiO_3$ monolayer. The Ti^{3+} signal is significantly wider than that of the La. The y axis is in linear scale in the upper image but logarithmic scale in the lower image. (c) Oxygen vacancies.[28] Blue spheres represents oxygen atoms. Vacancies form between $SrTiO_3$ and γ-Al_2O_3 (d) Atomic intermixing.[29] The figure schematically shows the cation intermixing at $LaAlO_3/SrTiO_3$ interface. The large blue circles, small blue circles, large red circles, small red circles represents Sr, Ti, La and Al, respectively. (e) Electronic reconstruction.[30] The figure shows the density of states of the n-type interface. The upper sub-plot shows the total DOS. The middle sub-plot shows d states of the magnetic Ti^{3+} with split-off d_{xy} band. The lower sub-plot shows the DOS of conventional Ti^{4+}.

$LaAlO_3/SrTiO_3$[27] and γ-$Al_2O_3/SrTiO_3$[28] interfaces. Seeking an understanding of the mechanism(s) behind this conductivity is central to the research of this dissertation.

A 2DEG with very high electron mobility ($10^3 cm^2 V^{-1} s^{-1}$) at low temperature is reported at interfaces with $SrTiO_3$ on one side.[27, 28, 31] The carrier density of the 2DEG is also very high ($\sim 10^{13}$ to $10^{14} cm^{-2}$ at room temperature).[27, 28, 31] In contrast, the sheet-carrier density in semiconductor heterostructures is usually 10^{11} to

10^{12}.[32] The 2DEG at oxide interfaces exhabits a variety of extraordinary electronic properties, such as superconductivity[33–35], colossal magnetoresistance[36, 37] and ferromagnetism[38, 39]. The conductivity can also be tuned by an electric field, and has potential applications to all-oxide devices.[32, 34, 40, 41]

The origins of the 2DEG at oxide interfaces are still heavily debated. Several different models as indicated in Figure 1.2 have been proposed to explain the conductivity at the interface between insulating oxides. It is also possible and quite likely that several mechanisms coexist in one system. In the following section, several material systems exhibiting interfacial 2DEGs are discussed and various models are explained. However, there are still discrepancies between theory and experiment, and there is considerable ongoing debate about which model best explains a specific system.

1.2.1 Polar Catastrophe

$LaAlO_3/SrTiO_3$

The $LaAlO_3/SrTiO_3$ system has attracted much attention. Bulk $LaAlO_3$ is polar. When the $LaAlO_3$ crystal is 'broken' into many (200) mono-layers, it consists of alternating LaO^+ and TiO_2^- layers. Bulk $SrTiO_3$ is non-polar. The pseudo-cubic lattice parameter of $LaAlO_3$ is 3.787 Å, which is 3% smaller than for $SrTiO_3$, but it can be grown coherently on $SrTiO_3$ substrate, as illustrated in Figure 1.3. Experimentally, when polar $LaAlO_3$ is grown on non-polar $SrTiO_3$, the p-type interface (i.e. AlO_2/SrO) is insulating. Only the n-type interface (i.e. LaO/TiO_2)[27] for $LaAlO_3$ films thicker than a critical thickness of ~ 3 unit cells (uc) show conductivity.[40] In addition, when the separation distance between the n-type interface and the p-type interface is less than about six perovskite unit cells of either $LaAlO_3$ or $SrTiO_3$, corresponding to

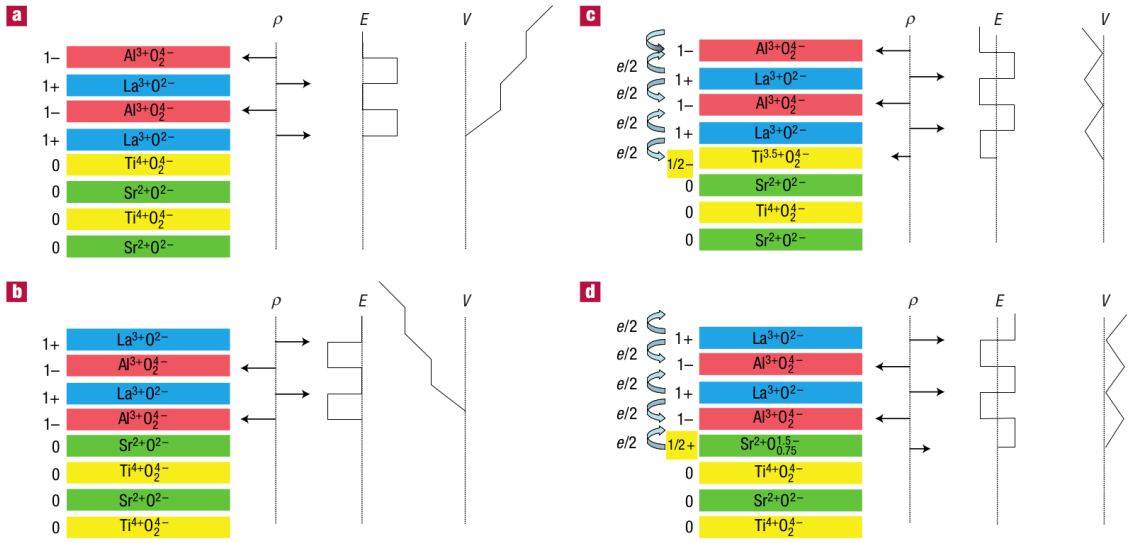

Figure 1.3. The polar catastrophe model illustrated for atomically abrupt (001) interfaces between $LaAlO_3$ and $SrTiO_3$.

(a) Atomically abrupt n-type interface: the potential diverges negatively if there is no compensation. (b) Atomically abrupt p-type interface: the potential diverges positively if there is no compensation. (c) The polar discontinuity can be compensated by transferring 1/2 electrons to each Ti atom. (d) The polar discontinuity can be compensated by introducing 1/4 oxygen vacancies at the interfacial SrO layer. Figure taken from Ref.[29].

approximately 23Å, electronic coupling between the two interface cannot be neglected. The conductivity and carrier density will decrease.[42]

The polar catastrophe model [43, 44] has been used to explain conductivity at this polar-nonpolar interface.[27] The electric potential, and thus the energy, diverges with $LaAlO_3$ film thickness, as shown in Figures 1.3(a) and (b), unless a layer of extra charge is created at the interface to compensate for the polar discontinuity, either by reduction of Ti at the n-type interface (Figure 1.3(c)) or by oxygen vacancies (Figure 1.3(d)) at the p-type interface. Taking into consideration that the band gap of $SrTiO_3$ is relatively small (3.2 eV), and the $LaAlO_3/SrTiO_3$ valence band offset is 0.1eV, DFT calculations show that it takes about 13 Å (four $LaAlO_3$ unit cells) for charge transfer

to occur,[45] which is in reasonable agreement with the experimental value of critical thickness.

Biaxial epitaxial strain may change the polarization of $SrTiO_3$, which in turn could have a strong influence on the 2DEG at the $LaAlO_3/SrTiO_3$ interface. By growing coherently strained single-crystal $SrTiO_3$ on single-crystal substrates with different lattice parameters, it was found that tensile-strained $SrTiO_3$ had no conducting 2DEG, while the carrier density was reduced at the compressively-strained $SrTiO_3$. DFT calculations suggest that compressively-strained $SrTiO_3$ forms <110> polarized nanoscale domains which lead to localization of the carriers in a 2DEG, whereas the tensile-strained $SrTiO_3$ has a ferroelectric-like structural distortion along the <001> direction, which weakens the polar discontinuity.[46]

1.2.2 Charge-Carrier Doping

$LaTiO_3/SrTiO_3$

In the $LaTiO_3/SrTiO_3$ system, the Ti^{3+} in $LaTiO_3$ has the electron configuration of d^1, but it is a Mott-Hubbard insulator due to strong Coulomb repulsion.[47] However, the $LaTiO_3/SrTiO_3$ interface is metallic. Observations using electron-energy-loss spectroscopy (EELS) for a metallic $LaTiO_3/SrTiO_3$ superlattice show that while the oxygen concentration across a single $LaTiO_3$ layer remains unchanged, the width of the Ti^{3+} signal across the same single $LaTiO_3$ layer is larger than that of the La signal.[26] This result indicates that the mechanism is similar to charge modulation doping in semiconductors. DFT+U calculations show that electron reconstruction happens at the interface, and the region near the interface is metallic and ferromagnetic over a wide parameter range.[48] The charge density after considering lattice relaxation agrees

with the experimental results, and the lattice relaxation also shifts the lower Hubbard band upwards.[49] Ferromagnetic orbit ordering may occur at high U values, leading to the insulating phase.[48–50] However, Hall measurements show that the electronic correlation is suppressed at the interface and no ferromagnetism is observed.[51] When La is substituted with rare-earth elements such as Sm or Y, which give more electron correlation[52], the interface is insulating.[53] A superconducting transition at a critical temperature T_c^{onset} ∼300 mK was also reported in this system. The superconducting 2DEG with a typical thickness of 12nm is located mostly on the $SrTiO_3$ side.[35]

1.2.3 Oxygen Vacancies

$\gamma - \mathbf{Al_2O_3/SrTiO_3}$

A high mobility ($1.4 \times 10^5 \mathrm{cm^2V^{-1}s^{-1}}$ at 2K) and high density ($3.7 \times 10^{14} \mathrm{cm^{-2}}$) 2DEG is reported for the γ-$Al_2O_3/SrTiO_3$ system grown by Pulsed Laser Deposition (PLD) at 600°C [28]. Room temperature PLD growth is also achieved, with electron mobility at low temperatures of $3200 \mathrm{cm^2V^{-1}s^{-1}}$, providing an opportunity to design nano-electron oxide devices.[54] Both γ-Al_2O_3 and $SrTiO_3$ are non-polar and γ-Al_2O_3 has no d electrons. This 2DEG is believed to be caused by a chemical redox reaction at the interfaces between $SrTiO_3$ and oxides with large negative enthalpy of formation such as γ-Al_2O_3.[55] It is energetically favorable for oxygen atoms near the interface in $SrTiO_3$ to diffuse out of $SrTiO_3$ and leave oxygen vacancies, which thus create a metallic layer. The oxygen substrate-to-film transfer is experimentally observed for film grown on ^{18}O-exchanged substrate.[56] The Ti^{3+} is confined within a layer of 0.9nm. The conductivity in samples with 8uc γ-Al_2O_3 can survive annealing at 300°C for 24h in 1 bar of pure O_2, but it vanishes in a sample with 2uc γ-Al_2O_3.[28] This

result suggests that oxygen vacancies and the 2DEG are stabilized by an interface effect.[28]

A critical thickness exists in the polar-nonpolar $LaAlO_3/SrTiO_3$ system. However, there also appears to be a critical thickness in the γ-$Al_2O_3/SrTiO_3$ system. The heterostructure is conducting only when the γ-Al_2O_3 film is thicker than approximately 2uc for samples grown at 600°C by PLD. The carrier density and Hall mobility reach maximum values between 2uc to 3uc.[28]. The critical thickness increased to approximately 8uc when sample were grown at room temperature by PLD.[54] A critical thickness between 2.1nm to 4.3nm is also observed in a sample grown by atomic layer deposition (ALD) at 345°C.[57]

As well as oxygen vacancies for the γ-$Al_2O_3/SrTiO_3$ interface, the polar catastrophe mechanism has also been discussed, where the cation site occupancy of the γ-Al_2O_3 structure is taken into account,[58], or by considering γ-Al_2O_3 as a Tasker [59] Type 3 crystal.[60] Despite the fact that this is different from the $LaAlO_3/SrTiO_3$ system [61], no potential gradient has been found in the γ-Al_2O_3 film [60].

$LaAlO_3/SrTiO_3$

Oxygen vacancies were found at both n-type and p-type $LaAlO_3/SrTiO_3$ interfaces by EELS. The oxygen vacancies for n-type interfaces are fewer than for p-type. The oxygen vacancies at p-type interfaces can compensate for the polar catastrophe, while reducing the band offset at n-type interfaces.[29] The effect of growth and annealing conditions were later systematically investigated. Changing the oxygen partial pressure during growth from 10^{-6}mbar to 10^{-4}mbar leads to a carrier density reduction from $\sim 10^{16}\text{cm}^{-2}$ down to $\sim 10^{13}\text{cm}^{-2}$.[62] The conduction in a sample deposited at 10^{-6}mbar was completely dominated by oxygen vacancies.[38] The Shubnikov–de Haas (SdH) oscillations show the 3D character of the conductivity for

deposition with oxygen pressure $P_{O_2} < 10^{-5}$mbar while samples deposited at high oxygen temperature are either insulating or highly resistive.[63] Another SdH oscillation measurement on a sample annealed in 200mbar of O_2 showed 2D character.[64] All these findings showed that oxygen vacancies are also important at the $LaAlO_3/SrTiO_3$ interface.[65]

LDA+U calculations with $U_p = 7$eV and $U_d = 8$eV and without ionic relaxation show that the p-type interface of $LaAlO_3/SrTiO_3$ is insulating and non-magnetic if the polar discontinuity is compensated by oxygen vacancies. These calculations showed that if there are no oxygen vacancies at the interface, the p-type interface is insulating only when a disproportionated, charge-, orbital-, and spin-ordered OP_π magnetic hole is formed.[30] For the n-type interface, several different configurations of oxygen vacancies have been investigated by GGA+U (with $U_{Ti} = 2$eV) calculations with ionic relaxation. A complex multi-orbital reconstruction is produced, which depends strongly on clustering of oxygen vacancies. Oxygen vacancies can create magnetic splitting of the interface d_{xy} orbital.[66]

$SrTiO_3$ surfaces

The 2DEG present at bare $SrTiO_3$ surfaces is similar to the 2DEG at $LaAlO_3/SrTiO_3$ interfaces. In both cases, the Ti $3d_{xy}$ (z is the film growth direction) state of light carriers is the first occupied level. Surface oxygen vacancies may be the origin of the 2DEG.[67] The impurity level introduced by oxygen vacancies on bare $SrTiO_3$ surfaces was investigated by Angle-Resolved Photoemission Spectroscopy (ARPES), and a single deep impurity level was found.[68–70] To explain the donor behavior of oxygen vacancies, GGA+U calculations with U_{eff}=4.36eV were performed and the results were verified using a hybrid functional (HSE06). This work showed that the oxygen vacancies energetically preferred the singly-ionized state V_O^+ rather

than neutral V_O^0 or doubly ionized V_O^{2+}. Thus, a singly occupied localized state in the band gap and a delocalized state in the conduction band were introduced.[71] An oxygen vacancy-based Anderson impurity model taking electron correlation into account has been used to explain the donor behavior of oxygen vacancies.[72]

Other non-polar or amorphous oxide/$SrTiO_3$

It was found recently that a 2DEG exists at the (110) and (111) $LaTiO_3/SrTiO_3$ interfaces,[73] and even at the interfaces between crystalline $SrTiO_3$ and various amorphous insulating overlayers of $LaAlO_3$, $SrTiO_3$ and yttria-stablized zirconia (YSZ) grown at $P_{O_2} \leq 10^{-2}$mbar.[73] No polar discontinuity exists at (110) or amorphous $LaTiO_3/SrTiO_3$ interfaces. This 2DEG can be removed by annealing in 0.5-1 bar pure O_2, suggesting that redox reactions at the $SrTiO_3$ substrate surface play an important role.[74] By ion-milling the overlayer, the insulating state for the oxygen-annealed crystalline $LaAlO_3/SrTiO_3$ heterostructure is restored, but not in the case of the amorphous unannealed structure, suggesting that the polar catastrophe alone accounted for the conductivity for the oxygen-annealed crystalline heterostructure, but both polar catastrophe and oxygen vacancies contributed to the unannealed crystalline heterostructure.[75] The critical thickness for the conductivity depends on the material[74] and the deposition conditions[75]. The critical thickness for the amorphous $LaAlO_3$ layer can be explained by the diffusivity of oxygen in amorphous $LaAlO_3$ being different from crystalline $LaAlO_3$. The interface can be "instantly" oxidized once a sample with a very thin overlayer is exposed to air.[57, 76]

1.2.4 Atomic Intermixing

$LaAlO_3/SrTiO_3$

Diffusion of all four cations into the opposite material near the $LaAlO_3/SrTiO_3$ interface has been observed by several experimental techniques such as EELS [29, 58, 77], Rutherford backscattering spectrometry (RBS) [78], Time-of-Flight Secondary Ion Mass Spectrometry (ToF-SIMS) [78], angle-resolved X-ray photoelectron spectroscopy (XPS) [79] and surface X-ray diffraction (SXRD) [80]. These different types of cation intermixing will affect the electronic structure differently.[81, 82] From both annular-dark-field (ADF) images and EELS maps, the n-type interface is found to be rougher than the p-type interface. A-site atomic intermixing (exchange of Sr and La atoms) across the interface will reduce the dipole introduced by the Ti^{3+}delocalized electron, which prevents the polar catastrophe. There is no delocalized screening electron or hole charge at the p-type interface so there is less cation mixing.[29]

The A site intermixing itself does not remove the polar instability at the n-type interface. However, La substitution for Sr (La_{Sr}) in $SrTiO_3$ is a shallow donor-type defect. Intermixing can form either one or two metallic $La_{1-x}Sr_xTiO_3$ layers, which could be the origin of the 2DEG,[80] or else form a charge neutral $Sr_{1-1.5x}La_xO$ layer, which will compensate the potential buildup for 1-5 uc thin films.[83] Experimentally, the annealed amorphous-$LaAlO_3/SrTiO_3$ interface with La diffused into the $SrTiO_3$ substrate for a depth of about 1.5nm turns out to be insulating.[84] DFT calculations show La_{Sr} defects do not contribute free carriers at p-type and n-type interfaces.[82] In addition, no A site occupancy variance across the interface is found,[58] which is in conflict with the possible formation of $Sr_{1-1.5x}La_xO$.

The La/Ti ratio also plays a very important role in the conductivity. It was found that the crystalline quality and tetragonality of the $LaAlO_3$ films decreased with increasing La/Al ratio.[85] Moreover, the conducting interface only exists in La-deficient or Al-excess films,[86] which requires that the La/Al ratio $\leq 0.97 \pm$

0.03. STEM-EELS shows that the A site (La + Sr) cation occupancy in both La-rich and Al-rich samples does not show variation across the interface. However, there is a dip in the B site (Al + Ti) occupancy at the interface in the La-rich sample, indicating that B site vacancies accumulate at the interface. On the contrary, there is no B-site occupancy variance in the Al-rich sample.[58] DFT calculations were used to determine the energetically favored defect structure. In the La-rich film, the diverging potential is screened by Al_2O_3-vacancy complexes formed at the interface so electronic reconstruction is no longer required. In the Al-rich film, Al substitutes for La, which does not modify the alternating polarity from stoichiometric $LaAlO_3$ film.[58]. Although A site mixing is at a greater depth,[80] the B site intermixing plays an important role. Al-on-Ti antisite is an electron-trapping defect and will reduce the 2DEG density, while Ti-on-Al antisite defects located on the $LaAlO_3$ side cause the interface magnetic moment. The polar discontinuity across the interface is believed to trigger spontaneous thermodynamic formation of the defects.[82] The different defect energy levels at $LaAlO_3/SrTiO_3$ interface, as illustrated in Figure 1.4, have been summarized.[82].

1.2.5 Electronic Reconstruction

Correlated electrons at the interface may undergo electronic reconstruction analogous to reconstructions in which atomic arrangements at surface or interface are different from the bulk, presenting a electronic phase that is different from that in the bulk.[48]

$LaTiO_3/SrTiO_3$

In the $LaTiO_3/SrTiO_3$ system, DFT+U calculations show that ferromagnetic spin

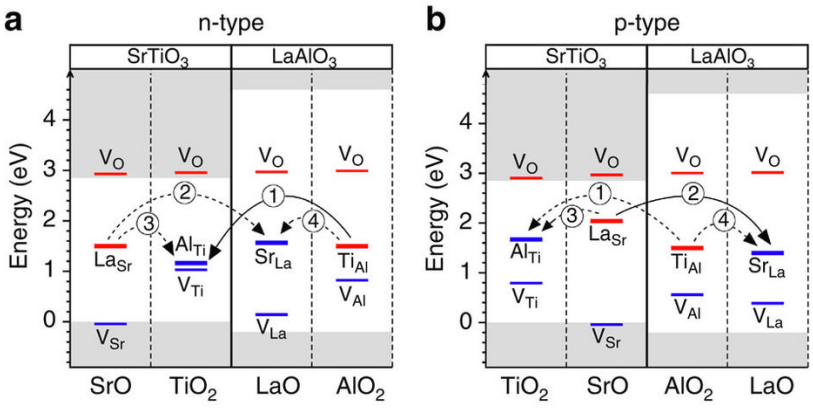

Figure 1.4. Defect energy levels of point defects at $LaAlO_3/SrTiO_3$ interface. ①-④ are four types of donor-acceptor pairs. (a) n-type interface. (b) p-type interface. From Ref[82].

ordering happens at intermediate and large U values, while orbital ordering happens at large U values. In the orbital ordering phase with one LaO layer, d_{xy} orbitals are dominant 2uc away from the interface, although the electron density is low. At both sides of the $LaTiO_3$ layer inside $SrTiO_3$ near the interface, the d_{xz} and d_{yz} orbitals are dominantly occupied, respectively, when not considering atomic relaxation.[48] The d_{xy} orbital is still dominant when considering atomic relaxation.[49]. A small Mott gap also opens up at large U value, separating the lower Hubbard band and resulting in a correlated insulator phase.[50]

Experimentally, the $LaTiO_3/SrTiO_3$ interface undergoes a superconducting transition. The temperature dependence of conductivity measured at critical magnetic fields exhibits a disordered 2D electronic structure,[35] which is different from DFT calculation results using very large U values.[48, 50] Multiple carriers have been reported from the observation of nonlinearity in Hall resistance.[51, 87] Low mobility carriers exist at the interface while the high mobility carriers are present deep in the $SrTiO_3$.[87]. Superconductivity is associated with the high mobility carriers, and can be tuned by the gate voltage.[88]

$LaAlO_3/SrTiO_3$

In the $LaAlO_3/SrTiO_3$ system, LDA+U study shows that t_{2g} degeneracy at the n-type $LaAlO_3/SrTiO_3$ interface is broken by the asymmetry at the interface. The d_{xy} orbital shifts down into the gap. Using U value of 7eV and no ionic relaxation, a charge-ordered ferromagnetic interface is obtained, and the conductivity can be explained by electron hopping on the 50% occupied Ti sublattice with occupied d_{xy} orbitals at checkerboard arranged Ti^{3+} sites.[30] Ionic relaxation is shown to suppress the charge order but d_{xy} orbital occupation remains at the interface layer, and t_{2g} occupation exists in deeper layers after relaxation.[89] Polar catastrophe can also be avoided by relaxation when the $LaAlO_3$ film is thinner than 5 monolayers.[90] The ground state for different U values has also been investigated.[91] Transitions from metal to insulator, non-charge ordering to charge ordering, and non-magnetic to ferromagnetic to antiferromagnetic ordering are observed with U increasing. Coulomb corrections (Hubbard U) were not included in another calculation because they might not properly describe electron correlation in the low carrier density case.[92] This calculation without U correction similarly showed a down-shift of d_{xy} in the first Ti layer at the interface and partial occupation of multiple subbands. Although not showing charge ordering, the lowest conduction band may still not participate in transport because it has a strong 2D character consisting mostly of d_{xy} in the first Ti layer and thus it may be Anderson localized. d_{xz} and d_{yz} may also be localized due to large effective mass along the planar direction. The mobile electron is attributed to electrons in Ti d_{xy} orbitals spreading over several Ti layers. The temperature dependence of sheet resistance varying with the $SrTiO_3$ thickness can also be explained by the Anderson localization model.[93] The d_{xy} preferential occupation is confirmed by X-ray linear dichroism (XLD) measurement[94] and d_{xz}/d_{yz} orbitals

are 50meV above d_{xy} ones.[95]. The measured differences in mobility and density between optical transmission spectroscopy and DC-transport measurement,[96] as well as the differences between the Hall effect and SdH oscillations[64], could be due to multiple channel transport, which also appears in δ-doped $SrTiO_3$.[97] The non-linear Hall effect[98–100] also indicates multiple conducting paths.

The magnetic properties and the superconductivity of the 2DEG are also related to partial occupation of different $3d$ subbands. Ferromagnetism is observed at the $LaAlO_3/SrTiO_3$ interface,[38] even though both materials are non-magnetic in their bulk phase. A possible spiral magnetism is proposed.[101] The ferromagnetism shows Ti^{3+} character in the d_{xy} orbital by XMCD experiments.[39] The ferromagnetism can be quenched by annealing in oxygen, showing a decisive role of oxygen vacancies,[102] which is explained by an oxygen-vacancy-induced orbital reconstruction which lowered the d_{xy} state.[103] The magnetic moment density variation between different samples [104–106] and the enhancement of ferromagnetism for higher oxygen growth pressure [38, 107] is explained by elimination of oxygen vacancies in the bulk region which reduces the depth of itinerant electrons.[108] Superconductivity with $T_c \sim 200mK$ at the interface is also reported.[33] Interestingly, superconductivity and ferromagnetism, which are usually considered to be incompatible, can coexist at the interface.[104, 109, 110] A multi-orbital superconductivity model is proposed and suggests that superconductivity is mainly caused by heavy quasiparticles consisting of d_{yz} and d_{xz}, and the Rashba spin-orbit coupling will stabilize the superconductivity against paramagnetic depairing effects.[111, 112] An electronic phase separation at the $LaAlO_3/SrTiO_3$ interface is reported and directly imaged with a scanning superconducting quantum interference device (SQUID) with micrometer-scale spatial resolution.[113] The interface charge is separated into regions of a quasi-2DEG phase,

a ferromagnetic phase persisting above room temperature or a (superconductor-like) diamagnetic/paramagnetic phase below 60 K.[107]

The conductivity of the 2DEG at $LaAlO_3/SrTiO_3$ interface is limited by different factors at different temperature and magnetic field. The temperature dependence of sheet resistance for samples grown at relatively high partial oxygen pressure is suggested to be a Kondo effect.[38, 114] The Kondo-like scattering is enhanced by increases in the lattice mismatch and growth temperature.[108] The Kondo effect at amorphous-$LaAlO_3/SrTiO_3$ interfaces can be suppressed by light irradiation due to light-induced decoherence of localized spin states.[115] Positive out-of-plane magnetoresistance and negative in-plane magnetoresistance is found at the interface and is explained as spin-orbit interactions becoming stronger when electrons move parallel to the magnetization.[116] As the magnetic field rotates in plane, the magnetoconductance oscillates periodically with angle, which is due to the Rashba spin-orbit term opening and closing a gap at Γ points for the Ti out-of-plane orbitals.[117] Giant negative magnetoresistance at low temperature is explained by the combination of spin-orbit coupling and scattering from finite-range impurities rather than Kondo screening.[118, 119] Colossal positive magnetoresistance (CPMR) is achieved in $SrTiO_3$ capped with low-pressure high-temperature homoepitaxial grown $SrTiO_3/LaAlO_3$ bilayer, and is attributed to the multiple types of carriers and inhomogeneous transport.[37] The tetragonal-to-cubic phase change of $SrTiO_3$ at 105K can affect the conducting path. At low temperature, the conducting path exists at the walls between ferroelectric domains due to enhancement of the polarization. The path also changes with the thermal history of the sample.[120]

The conductivity of $LaAlO_3/SrTiO_3$ interface[33, 121], as well as Nb-doped $SrTiO_3$[122, 123] shows T^2 resistivity at higher temperature, which typically in-

dicates electron-electron scattering. The Fermi-liquid theory is applied to explain the T^2 term.[124] However, the Fermi-liquid model is questioned because of the small Fermi vector and lack of electron reservoir in doped $SrTiO_3$ [125], and the scattering rate showing the independence of carrier density in both doped $SrTiO_3$ and gate controlled $SmTiO_3/SrTiO_3$ interface.[126] The $\rho \propto T^2$ may not be sufficient evidence for electron-electron scattering.[127] At room temperature and higher, the mobility is limited by electron-phonon scattering.[128, 129]

1.2.6 Discussion

The novel functionalities of the 2DEG present at complex oxide-oxide interfaces offers possibilities to design all-oxide electronic devices.[27, 40, 130] This is demonstrated experimentally since the $LaAlO_3/SrTiO_3$ interface can be reversibly switched between insulating and conducting states.[40] The field effect can persist for >24h at room temperature.[41] Switching between superconducting phase and non-magnetic insulating phase [121] and room-temperature control of ferromagnetism [131] are also demonstrated by applying gate voltage. The Rashba spin-orbital coupling and superconductivity can be modulated by controlling the 2DEG subband filling using applied electric field or different crystal orientations.[132–136] Magnetoresistance can be tuned using an applied electric field on the $SrTiO_3$ surface and Kondo effect appears at higher applied gate voltage.[114]

1.3 Outline of Dissertation

Fundamental questions about the 2DEG at complex oxide interfaces are still under much debate, including the discrepancy between the charge density predicted by the simple polar catastrophe model and the measured values, the role of oxygen vacancies and atomic intermixing, the origin of the superconductivity, etc. In this dissertation research, several different types of complex oxide interfaces have been investigated. Electron microscopy is the major experimental tool. Various microscopy and microanalysis techniques have been used, in combination with other experimental methods such as electrical measurements. Image and spectrum simulations, as well as DFT calculations, have also been used in order to compare the experimental results with different theoretical models. The origin and differences of the 2DEGs at complex oxide interfaces investigated is also discussed.

Chapter 2 will introduce the experimental, data analysis and simulation methods used in the dissertation. Both existing and newly developed methods will be described. This chapter will cover the NCSI, HAADF, BF and ABF techniques, image quantification, EELS techniques, ELNES data analysis, and simulation methods which include DFT simulations, image, spectrum and phase simulations.

Chapter 3 will describe the experimental and simulation results and their analysis from γ-$Al_2O_3/SrTiO_3$ interface, The origin of the 2DEG and the physical meaning of the experimental data will be explained.

Chapter 4 will describe the imaging and spectral analysis results for the $LaTiO_3/SrTiO_3$ system. Differences between the as-deposited sample and the oxygen-annealed sample will be discussed and explained.

Chapter 5 will describe the microscopy analysis for the $EuO/SrTiO_3$ interface. Links between the structural, chemical and electrical properties will be discussed.

Chapter 6 will describe the unusually large polarization and polarization gradient found in the $BaTiO_3/SrTiO_3$ system. Different mechanisms are discussed based on simulations and theoretical calculations.

Chapter 2

METHODS

The four apexes of the materials science tetrahedron (MST), are structure, properties, processing and performance, with characterization at the center. Transmission electron microscopy (TEM) is a very powerful tool for characterization since it can provide both structural and chemical information at resolutions down to the sub-Ångstrom scale. In this chapter, several TEM experimental methods used in this research, including high-resolution TEM, high resolution-STEM, EELS and electron holography are discussed. Moreover, since huge amounts of data are collected in modern TEM experiments, related big-data processing methods (mainly hyperspectral unmixing) are also discussed. DFT calculations are also very powerful for simulations at the atomic scale. In this dissertation research, DFT is used to explain the TEM results, and to provide insights into the physics behind the experimental data. Thus, related techniques and further processing of DFT calculations for TEM simulations are introduced in this chapter.

2.1 Transmission Electron Microscopy and Scanning Transmission Electron Microscopy

In this dissertation research, both TEM and STEM have been used. In TEM mode, the specimen is illuminated by a nearly-parallel electron beam. The exit wave is imaged by an objective lens and further magnified. The final image is normally recorded using a doped-YAG screen–coupled CCD camera. In STEM mode, the electron beam is

converged into a small probe which is scanned across the specimen. Electron detectors on the opposite side of the specimen are synchronized with the scanning probe and electrons transmitted at each pixel of the specimen are collected. An image of the specimen is then rebuilt with contrast related to the detector geometry.

2.1.1 Negative Cs Imaging

A very thin specimen is preferred for conventional high-resolution TEM. When the coherent parallel illumination beam passes through the specimen, both the amplitude and the phase are changed. The exit wave is given by

$$f(x,y) = \exp[-i\sigma \int V(x,y,z)dz + \mu(x,y)] \tag{2.1}$$

$$= \exp[-i\sigma V_t(x,y) + \mu(x,y)] \tag{2.2}$$

where (x, y) is a vector in real space, V is the crystal potential, σ is the interaction constant describing the effect of crystal potential on the phase change, μ is the absorption. Since the sample is thin, both the amplitude change (μ) and the phase change $\phi = -\sigma V_t$ are very small.

$$\exp[-i\sigma V_t(x,y)] \approx 1 - i\sigma V_t(x,y) \tag{2.3}$$

$$\exp[\mu(x,y)] \approx 1 + \mu(x,y) \tag{2.4}$$

Then,

$$f(x,y) \approx 1 + \mu(x,y) - i\sigma V_t(x,y) \tag{2.5}$$

The weak-phase-object approximation (WPOA) condition assumes that $\mu(x, y) = 0$ and that σV_t is small. The exit-surface wavefunction under WPOA will not give any image contrast because only the imaginary part of the wavefunction varies with

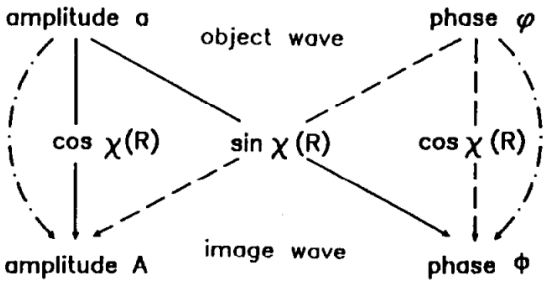

Figure 2.1. Scheme of transfer function from the exit wave to the image plane by means of the aberration $\chi(R)$.

The term $\sin(\chi)$ provides the cross-talk between phase and amplitude. Figure taken from Ref.[137].

position. In order to obtain phase contrast, the amplitude signal should reflect the phase variation of the exit wavefunction.

Fourier transformation of the exit wavefunction then gives,

$$f(\mathbf{u}) = \delta(\mathbf{u}) + \mu(\mathbf{u}) - i\sigma V_t(\mathbf{u}) \tag{2.6}$$

In which $\mathbf{u} = (1/x, 1/y)$. If an extra phase shift $\Delta\phi = \chi(\mathbf{u})$ is added to each non-zero Fourier component of the image (i.e. every diffracted beam), then the final image wavefunction $f'(x, y)$ will have some cross-talk between the real and imaginary part.

$$f'(\mathbf{u}) = \delta(\mathbf{u}) + [\mu(\mathbf{u}) - i\sigma V_t(\mathbf{u})] \exp(-i\chi(\mathbf{u})) \tag{2.7}$$

$$= \delta(\mathbf{u}) + [\mu(\mathbf{u}) - i\sigma V_t(\mathbf{u})](\cos(\chi(\mathbf{u})) - i\sin(\chi(\mathbf{u}))) \tag{2.8}$$

$$= \delta(\mathbf{u}) + \sigma V_t(\mathbf{u})\sin(\chi(\mathbf{u})) + \mu(\mathbf{u})\cos(\chi(\mathbf{u})) - i\sigma V_t(\mathbf{u})\cos(\chi(\mathbf{u})) - i\mu(\mathbf{u})\sin(\chi(\mathbf{u})) \tag{2.9}$$

The desired crosstalk terms between the phase and the amplitude are provided. The relationship is illustrated schematically in Figure 2.1.

In practice, the required phase shift $\Delta\phi$ is provided by the transfer function of the

objective lens. The total transfer function can be represented in the following form.

$$T(\mathbf{u}) = A(\mathbf{u})E(\mathbf{u})e^{-i\chi(\mathbf{u})} \tag{2.10}$$

where $A(\mathbf{u})$ is an aperture function that cuts off all information beyond the boundary of the objective aperture. $E(\mathbf{u})$ is an envelope function, which is the product of several different factors including chromatic aberration, beam divergence, specimen drift, specimen vibration and detector properties. $E(\mathbf{u})$ is close to 1 at low u values but decays rapidly to zero near the information limit of the electron microscope. Both $A(\mathbf{u})$ and $E(\mathbf{u})$ are real functions. The phase shift $\chi(\mathbf{u})$ of the objective lenses is given to a first approximation by

$$\chi(u) = \pi\Delta f\lambda u^2 + \frac{1}{2}\pi C_S\lambda^3 u^4 \tag{2.11}$$

Where Δf is the defocus, C_S is the spherical aberration coefficient of the objective lenses, and λ is the wavelength of the electron beam. C_S has a fixed value at fixed lens current for a conventional TEM. The optimized defocus is obtained by making the variance of the transfer function small. Let

$$\left.\frac{d\chi}{du}\right|_{\chi=-\frac{2\pi}{3}} = 0 \tag{2.12}$$

The so-called Scherzer Focus[138] is then obtained

$$\Delta f_{Sch} = -\left(\frac{4}{3}C_S\lambda\right)^{\frac{1}{2}} \tag{2.13}$$

According to the famous Scherzer Theorem [139] the spherical aberration can be corrected by breaking the rotational symmetry of the objective lens. Aberration correction for TEM can be achieved by using two electromagnetic hexapoles and four additional round lenses.[140]

To maximize information transfer, the steepest ascent of the wave aberration $|d\chi/du|_{max}$ should be minimized in the reciprocal frequency range $[0, u_{max}]$

$$(d\chi/du)|_{u_{min}} = -(d\chi/du)|_{u_{max}} \tag{2.14}$$

where u_{min} and u_{max} are u values at which $d\chi/du$ reaches minimum or maximum (the maximum is taken as the information limit). The optimized defocus under this condition is

$$\Delta f_{Lichte} = -\frac{3}{4} C_S \lambda^2 u_{max}^2 \tag{2.15}$$

This defocus is known as the Lichte defocus, which is also the condition where the image has the least delocalization or least confusion[141], and it was originally used for recording electron holograms.[137] In conventional TEM, C_S is always positive, so both Δf_{Sch} and Δf_{Lichte} are negative (underfocus). Aberration correction makes it possible to control the C_S value over a large range. For aberration-corrected TEM,

$$\Delta f_{Sch} = \Delta f_{Lichte} \tag{2.16}$$

So that the optimized C_S and defocus values can be derived. Under WPOA, both conditions (positive C_S with negative Δf and negative C_S with positive Δf) should have the same effect. However, when negative C_S is used with positive Δf, then the electron-channeling-induced amplitude contrast, which gives a bright spot at the location of the atomic column, will enhance the phase contrast, which will give brights spot at the locations of the atomic columns.[141, 142] Thus, the negative C_S imaging (NCSI) is preferred. For an aberration-corrected microscope with information limit $u_{max} = (0.08\text{nm})^{-1}$, the optimized C_S is -13 μm, and the optimized defocus is +6nm. Light elements in transition metal oxides, such as oxygen atomic columns, which were not visible in conventional TEM, give detectable contrast under these imaging conditions provided that the specimen is thin enough to comply with the WPOA.[143]

2.1.2 Scanning Transmission Electron Microscopy Imaging

Bright Field (BF)

The NCSI condition requires small negative C_S, whereas the C_S is usually set to be as small as possible in aberration-corrected STEM imaging in order to form the smallest probe. A slightly negative C_S can be used to balance the positive fifth-order spherical aberration.[144] Coherent imaging using phase contrast is achieved using a bright-field (BF) detector. The difference with the TEM counterpart is the Fourier transform of the phase change due to aberrations, which is the probe amplitude distribution $P(R)$, which is referred as the point spread function in the TEM case.[145]

$$\mathcal{FT}\{\exp[-i\chi(\mathbf{u})]\} = P(R) = \int e^{2\pi i \mathbf{u}\cdot R} e^{-i\chi(\mathbf{u})} d\mathbf{u} \tag{2.17}$$

The bright field image intensity is given by

$$I_{BF}(\mathbf{R}) = |f(\mathbf{R}) \otimes P(\mathbf{R})|^2 \tag{2.18}$$

where $f(\mathbf{R})$ is given in equation 2.2. The image contrast can be improved by using the annular-bright-field (ABF) imaging mode (implemented using a BF detector in conjunction with a beam stop).[146] ABF imaging is similar to hollow cone illumination in STEM[147], in which the tilted incident beam can reduce the effect of the chromatic aberration C_C.[148] It has been demonstrated that atomic columns as light as hydrogen can be directly imaged using this imaging mode.[149]

When a small BF detector on the optic axis is used, STEM is equivalent to CTEM imging based on the reciprocity principle.[150, 151] However, if a large coherent convergent beam is used and the collection angle is set equal to the convergence angle, the phase contrast will be suppressed.[152] The contrast has very weak defocus and thickness dependence.[153, 154] The incoherent high-angle bright-field (HABF) image

contrast is a simple convolution between the object function $O(\mathbf{R_0})$ and the effective probe intensity $P_{eff}(\mathbf{R_0})$

$$I_{HABF}(\mathbf{R_0}) = O(\mathbf{R_0}) \otimes P_{eff}(\mathbf{R_0}) \tag{2.19}$$

high-angle annular-bright-field (HAABF) imaging is used in this dissertation research for determining the position of oxygen atomic columns in the lattice.

Dark Field (DF)

When the inner collection angle is increased to avoid the bright field region, both coherently and incoherently scattered electrons are collected. The coherent part can give diffraction contrast and has been used in tomography reconstruction.[155] For the incoherently scattered part, any effect that leads to dechannelling of the incident electron beam will give rise to contrast.[156]

Low-Angle Annular-Dark-Field (LAADF)

The random strain fields from point defects can give rise to incoherently scattered contrast which is more pronounced at low scattering angles.[157, 158] The low-angle annular-dark-field (LAADF) imaging mode has been used for detecting oxygen vacancies in $SrTiO_3$ with unit-cell resolution, with the collection semi-angle at 25-50 mrad and acceleration voltage at 200 kV.[156] Atomic-resolution defect contrast in LAADF is also observed in γ/γ' Ni-superalloys[159] and CeO_2 nanoparticles (known as oxidation-state-sensitive imaging)[160]. However, when the collection angle is small enough, coherently scattered diffraction contrast such as thickness fringes may occur, and multi-slice image simulations are required to interpret the intensity.[161]

High-Angle Annular-Dark-Field (HAADF)

In high-angle annular-dark-field (HAADF) imaging, diffraction contrast is fully

suppressed and thermal diffuse scattering (TDS) is dominant. This requires [162]

$$\theta_{\mathrm{HAADF}} \geq \lambda / d_{\mathrm{thermal}} \tag{2.20}$$

where λ is the electron wavelength and $\mathrm{d_{thermal}}$ is the amplitude of atomic thermal vibration. For silicon at room temperature, and an acceleration voltage of 200 kV, $\theta_{\mathrm{HAADF}} > 40$ mrad.[145]. In TDS at high scattering angle, the atomic form factor has the following form [163, 164]

$$f'_{\mathrm{HA}}(M, s) \approx \sigma_{\mathrm{TDS}} \propto \int_{\mathrm{detector}} f^2(s) \left[1 - \exp(-2M \cdot s^2)\right] d^2\mathbf{s} \tag{2.21}$$

where M is Debye-Waller factor proportional to the mean square of the thermal verbration amplitude $< u^2 >$. Since $f(s)$ is related to atomic number Z, the HAADF contrast is often referred as Z-contrast. At very high angle, the scattering cross-section approaches Z^2 dependence, which is similar to Rutherford scattering from an unscreened nucleus. Lower-angle scattering cross sections range from Z^2 to $Z^{3/2}$.[165, 166] For collection angles of (50-250 mrad) with acceleration voltage of 200 kV, HAADF signal scales approximately as $Z^{1.7}$.[156] For mass-thickness contrast, HAADF is more effective than bright-field imaging.[164] Similar to other imaging modes, the HAADF signal is also affected by channelling when a low-index zone axis of a crystal sample is aligned with the electron beam direction. The channelling effect reduces the spreading of the beam as it propagates through the sample, which is useful for imaging atomic columns in thick samples in probe-corrected microscopes.[167] Channelling also enhances the high-angle scattering, thus increasing the HAADF signal.[166, 168] In comparison, phase contrast modes such as NCSI can also benefit from channelling for thin samples. However, for thicker samples where the WPOA does not hold, contrast reversal occurs due to phase wrapping.

2.1.3 Image Quantification

2.1.3.1 Comparison of Experimental and Simulated Images

Image quantification can provide structural or even chemical information about the sample, as introduced in previous sections. The projected atomic columns in a crystalline sample often appear as bright or dark spots in atomic-resolution images. The positions of the spots are related but often not directly to atomic positions in the sample. Assuming the brightest (or darkest in BF mode) position in a high-resolution image as corresponding to the atomic position is often biased for two reasons. First, when the sample is not extremely thin, Equations 2.2 to 2.5 are no longer valid anymore. the wave propagation inside a sample cannot be expressed as the projected atomic potential and absorption function convoluted with the atomic positions. The exit wave at any atomic column will be affected by neighboring atomic columns in a complicated way. An example is the channelling effect. [169–171] Second, when atomic columns are not well separated, the tail of one intensity peak may affect the positions of neighboring peaks, unless the local symmetry around that atomic column ensures the effect of all nearby atomic column have canceled each other. However, most important cases of atomic position measurement are dealing with local symmetry breaking such as ferroelectric displacements or surface/interface displacements.

A feasible method to recover atomic structure information from TEM or STEM images is as follows. Different structure models are constructed and the corresponding images are simulated. The simulated images are compared with experimental data and the parameters of the structure model and the imaging conditions in the simulation are then adjusted through an iterative procedure until a close match is reached.[172]

Recent experimental examples of this method include using an aberration-corrected STEM to determine the depth position of a individual dopant atom in crystalline $SrTiO_3$,[173], and using the aberration-corrected TEM to determine the 3D surface structure of a MgO crystal from a single micrograph.[174]

For phase contrast images, cross-correlation coefficients between an experimental image and simulated images are often used as the matching criterion.[175] However, in many high-resolution images, especially STEM-HAADF images, the intensity of an atomic column is a 2D Gaussian function (due to central limit theorem).

$$I(x,y) = f(x,y) \tag{2.22}$$

$$= \frac{A \cdot \exp\left(-\frac{1}{2(1-\rho^2)}\left[\frac{(x-\mu_X)^2}{\sigma_X^2} + \frac{(y-\mu_Y)^2}{\sigma_Y^2} - \frac{2\rho(x-\mu_X)(y-\mu_Y)}{\sigma_X\sigma_Y}\right]\right)}{2\pi\sigma_X\sigma_Y\sqrt{1-\rho^2}} \tag{2.23}$$

Such a 2D Gaussian function will only have a few adjustable parameters A, σ_X, σ_Y, ρ, μ_X and μ_Y. When comparing experimental and simulated images, comparison of the parameters derived from the images as the criterion would be sufficient if the intensity of the atomic columns does not deviate from a 2D Gaussian function. Comparing these parameters instead of comparing pixel-by-pixel can also avoid over-fitting, and make the calculation simpler.

2.1.3.2 Limitations from Electron Dose and Resolution

The ultimate limit of accuracy in estimating the position of an individual atomic column is set by the electron dose. The intensity (electron count) of each pixel around the atomic column is measured. An estimator of the central position uses this intensity data.

$$(\hat{\mu_X}, \hat{\mu_Y}) = \hat{\mu}(I(x_1,y_1), I(x_2,y_2), ..., I(x_n,y_n)) \tag{2.24}$$

where $I(x_i, y_i)$ are the intensity of n pixels $(x_1, y_1), (x_2, y_2), ..., (x_n, y_n)$ around the atomic column and the total electron count

$$N = \sum_{i=1}^{n} I(x_i, y_i) \tag{2.25}$$

A good estimator should be both unbiased and having minimum mean-squared error.[176] Consider an ideal case in which the position (X_i, Y_i) of each individual electron that forms a high-resolution image can be measured individually and accurately on the image. When the shape of the atomic column is a Gaussian function (e.g., in HAADF), the sample set $\{(X_i, Y_i), i = 1, 2, ..., N\}$ is from a 2D Gaussian distribution with mean (i.e. the center of the atomic column) (μ_X, μ_Y), standard deviation (i.e. the size of the atomic column) (σ_X, σ_Y) and $\rho = 0$. The uniformly minimum-variance unbiased estimator (UMVUE) [177] for (μ_X, μ_Y) is the mean position of all the electrons.

$$(\hat{\mu_X}, \hat{\mu_Y})_{UMVUE} = \frac{1}{N} \sum_{i=1}^{N} (X_i, Y_i) \tag{2.26}$$

The mean squared error of this unbiased estimator is

$$MSE = var((\hat{\mu_X}, \hat{\mu_Y})_{UMVUE}) = \frac{1}{N}(\sigma_X^2, \sigma_Y^2) \tag{2.27}$$

where the population standard deviation σ_X and σ_Y can be estimated from the sample standard deviation S_X and S_Y. Therefore, the standard error of the estimator in equation 2.26 is $1/\sqrt{N}$ of the standard variation (σ_X and σ_Y) of the Gaussian intensity profile in equation 2.23. Two factors determines σ_X and σ_Y. First, the atomic column in the exit wavefunction already have finite size. Second, the instabilities and aberrations in the microscope further increase the apparent size of the atomic column in the recorded image.

As an example, when using an aberration-corrected STEM to record a HAADF image, if there is an atomic column with 95% percent of the HAADF intensity within a

radius of 50 pm and there are 10^4 electrons in the atomic column, then the center of the Gaussian intensity peak can be estimated with no better than $50pm/\sqrt{10^4} = 0.5pm$ accuracy at the 95% confidence level.

In microscopes where a CCD or a direct electron detector is used, the expected accuracy will be lower, because the intensity data is pixelated. The estimator in equation 2.26 using the mean position of all electrons turns into a calculation of the moment of the intensity.

$$(\hat{\mu_X}, \hat{\mu_Y}) = \frac{1}{N}\sum_{i=1}^{N}(X_i, Y_i) \tag{2.28}$$

$$= \frac{(\sum_{i=1}^{n} x_i \cdot I(x_i, y_i), \sum_{i=1}^{n} y_i \cdot I(x_i, y_i))}{\sum_{i=1}^{n} I(x_i, y_i)} \tag{2.29}$$

In equation 2.29, the estimated position is a weighted mean of each pixel. and the weight is proportional to its intensity. This can be understood by the fact that each pixel effectively has a variance of $(\sigma_X^2, \sigma_Y^2)/I(X_i, Y_i)$. By multiplying the weight $I(X_i, Y_i)$, each pixel (not each electron) becomes independent and identically distributed (IID). The least square estimator, which is the weighted mean, is then used (the Gauss–Markov theorem [176]). This transformation will be used again later when the effect of noise is considered.

The intensity moment is the best estimator (UMVUE) and should be preferentially used when the pixel size is negligible compared to the radius of the atomic column and there is no background or additional noise except for the Poisson shot noise.

2.1.3.3 Limitations from Background Noise

When additional noise, which usually comes from positive background due to inelastic scattering, or from thermal noise of the CCD camera or electron detector,

is added, then equation 2.26 and 2.29 are no longer UMVUE. If the additional noise comes from a uniform positive background with average electron count of λ, the background count follows a Poisson distribution and can be approximated by a Gaussian distribution with mean value of λ and standard deviation of $\sigma_{cnt} = \sqrt{\lambda}$ when $\lambda > 10$. The mean intensity of the background λ can be deducted from the intensity before further data processing. If the additional noise is the dark thermal noise, the background can also be approximated by a Gaussian with mean value of 0 and standard deviation of σ_{cnt}^2 which depends on the property of the CCD camera or the detector. Here a weighted average method is suggested and the derivation is as follows.

Let σ_{cnt} represent the overall variance of electron count (not the position) caused by background in each pixel. In order to use the Gauss–Markov theorem, which requires all pixels to have the same finite variance, each pixel needs to be reweighted. Let c represent the actual electron count on each pixel . c' represents the recorded electron count. (i.e. $I(X_i, Y_i) = c'$). The expected value of the "effective" variance of the position (not the count) contained in each pixel is calculated as follows.

$$E\left[var(\frac{\sum_i X_i}{c})\right] = \int_{-\infty}^{\infty} \frac{\sigma_X^2}{c} \frac{1}{\sqrt{2\pi}\sigma_{cnt}} \exp\left[-\frac{(c-c')^2}{2\sigma_{cnt}^2}\right] dc \tag{2.30}$$

This integral cannot be solved. However, assuming $\sigma_{cnt} \ll c$ (excluding very noisy pixels) and using Taylor expansion for $\frac{1}{c}$ around c', let $\Delta = c - c'$

$$\frac{1}{c} = \frac{1}{c' + \Delta} \tag{2.31}$$

$$= \frac{1}{c'} - \frac{\Delta}{c'^2} + \frac{\Delta^2}{c'^3} + O(\Delta^4) \tag{2.32}$$

The integral in equation 2.30 is then solved as

$$E\left[var(\frac{\sum_i X_i}{c})\right] = \frac{\sigma_X^2(\sigma_{cnt}^2 + c'^2)}{c'^3} \tag{2.33}$$

where the $\sum_i$ is summing over a pixel. The same derivation can be done for Y direction. In order to use the Gauss–Markov theorem, weight is inversely proportional to the variance in equation 2.33. Thus, each pixel should be weighted by $\frac{(I(X_i,Y_i))^3}{\sigma_{cnt}^2+(I(X_i,Y_i))^2}$

$$(\hat{\mu_X}, \hat{\mu_Y}) = \frac{1}{N}\sum_{i=1}^{N}(X_i, Y_i) \tag{2.34}$$

$$= \frac{\left(\sum_{i=1}^{n} x_i \cdot \frac{(I(X_i,Y_i))^3}{\sigma_{cnt}^2+(I(X_i,Y_i))^2}, \sum_{i=1}^{n} y_i \cdot \frac{(I(X_i,Y_i))^3}{\sigma_{cnt}^2+(I(X_i,Y_i))^2}\right)}{\sum_{i=1}^{n} \frac{(I(X_i,Y_i))^3}{\sigma_{cnt}^2+(I(X_i,Y_i))^2}} \tag{2.35}$$

In another extreme, when background noise is dominant, $\sigma_{cnt} \ll c$ is not valid almost everywhere, and the weighted moment in equation 2.35 cannot be calculated. The direct 2D Gaussian fit[178] is another algorithm to find the center of an individual spot. The intensity around a bright spot is fitted to a 2D Gaussian function in equation 2.23. An iterative method is used and the parameters in the 2D Gaussian function are updated until the least-square error reaches a minimum. In this case, direct 2D Gaussian fit is the best estimator because the variance is mostly background noise, and it is the same for every pixel.

2.1.3.4 Limitations from Pixelation

In atomic-resolution electron microscopy, it has been demonstrated that the positions of a single atomic column can be determined with sub-pixel accuracy.[179] With such accuracy, the effect of pixelation becomes an issue because the positions of pixels are discrete and the electron count is integrated over the area of the pixel. When the size of a spot is not significantly larger compared to the size of a pixel, the effect of pixelation is more obvious. It would very complicated to investigate this problem using analytical methods. Numerical methods can instead be used.

The scenario of relatively low SNR and very small object size (large pixel size) has been investigated using numerical simulations by people working on single-particle tracking in biophysics and star-image positioning in astronomical studies, where the radius of an object to be measured is only 1-2 pixels. Although the radius of an atomic column is often 5-20 pixels in high-resolution electron microscopy, simulation results tested for small objects may still be useful.

First, giving higher weight to brighter pixels in any algorithms generally increases the accuracy.[180, 181] This is consistent with the analytical analysis in previous sections.

Second, proper sub-pixel interpolation will reduce the bias and increase the accuracy.[182, 183] The analytical form of the interpolation function, even without considering the noise, is very complex.[182]

Third, the 2D Gaussian–fitting method outperforms the simple moment method over a wide parameter range, especially at low SNR.[180, 183] The moment method tends to bias towards the geometric center of the area being included in the calculation when the area is defined by the pixels above a certain threshold.[183] The bias and standard deviation of position using the moment method also fluctuates with the actual position of the center inside the pixel.[183] However, these results are for small objects with radius of 1-2 pixels. Both the bias and standard deviation are less than 1 pixel in both methods. Results for atomic columns have not yet been evaluated.

2.1.3.5 Strategies and Algorithms Used

From the discussions above in chapter 2.1.3.1 to 2.1.3.4, in order to do quantification for high-resolution images, the strategy should be as follows:

1. Calibrate the analogy amplifier for the detector or CCD so that the electron count being read reflects the actual electron count.

2. The dark noise and the background should be measured for the same conditions as for the image acquisition. These data are needed for calculating the parameters of the noise distribution.

3. Unless the material is beam-sensitive, use large electron dose and dose rate for the exposure in order to obtain high SNR. Large dose rate is preferred because part of the dark noise is proportional to the exposure time. If the material is beam-sensitive, a balance between the increment of dark noise and beam damage will be needed. For the same reason, although sampling higher than the Nyquist frequency (using pixel size smaller than the information limit) does not carry any useful information except noise, it increases the sub-pixel accuracy.

The intensity data is then processed off-line for determining the atomic column positions in the image.

A small program has been developed and it works as follows:

1. Three parameters are defined for rough peak finding:

MAX_THRESHOLD. Any pixels brighter than this threshold are recognized as spike noise and are excluded.

MIN_THRESHOLD. Pixels darker than this are recognized as random fluctuations in the background instead of a peak.

PEAK_RADIUS. No second pixel within this distance to an existing peak will be recognized as another peak.

2. Sort the list LIST_OF_PIXELS with all pixels between maximum and minimum threshold in the image by brightness.

3. Label the brightest pixel in the list as a peak, move it to another list named

LIST_OF_PEAKS, remove every pixel within a distance of PEAK_RADIUS from LIST_OF_PIXELS. Then label the brightest pixel in the reduced list again. Step 3 will be looped until the LIST_OF_PIXELS is empty. This procedure finds all pixels with the intensity local maximum as a rough position.

4. Define a FITTING_RADIUS, For each pixel in LIST_OF_PEAKS, use the position of that pixel as starting, use moment method or 2D Gaussian fit to refine the position ATOMIC_CENTER with sub-pixel resolution. The refined position is put into LIST_OF_CENTERS. The moment method is currently implemented. The weight and background level can be given. If not given, the simple moment method will be used and the background level will be set to the minimum intensity within FITTING_RADIUS. the refinement will be iterated until convergence (i.e. ATOMIC_CENTER does not change anymore.). The total electron count ATOMIC_BRIGHTNESS can also be calculated at the same time. The atomic column position data and the intensity data in the experimental image can then be compared with the same data obtained from the simulated image.

2.2 Electron Holography

Transmission electron microscopy usually only provides intensity information for the electron wave, whereas both the amplitude and phase information are available in electron holography. Experimental methods include in-line holography, off-axis holography, etc.[184] In this dissertation research, off-axis TEM holography has been used. A very thin conducting wire is inserted into the microscope perpendicular to the electron beam close to the image plane of the objective lens. This wire is connected to a positive voltage to serve as a biprism and deflect the electron waves on each

side so that interference fringes form at a distance. The specimen is put on one side, and the amplitude and phase of the sinusoidal interference fringes represent the amplitude and phase of the exit wavefunction.[184] Electron holography is a useful tool for material analysis. It has been demonstrated that magnetic fields, electrostatic potential, polarization fields and 2DEG charge density in semiconductors can be mapped using off-axis electron holography.[185–188]

2.2.1 Mean Inner Potential

The transfer function of the objective lens have already been discussed in Chapter 2.1.1. In holography, both amplitude and phase information are collected. The cross-talk between amplitude and phase is illustrated in Figure 2.1 Unlike NCSI, the C_S should be adjusted to a value as small as possible to minimize delocalization when recording a hologram in an aberration-corrected microscope.

The interaction of the high energy incident electron with electromagnetic fields inside the sample is described by the time-independent Schrödinger equation [184]

$$\left(\frac{1}{2m}\cdot(-ih\nabla+e\mathbf{A})^2-eV\right)\psi=E\psi \tag{2.36}$$

where ψ, $\mathbf{A}$ and V are the wavefunction, the vector potential and the scalar potential. In equation 2.36, one electron approximation is used. Only elastic scattering is considered because the inelastic terms are at least an order of magnitude smaller.[184] Different from holography using low energy electron diffraction (LEED), exchange-correlation potential V_{xc} in solid state physics does not need to be considered because of the high energy difference between the incident and atomic electrons.[189]

Instead of solving Bloch states, apply the Wentzel–Kramers–Brillouin (WKB) approximation to solve equation 2.36, and assume the object electron wavefunction

has the form of $\psi(x,y) = a(x,y)e^{i\psi(x,y)}$[184]

$$\psi(x,y) = \frac{\pi}{\lambda E}\int_L V(x,y,z)dz - \frac{2\pi e}{h}\int_L A_Z(x,y,z)dz \tag{2.37}$$

Assume that the magnetic field to be zero and $V(x,y,z)$ is constant within the space. Integrating over the sample with thickness t.

$$\psi = \frac{2\pi}{\lambda U_A}\cdot\frac{2m_0c + eU_A}{m_0c^2 + eU_A} = CV_0t \tag{2.38}$$

U_A is the accelerating voltage. $C = 1.039\times10^6 m^{-1}eV^{-1}$ for 300 kV electrons. V_0 is the mean inner potential.[184] In the normal experiments, the sample is tilted off-zone in order to avoid dynamical diffraction.

V_0 is the electrostatic (Coulomb) potential $V(\mathbf{r})$ averaged within the material of volume Ω.

$$V_0 = \frac{1}{\Omega}\cdot\int_\Omega V(\mathbf{r})d\mathbf{r} \tag{2.39}$$

The use of DFT calculations to estimate the mean inner potential (MIP) (V_0) will be introduced in Chapter 2.6.3. Another way to estimate V_0 from experiment other than holography is assuming atoms in the specimen consist of neutral free atoms, and using the sum of the 0th atomic scattering amplitudes as the V_0

$$V_0 = \frac{h^2}{2\pi m_0 e\Omega}\cdot\sum_j f_j(0) \tag{2.40}$$

where the sum is performed over the j atoms in the unit cell. V_0 is often overestimated because equation 2.40 ignores the valence electrons.[184]

The MIP is affected by valence charge. Give an example, MgO is an oxide with simple FCC structure. For a pro-crystal made of charge neutral Mg and O atoms, the calculated MIP is 18.43V. If Mg^{2+} and O^{2-} are considered, the calculated MIP is 12.85V, which is close to the experimental value of 13.01V.[190]

In analogy to the work function being affected by the surface, the MIP is also affected by surface and adsorbates. DFT calculations show that the MIP depends on the surface orientation, surface reconstruction, surface atom relaxation and adsorbed atoms.[191, 192] As an example, the MIP of Si ranges between 12.01V to 14.12V with different surface orientation, type of surface reconstruction, surface composition and surface relaxation.[191] All of these factors give discrepancies between theoretical and directly measured MIP values. Consider that Si is a non-polar material and atoms in Si have neutral charge, while oxides often consist of charged ions and are polarized. The MIP of oxides may also be affected more by their surface states.

2.3 Electron Energy-Loss Spectroscopy

2.3.1 Electron Energy-Loss Near-Edge Structure

STEM-EELS is used for acquiring the Electron Energy-Loss Near-Edge Structure (ELNES) because this approach gives both high spatial resolution and energy resolution, which is necessary for investigating complex oxide interfaces.

The transition probability can be expressed in the double differential scattering cross section (DDSC) form by [193]

$$\frac{\partial^2\sigma}{\partial E\partial\Omega} = \frac{4\gamma\gamma'}{a_0^2 q^4}\frac{k'}{k}S(\mathbf{q}, E) \tag{2.41}$$

where σ is the cross-section. E is the energy-loss. Ω is the solid angle. $\gamma^2 = 1/(1 - v^2/c^2)$. $\gamma'^2 = 1/(1 - v'^2/c^2)$. v and v' are velocity of incident and scattered fast electrons. $a_0 = \frac{4\pi\epsilon_0\hbar^2}{me^2}$ is the Bohr radius. k and k' are the wave vectors of the incident and scattered fast electrons and $\frac{k'}{k} \approx 1$. The dynamic form factor (DFF) $S(\mathbf{q}, E)$ is

given by[193]

$$S(\mathbf{q}, E) = \sum_{junoc} \left| \left\langle \phi_i | e^{i\mathbf{q}\cdot\mathbf{r}} | \phi_j \right\rangle \right|^2 \delta(E_i + E - E_j) \tag{2.42}$$

i and j are initial and final states. $\mathbf{q}$ is the momentum transfer.

Because the core-level states are highly localized, the sum in DFF is mainly determined by the unoccupied density of state.[194] Thus, ELNES can be regarded as a probe of the local density of state with spatial, energy and momentum resolution. Several factors limit the spatial and energy resolution. In addition to limitations due to the microscope such as acceleration voltage and lens instability, the spatial and energy resolution are further limited by the electron-specimen interaction.

The spatial delocalization due to the long-range nature of the electrostatic interaction between the incident electron and atomic electrons increases with incident electron wavelength λ and decreases with scattering angle θ.[195] Thus, higher incident energy and larger energy loss give smaller delocalization. For the ELNES signals used in this research, incident beam energy of 100-200 keV and energy losses of 100-2000 eV have been used. The delocalization width is then in the range of 0.1-0.4 nm[195] for thin samples. Unit-cell resolution should therefore be possible.[156]

The spectral broadening (energy resolution) is limited by the core-hole lifetime and the final-state lifetime, as defined by Heisenberg's uncertainty relation $\Gamma\tau \approx \hbar$. Both the core-level broadening and the final-state energy broadening increase with energy threshold.[195]. This effect will be considered in simulations described in chapter 2.6.2. Energy losses higher than 500 eV will give broadening greater than approximately 0.2 eV. Therefore, a cold-field-emission electron gun might be helpful but an ultra-fine monochromator is not necessary.

Plural scattering in thick samples creates a broad double-scattering peak at $E_k + E_p$, where E_k is the main edge and E_p is the energy of plasmon peak.[195] This can be

removed from the spectrum by deconvolution using low-loss spectrum. To avoid the complexity of acquiring low-loss spectrum and losing SNR, all experimental spectra in this dissertation were collected at thicknesses $t/\lambda < 0.8$ where λ is the inelastic-scattering mean free path. This was verified by the zero-loss and low-loss spectra in the same area.

When doing ELNES quantification, the complexity of the electron wave propagation inside the sample has to be considered. Channelling happens before and after the inelastic scattering process. The double-channelling results can be as much as 20% different from single channelling predictions even for a thin sample.[196] Despite this restriction, an linear model which assumes that the ELNES signal is linearly proportional to the area density is still used for semi-quantification in this dissertation research.

2.3.1.1 Ti-L edge

The $\mathrm{Ti-L_3}$ edge (originating from $2p_{3/2}$ to $3d$ transitions) and $\mathrm{Ti-L_2}$ edge (originating from $2p_{1/2}$ to $3d$ transitions) are separated by about 5.5 eV. In Ti^{4+}, each of them is further separated into t_{2g} and e_g peaks due to crystal-field splitting of Ti-3d. As the oxidation state decreases, in mixed Ti^{3+} and Ti^{4+} states such as the Magneli phases Ti_4O_7 and Ti_5O_9, a pre-peak a' and b' (see Figure 2.2) appears due to orthorhombic polyhedra distortions.[197] The t_{2g} and e_g merge together in Ti^{3+}. In Ti^{2+} and metallic Ti, the peaks systematically shift to lower energy, as shown in Figure 2.2. The shapes of the Ti white lines are dominated by the multiplet effect[198, 199] and are sensitive to the Ti oxidation state.[156]

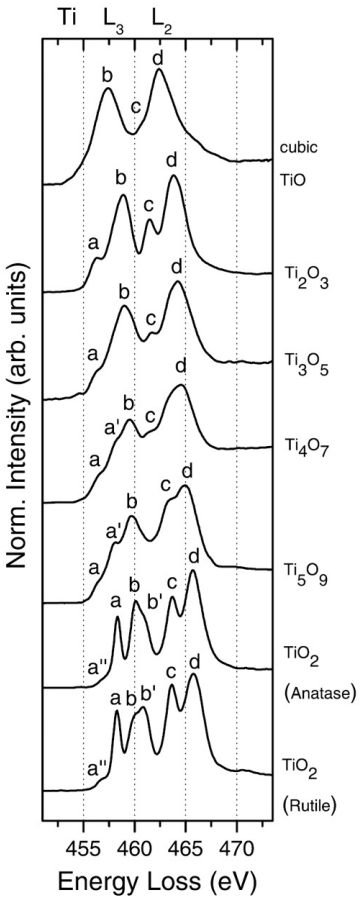

Figure 2.2. $\mathrm{Ti} - \mathrm{L}_{3,2}$ ELNES spectra of several Ti oxides.

Notice the crystal field splitting and merging of peaks for lower oxidation states. Figure taken from Ref.[197].

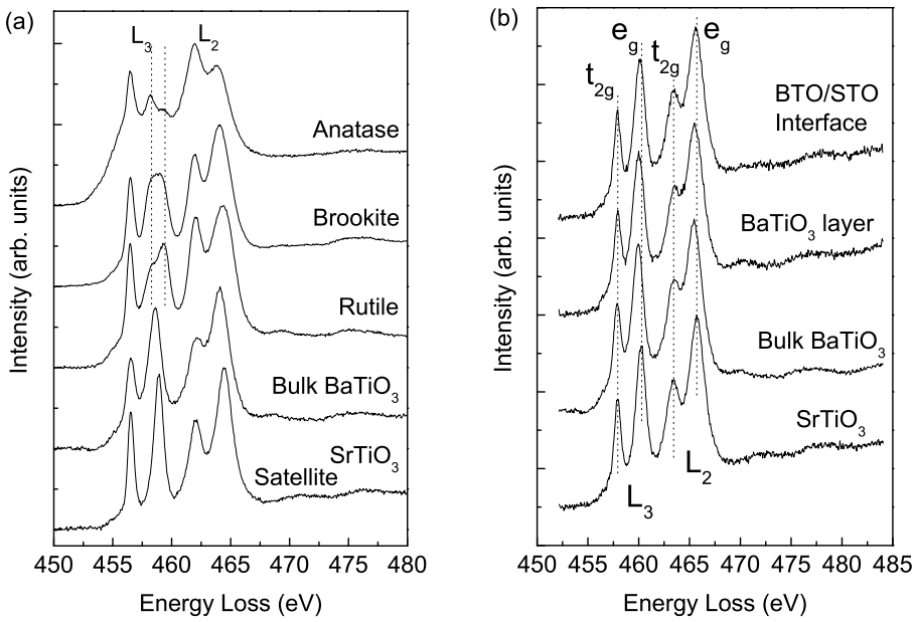

Figure 2.3. $Ti - L_{3,2}$ ELNES spectra of BTO, STO and several Ti oxides.

(a) Experimental spectra of bulk BTO and STO compared to TiO_2 anatase, brookite, and rutile. Notice the crystal field splitting, especially the e_g splitting indicated by the dashed line. Satellite structures appear above the white lines. (b) Comparison of $Ti - L_{3,2}$ edges measured in STO, BTO, and at the BTO/STO interface. Figures taken from Ref[200]

The satellite peaks above the white lines originate from the backscattering at neighboring atoms and the shifts of these satellite peaks are sensitive to inter-atomic distance.[200]

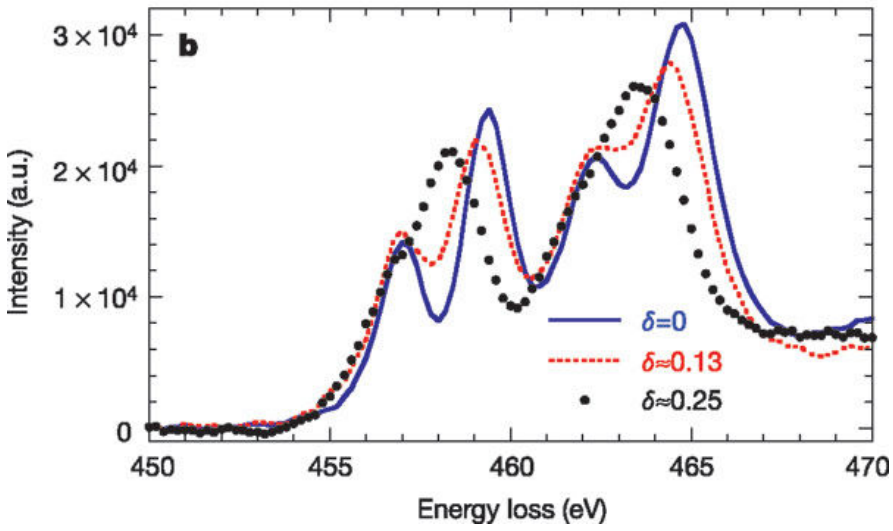

Figure 2.4. $\mathrm{Ti-L_{3,2}}$ ELNES spectra in $SrTiO_{3-\delta}$ with oxygen vacancies. Figure taken from Ref[156]

2.3.1.2 O-K edge

The oxygen K edge originates from the transition from inner K shell to the empty hybridized O-$2p$ orbits with Ti-$3d, 4s, 4p$ orbits.[201] Peaks before 537 eV originate from the transition to t_{2g} and e_g states.[201] The peak between 537 eV to 546 eV originates from transitions into Ti-$4s, 4p$ orbits.[202] An alternative explanation for the peaks above 537 eV is backscattering at neighboring atoms.[203]

The O-K ELNES is sensitive to local environment and it is a good approximation to the projected density of state at the oxygen atom[204] Figure 2.5 to 2.7 show the O-K edge in different materials.

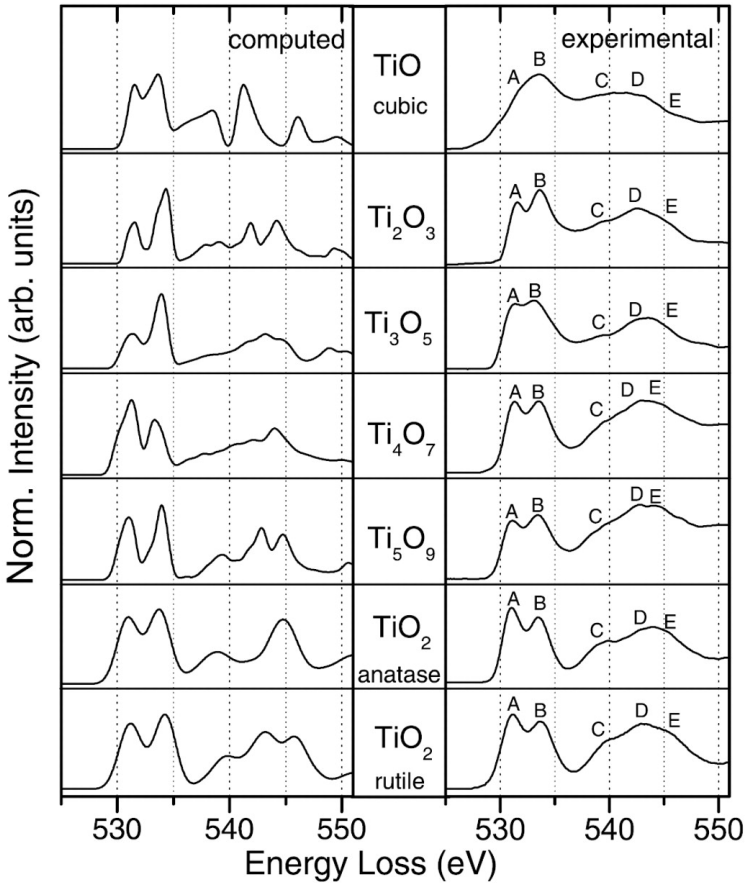

Figure 2.5. $O-K$ ELNES spectra of several Ti oxides.

Notice the crystal field splitting (peak A and B) and merging of peaks at lower oxidation states. Figure taken from Ref.[197].

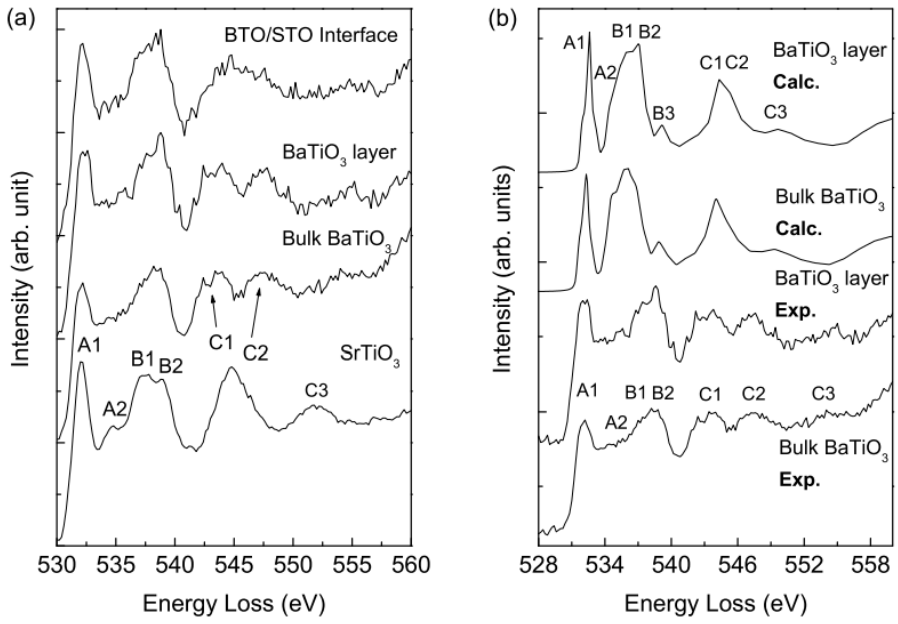

Figure 2.6. O − K ELNES spectra of BTO, STO and several Ti oxides.

(a) Comparison of the O − K edge in $BaTiO_3$, $SrTiO_3$ and their interface. (b) Experimental and simulated oxygen K edges of bulk $BaTiO_3$ and $BaTiO_3$ thin film. Figures taken from Ref[200]

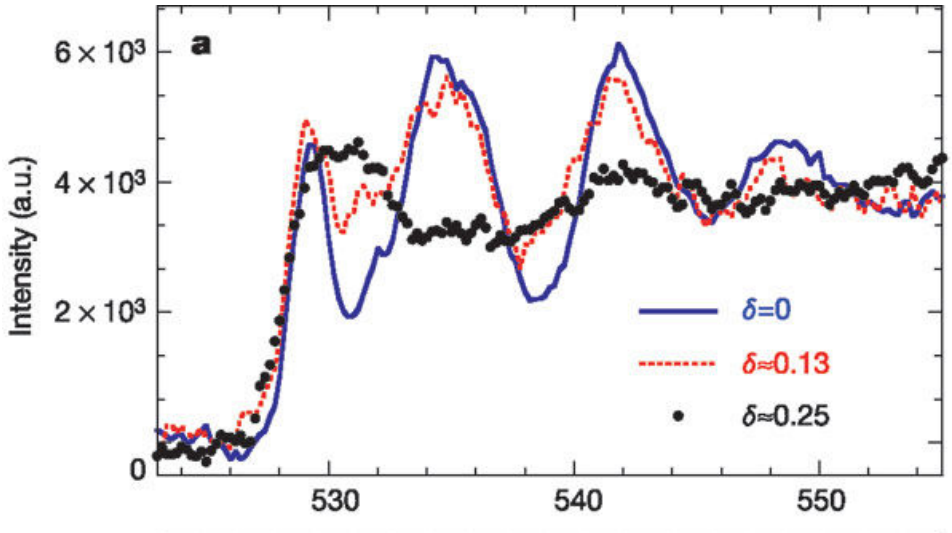

Figure 2.7. O − K ELNES spectra in $SrTiO_{3-\delta}$ with oxygen vacancies.

Figure taken from Ref[156]

2.4 Hyperspectral Unmixing

ELNES is sensitive to small atomic or electronic structural changes. High accuracy chemical analysis, especially at interfaces or at dislocation core, or for detection of orbital or magnetic signals, requires more accurate quantitative spectral analysis. Limited by the electron dose, the SNR cannot increase proportionally. On the other hand, with improving spectral and energy resolution, the amount of data acquired in one spectrum image is large. In modern microscopes, an 512 pixel x 512 pixel x 2048 channel spectrum image with 16 bits of quantization will produce 1 gigabyte per spectrum image. New methods for quantitative spectrum image analysis are necessary to handle such large data sets.

The hyperspectral unmixing technique is a powerful tool for spectrum analysis, and has been succesfully applied to geometrical data in remote sensing[205]. The hyperspectal image in EELS and the geometrical data have many similarities. They both have many pixels (to form an image) and multiple channels (to form a spectrum). An important similarity is that the spectrum in each pixel in many cases is not just a spectrum from a pure material, but a mixture from several different materials. For example, due to resolution limits, each pixel in geometrical data can be a mixture of roadways and vegetation, which have two different spectra. In material analysis, the oxidation state may change gradually over an area and in each pixel spectrum appears as a mixture of the two spectra for high and low oxidation states. An important difference is that the geometrical data acquired by modern remote sensing devices can give high SNR (> 500 or ~ 27dB[206] in AVIRIS data [207] for example), whereas the electron count per channel in EELS mapping is usually less than 10^4, or even as few as several dozen, giving a typical SNR of 10-20dB, even without considering the

EELS background. In this section, a standard procedure with several improvements, including pre-processing, is introduced so that ELNES data will fit the hyperspectral unmixing algorithms, The approach can then be applied to ELNES data having low SNR.

2.4.1 Basis

In a linear mixing model, the data in a spectrum image is represented by a matrix $\mathbf{r}$ of size $L \times N$, where each column represents a pixel in the image with a total of N pixels, and each row represents a channel in the spectrum with a total of L channels (dimensions). In the linear mixing model, the spectrum image is a product of the endmember matrix $\mathbf{M}$ and an abundance matrix α,[205]

$$\mathbf{r} = \mathbf{M}\gamma\alpha + \mathbf{n} \tag{2.43}$$

M is a matrix of size $L \times p$, p is the number of independent endmembers, γ is a scale factor, and n is the random noise. The abundance matrix has the following constraints.[205]

$$\text{Non-negativity} \qquad \alpha_{i,j} \geq 0 \tag{2.44}$$

$$\text{Sum-to-one} \qquad \mathbf{1}^T\alpha = 1 \tag{2.45}$$

Linear unmixing algorithms take dataset $\mathbf{r}$ as input and calculate the endmember matrix $\mathbf{M}$ and abundance matrix α. There are several different approaches. Take a simplex-based algorithm as an example. The convex hull of the columns of $\mathbf{M}$ forms a $p-1$ simplex in $\mathbb{R}^L$, as illustrated in Figure 2.8. The N-FINDR algorithm maximizes the simplex volume with endmembers within the dataset.[209]

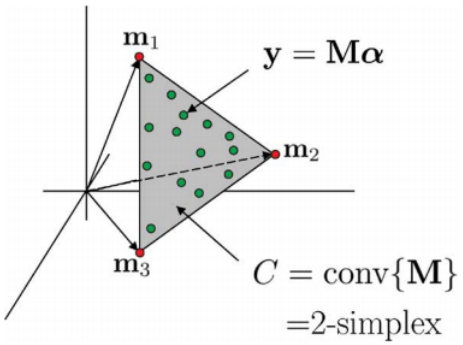

Figure 2.8. Illustration of the simplex set C for $p = 3$.

C is the convex hull of the columns of $\mathbf{M}$. Green circles represents N spectral vectors in dimension L. Red circles represent the p endmembers. Figure taken from Ref[208].

In this work, a set of improved algorithms optimized for ELNES map unmixing has been developed. Figure 2.9 is an outline of the unmixing procedure. The details are discussed in the following sections.

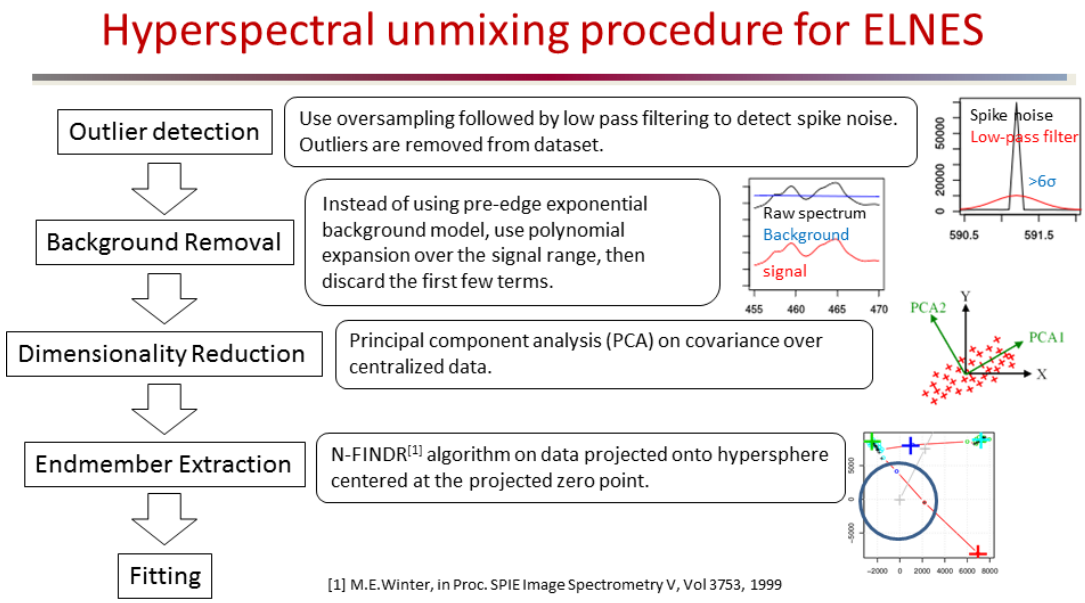

Figure 2.9. Standard procedure developed for ELNES map unmxing.

2.4.2 Outlier Detection

The spike-noise peaks are outliers in the dataset. For second-order statistics–based algorithms such as PCA, a single data point with spike noise will give large variance. For the simplex-based algorithms, data points with spike noise are usually far away from the original simplex. Therefore, these algorithms will always fail when spike noise is still present in the data. However, spike noise is very common in any CCD or electron detector in the TEM due to X-Rays or background radiation. Hence, it is very important to remove them before further processing.

Oversampling in the energy dimension is used for outlier detection. Oversampling (using a dispersion (in eV/channel) finer than the energy resolution of the equipment) is usually undesirable because thermal noise in the CCD will add up when using more pixels to collect the same number of electrons. Here it is possible make a trade-off between some loss of SNR and a gain of spike noise detection. The dispersion is set to be several times the energy resolution. After data acquisition, a low-pass filter with cut-off frequency above the energy resolution but below the cut-off of the transfer function of CCD camera is applied to each spectrum. For example, in an EELS system with energy resolution of 0.6eV, the dispersion is set to be 0.1eV/channel. A low-pass filter with cut-off at 0.2-0.3eV/channel is then applied. The filtered spectrum is compared with the original spectrum. If the difference is greater than a threshold, such as 6σ, the data point is considered to have spike noise and it is discarded. σ^2 is estimated from the variance of a dark reference plus the Poisson shot noise.

After outlier detection, a simple spatial and energy drift correction based on cross-correlation is applied to the spectrum image. Unchanged features in the spectrum are used for reference in the cross-correlation calculation.

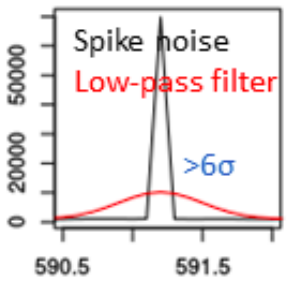

Figure 2.10. Illustration of spike noise detection.

The black line is a spectrum with spike noise. The red line is the same spectrum after low-pass filtering. The difference is greater than 6σ

2.4.3 Removal of EELS Background

The pre-edge power-law background model may not work very well for background substation when the electron dose is low. If there is not enough region for pre-edge fitting, there will be too much variation in the background. In particular, the variance will be magnified when the signal range is large comparing to the pre-edge region. Even a small variance in the pre-edge region will introduce large variance in the signal region (See figure 2.11(a)). If the pre-edge region has some feature, then a systematical bias associated with that feature will be mixed with the signal (See figure 2.11(b)). It might be unnoticeable from the spectrum itself, but it will sometimes cause the endmember extraction algorithms to fail. Error associated with the feature in the background may be regarded as a new endmember, especially when the background-to-signal ratio is high.

The solution is to use the signal region instead of using the pre-edge region for background subtraction. The algorithm presented here resolves the background subtraction problem from the point of view of signal separation. Compared with the conventional power-law background subtraction algorithm which aims to separate

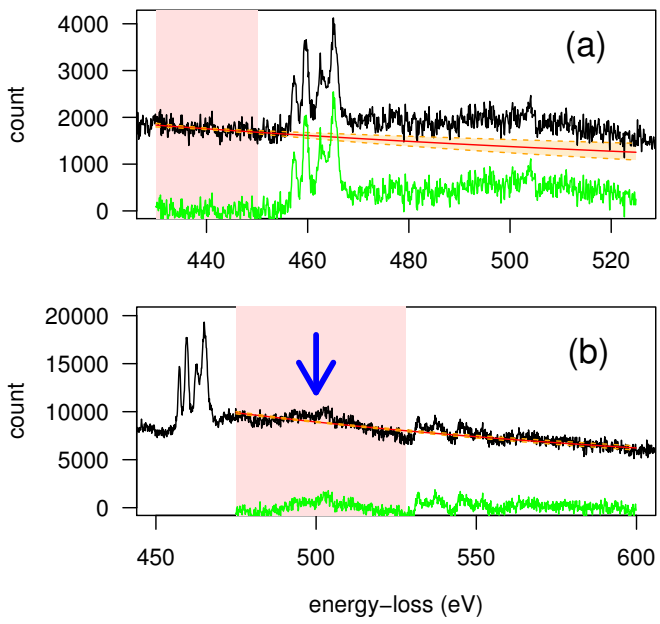

Figure 2.11. Illustration of variance and bias in power-law EELS background subtraction.

The power-law EELS background subtraction algorithm is applied to Ti-L edge and O-K edge of a $SrTiO_3$ sample. The pink box indicates the pre-edge region used to fit the power-law function, the black line is the raw EELS spectrum, the green line is the signal after background extraction. The red line is the power-law background, The orange area is the 95% confidence interval of the background. (a) Pre-edge power-law background subtraction for Ti-$L_{2,3}$ edge. The confidence interval of the background, which is also the variance of the extracted signal, becomes wider further away from the pre-edge region. (b) Pre-edge power-law background subtraction for O-K edge. Features remain in the background region, which are most likely due to plural scattering of the Ti-L edge. Features in the pre-edge region cause bias in the signal.

the exact signal and background, recovering only part of the exact signal in a linear subspace which only have the rapidly-oscillating part could be as good or even better, as long as the error and the SNR are better than the conventional method. Assume $c_{total}(E)$ is the total electron count (background plus signal) per channel at energy-loss E. $c_{total}(E)$ is the sum of the "background" (denoted by $c'_{bkg}(E)$) and the "signal"

(denoted by $c'_{signal}(E)$).

$$c_{total}(E) = c'_{bkg}(E) + c'_{signal}(E) \tag{2.46}$$

A low-order polynomial least-square fitting over the signal range can be applied instead of the normal power-law pre-edge background model. The low-order polynomial function is discarded as background and the residual of the fitting is taken as the signal. This is illustrated in figure 2.12.

$$c'_{bkg}(E) = \sum_{j=0}^{J} b_j (E - E_0)^j \tag{2.47}$$

where E_0 is the beginning of the signal range. J is a small number such as 2 or 1, depending on whether or not the 2nd term needs to be included. The residual of the polynomial fitting is considered as the "signal" ($c'_{signal}(E)$). The sum of the squared error is calculated as the sum of squared signal.

$$e = \sum_{E=E_0}^{E_1} (c'_{signal}(E))^2 \tag{2.48}$$

where E_1 is the highest energy of the signal. The fitting coefficients $b_1, \ldots, b_j$ are determined by minimizing the squared error e.

$$(b_1, \ldots, b_j) = \underset{b_1,\ldots,b_j}{\arg\min}\, e(b_1, \ldots, b_j) \tag{2.49}$$

and can be calculated by setting the gradient to zero.

$$\frac{\partial e}{\partial b_j} = 0, \quad j = 1, \ldots, J \tag{2.50}$$

The power-law background has most of its component in the 0th and 1st terms. Consider the power-law background function and expand it into a polynomial function at the beginning of the edge E_0:

$$c_{bkg}(E) = AE^{-r} \tag{2.51}$$

$$= A \sum_{n=0}^{\infty} (E - E_0)^n E_0^{-n-r} \binom{-r}{n} \tag{2.52}$$

A and r are constants defining the shape of the power-law background. The coefficients of high-order terms $AE_0^{-n-r}\binom{-r}{n}$ decay rapidly with n. Thus, low-order terms will be good approximations for the power-law background. Using the 0th and 1st order terms is usually sufficient. However, when the signal range is large, the 2nd-order term might also need to be included. The higher-order terms are so small that they can be neglected. On the other hand, the signal, which is usually rapidly varying with energy E, has both low-order terms and high-order terms.

$$c_{signal} = a_0 + a_1(E - E_0) + a_2(E - E_0)^2 + a_3(E - E_0)^3 + \ldots, \; a_j \neq 0 \tag{2.53}$$

The high-order terms in the signal will be preserved after background removal.

The theory behind this method can be explained as follows: Let V be a Hilbert space of random variables $c_{total}(E)$ with an inner product defined by

$$< c_1, c_2 >= \sum_{E=E_0}^{E_1} (c_1(E) \cdot c_2(E)) \tag{2.54}$$

Suppose W represents the space of possible polynomial estimators, spanned by $\{b_j(E - E_0)^j |\; j = 0, \ldots, J\}$. According to the orthogonality principle [210], when the squared error e reaches its minimum, the residual c'_{signal} is orthogonal to the subpace W. i.e., $c'_{bkg} \in W$, $c'_{signal} \in \overline{W}$. $\overline{W}$ is the orthogonal complement of subspace W of V.

From the approximation in equation 2.52, c_{bkg} is approximately completely in W ($c_{bkg} \in W$). So there is approximately no information about the background c_{bkg} in $\overline{W}$. i.e., the background is removed in $\overline{W}$, whereas c_{signal} has components in both W and $\overline{W}$. Its component in $\overline{W}$ is c'_{signal}. Its component in W, along with c_{bkg}, becomes c'_{bkg} and is discarded. Although other methods like pre-edge power-law fitting do not lose any component, they have the cost of introducing bias and variance from the pre-edge region.

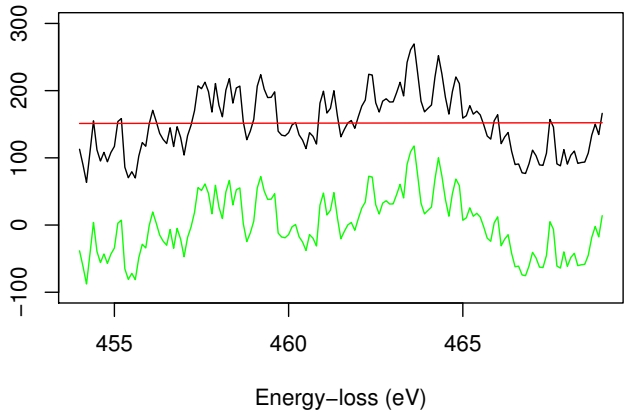

Figure 2.12. Illustration of background removal by polynomial fitting.

The total spectrum (c_{total}, shown in black) is fitted by a polynomial function (c'_{bkg}, shown in red). Here the polynomial function is a linear function. The residual (shown in green) is the signal c'_{signal}

c'_{signal} losing its component in W will not introduce error in further data processing. In the linear-mixing model described by equation 2.43, c_{signal} can be expressed as a linear combination of endmembers $m_1, \ldots, m_p$.

$$c_{signal} = \alpha_1 m_1 + \alpha_2 m_2 + \cdots + \alpha_p m_p \tag{2.55}$$

If the same polynomial background removal is also applied for every endmember $m_1, \ldots, m_p$, and the residual (signal) is $m'_1, \ldots, m'_p$. As long as none of $m'_1, \ldots, m'_p$ is zero (which is the usual case because signal is usually fast varying with E), the following equation is still valid in subspace $\overline{W}$

$$c'_{signal} = \alpha_1 m'_1 + \alpha_2 m'_2 + \cdots + \alpha_p m'_p \tag{2.56}$$

Therefore, the background removal method based on polynomial-least-squares fitting will not alter the resulting linear combination coefficients $\alpha_1, \ldots, \alpha_p$.

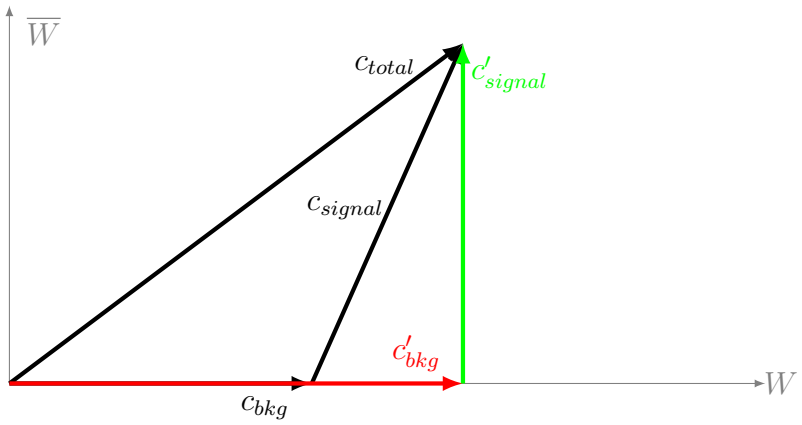

Figure 2.13. Illustration of the orthogonality principle.
Both c_{bkg} and c'_{bkg} are in W. c'_{signal} is c_{signal} projected in $\overline{W}$

In summary, in this background removal method, the space c_{total} is divided into a subspace W where c_{bkg} is located, and the orthogonal complement $\overline{W}$. Anything in W is removed as background. All of the following signal processing is done in $\overline{W}$. Bias and variance in other methods depending on pre-edge or post-edge region are avoided in this approach, at the cost of losing some signal in W, which is usually not an issue for EELS signals varying rapidly with energy loss E.

2.4.4 Dimensionality Reduction

The Principle Component Analysis (PCA) algorithm on covariance (equivalent to Singular Value Decomposition (SVD) on centered data) is used for dimensionality reduction[205]. Generally, PCA finds a set of orthogonal axes where the data have the largest variance. As a second-order statistics–based algorithm, it is desirable to make sure that the random noise variance has the same expected value everywhere in the sample space so that the PCA will not bias towards directions with more noise variance. Therefore, the electron count should be weighted by the inverse of noise

variance, which is the sum of the variance of dark noise and the variance of Poisson shot noise.

$$w_i = 1/(\sigma_{dark}^2 + \sigma_{Poisson}^2) \tag{2.57}$$

The dark noise σ_{dark} of each channel in each pixel is a fixed value for one spectrum map acquisition. Considering when the electron dose is low, the dark noise will be comparable or greater than the Poisson noise. If the jump ratio of the edge is not too high at the same time, it is expected that $\sigma_{Poisson}$ will not vary much at different channels and different pixels. For EELS data, especially 2D scans of core-loss edges, w_i can approximately be set to 1. However, for data with good SNR, weighting is required. An extreme case is when Poisson noise is dominant, such as in EDX data, weighted PCA is needed.[211–213]

Currently, only PCA is implemented in the dimensionality reduction process. When there is a non-linear signal in the hyperspectral data, such as a peak shift, PCA results in more dimensions than the actual number. Non-linear dimensionality reduction, possibly manifold learning, might be added at a later stage.

Take the simple unweighted PCA as an example. As already introduced in chapter 2.4.1, the total number of pixels is N. The total number of channels is L. r is the data matrix of dimension $L \times N$.

$$\mathbf{r} = [c'_{signal,1}, \ldots, c'_{signal,N}] \tag{2.58}$$

where each column vector $c'_{signal,n}$ is the ELNES signal in n-th pixel with background removed pixel by pixel using the polynomial least-square fitting method introduced in chapter 2.4.3.

Let $r_{l,n}$ be the matrix element of $\mathbf{r}$ at l-th row and n-th column. $\mathbf{r}_m$ is a $L \times N$

matrix with every element of l-th row being the mean value of l-th row vector of $\mathbf{r}$.

$$\mathbf{r} = [r_{l,n}]_{L\times N} \tag{2.59}$$

$$\mathbf{r}_m = \left[\frac{1}{N}\sum_{j=1}^{N} r_{l,j}\right]_{L\times N} \tag{2.60}$$

Data centering

$$\mathbf{r}_o = \mathbf{r} - \mathbf{r}_m \tag{2.61}$$

To speed up the matrix factorization, calculate the SVD on matrix $\mathbf{r}_o\mathbf{r}_o^T$ instead of PCA on $\mathbf{r}_o^T$

$$\mathbf{r}_o\mathbf{r}_o^T = \mathbf{V}\mathbf{\Sigma}^2\mathbf{V}^T \tag{2.62}$$

$\mathbf{\Sigma}^2$ is an $L \times L$ matrix with the squares of the singular values. $\mathbf{V}$ is an L by L matrix whose columns are orthogonal unit vectors. To reduce data into p dimensions, take the first p columns of matrix $\mathbf{V}$ and name it $\mathbf{V}_p$.

Project the data into p dimensions using $\mathbf{V}_p$

$$\mathbf{X}_p = \mathbf{V}_p^T\mathbf{r}_o \tag{2.63}$$

The noise level (squared error) can be estimated from the residuals in the $L - p$ space. The mean squared error (MSE) per channel per pixel is

$$e = \frac{1}{L \times N}\left(\sum_{l,n} r_{l,n}^2 - \sum_{l,n} X_{p;l,n}^2 - \sum_{l,n} r_{m;l,n}^2\right) \tag{2.64}$$

where $r_{l,n}$, $X_{p;l,n}$ and $r_{m;l,n}$ are matrix elements of $\mathbf{r}$, $\mathbf{X}_p$ and $\mathbf{R}_m$ at l-th row and n-th column.

A threshold for e can be set to determine the number of endmembers p. This threshold can be set close to $(\sigma_{dark}^2 + \sigma_{Poisson}^2)$.

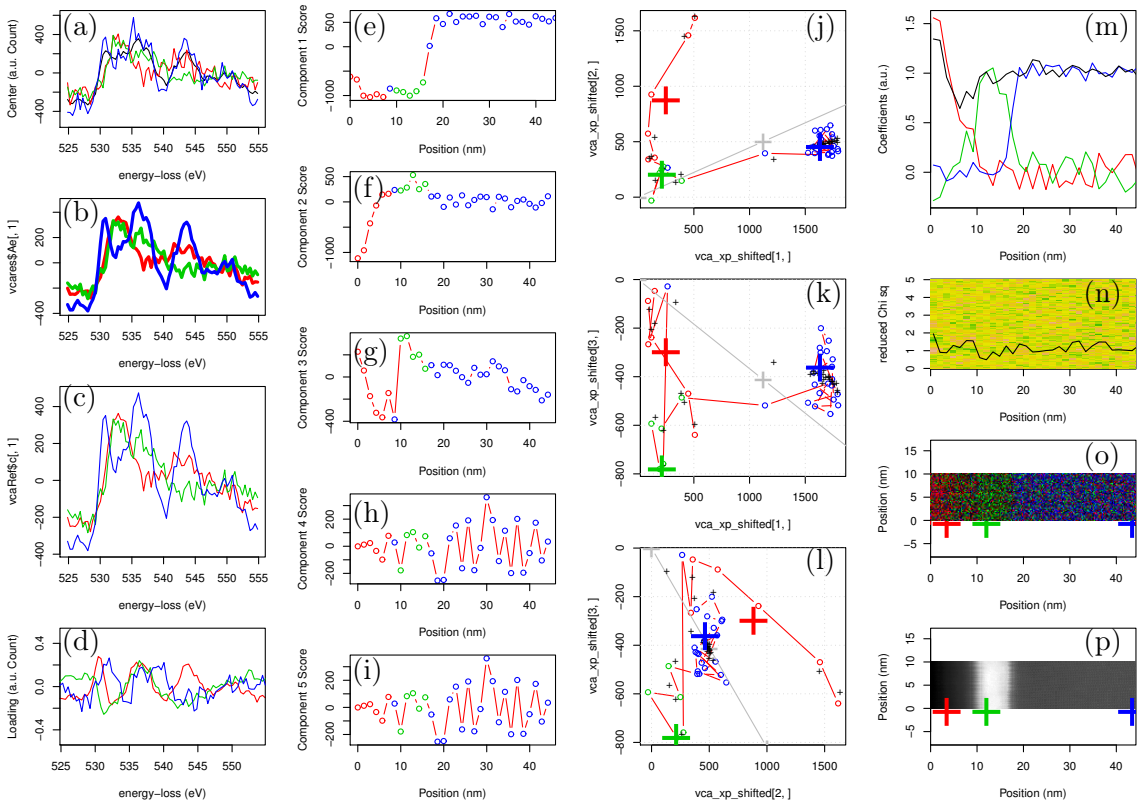

Figure 2.14. An example of hyperspectral unmixing for 3-layer oxide heterostructure.

Spectrum are collected over a 2D area and averaged along the direction of the interface. After background removal there are $N = 64$ pixels and $L = 151$ channels. (d) PCA loadings for centered spectra. (e)-(i) are 1st to 5th PCA scores. The colors of the points are from a simple k-means clustering only for reference and not used in the following processes. (j)-(l) are low-dimensional projections of the dataset. The projected plane is spanned by 1st and 2nd PCA axes for (j), by 1st and 3rd PCA axes for (k), and by 2nd and 3rd axes for (l). Color points are $\mathbf{X}'_p$. The red line connecting them shows the 1D manifold. Small black "+" are $\hat{\mathbf{X}}_{p;n}|\mathbf{X}'_{p;n}|$, showing that the bias from N-FINDR and k-NN canceled each other. $p = 3$ endmembers are identified. Large color "+" are endmembers identified by N-FINDR. (a) endmember signatures in L dimensional space (in $\mathbf{r}$). (b) same endmember signatures with noise in the null space being removed by PCA. i.e. $\mathbf{X}_p + \mathbf{r}_m$. (c) same endmember signatures, with noise removed by PCA, and then scaled by λ_q. The endmembers in (c) is used for fitting. (m) fitting coefficients of the data averaged along the direction of the interface, which can be regarded as a density profile of each species. The line in (n) is the χ^2 statistic. The terrain map is the residual plot. (o) fitting coefficients for the 2D data in false color map. Large color "+" show positions of endmembers identified. (p) is the corresponding HAADF image acquired simultaneously with the spectral map. Large color "+" show the positions of the endmembers.

2.4.5 Endmember Extraction

Dimensionality reduction algorithms such as PCA give the best p-dimensional subspace of the original L-dimensional spectral data vectors in terms of preserving the variance of the signal. However, the axes (principal components) of PCA are required to be orthogonal and therefore might not have physical meaning. Figure 2.14(d) shows PCA loadings and Figures 2.14(e)-(i) show PCA scores. They are a mixture of several physical effects and difficult to interpret. Endmember extraction will find p linearly independent (but not necessarily orthogonal) vectors in the signal space, which satisfies equation 2.43. They usually have physical meaning because they also have the constraints in equation 2.44 and 2.45

Although dimensionality reduction is not a prerequisite for endmember extraction, it is desirable to do endmember extraction in the low-dimensional subspace. First, the noise in the null space is removed. Second, Euclidean distance does not work well in high dimensions.

The N-FINDR algorithm[209] is used for endmember extraction. Other algorithms like VCA[214] are also tried but N-FINDR gives best accuracy. Although N-FINDR has speed issues on large data sets, EELS spectra have $\sim 10^3$ data points, so that N-FINDR can finish within several seconds using the single-replacement iterative N-FINDR (1-IN-FINDR)[205]. N-FINDR is a simplex based algorithm. It assumes all the endmembers are in the data sample set. It will maximize the volume of the p-vertex simplex formed by any set of p data sample vectors.

Here, a modified N-FINDR algorithm is used. For p endmembers, the data dimensionality is reduced from L to p instead of $p-1$ in the dimensionality reduction step. Because the data is centered before PCA, the original zero point can also be

project into the p dimension subspace. In L-dimensional space centered at $\mathbf{r}_m$, the zero point of original data is at $-\mathbf{r}_m$. Project it onto the p-dimensional space. The data points projected in the p-dimensional space are then being translated so that the projected zero point is again at the origin in the p-dimensional space.

$$\mathbf{X}'_p = \mathbf{X}_p - \mathbf{V}_p^T(-\mathbf{r}_m) \tag{2.65}$$

Note that steps from equation 2.60 to 2.65 are different from simply doing SVD on non-centered data $\mathbf{r}$ because the p-dimensional subspace derived from SVD in equation 2.62 would be different.

Normalize all data vectors so that the Euclidean norm of every data vector becomes 1. i.e., project all data points to a hypersphere with radius of 1.

$$\mathbf{X''}_{p;n} = \frac{\mathbf{X}'_{p;n}}{|\mathbf{X}'_{p;n}|} \tag{2.66}$$

$\mathbf{X''}_{p;n}$ and $\mathbf{X}'_{p;n}$ are the n-th column of $\mathbf{X''}_p$ and $\mathbf{X}'_p$. $\mathbf{X''}_p$ is the normalized data matrix. $|\cdot|$ is the Euclidean norm.

The $p-1$ dimensional space on the hypersphere is the subspace N-FINDR algorithm works in later. This subspace only has information about the shape of the spectrum. Because the Euclidean norm of all data points is re-scaled to 1, amplitude information is not in this subspace. Therefore, we can exclude the effect of amplitude change and focus on the shape of the spectrum. However, a side effect comes. After the step in equation 2.66, the noise variance is not normalized on the hypersphere. Data points with low SNR will be magnified and therefore big errors will be introduced. Simplex volume-based algorithms such as N-FINDR will be affected by noise and introduce bias.

In additional to this problem, there is an inherent problem of N-FINDR. Because N-FINDR always find the simplex with maximum size, the endmembers found by N-

FINDR will always bias towards the outside part of the simplex when noise is present. This problem becomes very obvious for ELNES data due to low signal-to-noise ratio, especially worse when the concentration of the element is low, giving a close-to-zero SNR.

To resolve the two problems at one time, a transformation similar to weighted k-nearest neighbors (k-NN) regression[215] is applied to every data point $\mathbf{X''}_{p;n}, n = 1, \ldots, N$ before endmember extraction.

$$\hat{\mathbf{X}}_{p;n} = \sum_{j=1}^{N} w_j \mathbf{X''}_{p;j} \tag{2.67}$$

The $\sum_{j=1}^{N}$ is summing over all data points (pixels), including the n-th data point itself. In practice, a threshold distance can be defined and only the points within the threshold distance are calculated. Points at large distances will have very small weight.

The weight w_j has two parts $w_{j,1}$ and $w_{j,2}$. $w_{j,1}$ and $w_{j,2}$ is combined using

$$w_j = \frac{w_{j,1} w_{j,2}}{\sum_{n=1}^{N} w_{j,1} w_{j,2}} \tag{2.68}$$

$w_{j,1}$ is the weight decays exponentially with distance.

$$d_{n,j} = |\mathbf{X''}_{p;j} - \mathbf{X''}_{p;n}| \tag{2.69}$$

$$w_{j,1} = \exp(-\frac{d_{n,j}|\mathbf{X'}_{p;n}|}{a\sqrt{ep}}) \tag{2.70}$$

Ideally, the spherical distance on the hypersphere should be used instead of the Euclidean distance in equation 2.69. However, the Euclidean distance is a good approximation considering only small d is contributing $w_{j,1}$. In equation 2.70, the term $\sqrt{ep}$ scales the standard error $\sqrt{e}$ per channel per pixel into p dimensions for $|\mathbf{X'}_{p;n}|$ in p dimensions. $d_{n,j}|\mathbf{X'}_{p;n}|$ scales the distance $d_{n,j}$ from the space on the hypersphere

back to the space near $\mathbf{X}'_{p;n}$. a is a constant which will be explained in the last part of this section.

$w_{j,2}$ is the inverse-variance weight.

$$w_{j,2} = |\mathbf{X}'_{p;j}| \tag{2.71}$$

The N-FINDR is then performed on the hypersphere for dataset $\{\hat{\mathbf{X}}_{p;n}|n = 1,\ldots,N\}$ using the simplex volume on the hypersphere. The volume on the hypersphere is calculated using formulas in Ref.[216]. Let $\{\mathrm{em}(q)|q = 1,\ldots,p\}$ represents the index of the endmembers N-FINDR found from the columns of $\hat{\mathbf{X}}_p$. Now project $\mathbf{X}_p$ back into L dimensions using $\mathbf{V}_p$,

$$\mathbf{X} = \mathbf{V}_p\mathbf{X}_p \tag{2.72}$$

$\mathbf{X}$ can be considered as $\mathbf{r}_o$ with noise removed by PCA. Corresponding $\{\mathrm{em}(q)|q = 1,\ldots,p\}$ columns in $\mathbf{X}$ are the p endmember signatures $\{\gamma_q\mathbf{X}_{\mathrm{em}(q)}|q = 1,\ldots,p\}$. γ_q is a scaling factor which will be explained later.

The endmembers can then be taken as the basis of the p dimensional space and decompose other data points into the form of equation 2.56. In order to do semi-quantification, the ELNES cross-section in the same core-loss edge is assumed to be the same regardless of the difference in shape due to different oxidation states or chemical environment. Then, if the corresponding ELNES signal for different endmembers have the same total electron count, the linear combination coefficients $\alpha_1,\ldots,\alpha_p$ in equation 2.56 are directly proportional to the area density of each endmember species. However, the endmembers N-FINDR found are directly derived from the dataset. They need to be scaled by

$$\gamma_q = 1/\sum_{E=E_0}^{E_1} c_{signal;q}(E) \tag{2.73}$$

$c_{signal;q}(E)$ is the electron count per channel in the em(q) data point that corresponds to the q-th endmember. $c_{signal;q}(E)$ is derived from regular power-law background model so that the count have physical meaning. Then a multiple linear least square (MLLS) fitting can be done for each column of $\mathbf{r}_o$, as shown in Figure 2.14(m) and (o). In equation 2.56 again,

$$c'_{signal,n} = \mathbf{r}_{o;n} \tag{2.74}$$

$$m'_q = \mathbf{X}_{em(q)} \tag{2.75}$$

where $n = 1, \ldots, N$, $q = 1, \ldots, p$. The resulting $\alpha_1, \ldots, \alpha_p$ will be exactly the same as doing decomposition using basis $\{\mathbf{X}_{p;em(q)} | q = 1, \ldots, p\}$ for data $\{\mathbf{X}_{p;n} | n = 1, \ldots, N\}$ in p dimensional space, except that the residual can be derived in L dimensional space.

The weighting algorithm can be understood as a trade-off between bias introduced by N-FINDR and k-NN. Bias is not avoidable in either case. However, N-FINDR always biases towards outside the simplex, while k-NN always biases towards areas with more data points, which is usually inside the simplex. When combined, bias can be limited within an acceptable range in most cases. The following part will explain how to choose a in equation 2.70 so that the combination of the two biases can be minimized.

Assume any the data points is a ground truth plus a random noise with squared-error e. The ground truths near the endmembers are always on a low-dimensional manifold of dimension t. This can be ensured by slight oversampling during spectral line-scan or map data collection. Choose the distance between two adjacent pixels always being smaller than the smallest feature on the sample, which is usually limited by the spatial resolution of the scope. For a 2D scan, $t \leq 2$. For a line-scan, $t \leq 1$.

Assume the ground truths on the manifold are evenly distributed on the manifold within the simplex. This is a loose restriction. Later it will be shown that even if

the distribution deviates from this assumption, the result will not be altered much. Choose an arbitrary axis $\mathbf{x}$ which is not perpendicular to the manifold and let the ground truth of the endmember be located at zero point. Assume the simplex where all ground truths are located is at the $x > 0$ part. Thus, for every ground truth position $x_{\text{true}} > 0$. The position of the data point with noise is $x = x_{\text{true}} + x_{noise}$

First, consider the case $t = 0$. Data points near the endmember follow a Gaussian distribution with variance e. The density of the data point can be expressed as

$$f_{t=0}(x) = \frac{1}{\sqrt{2\pi e}} \exp\left[-\frac{x^2}{2e}\right] \tag{2.76}$$

Then assign each data point j with weight $w_{j,1}$

$$w_{j,1} = \exp\left[-\frac{x_j}{a\sqrt{e}}\right] \tag{2.77}$$

and sum up all points using equation 2.67, The weight-averaged position $\hat{x}$ is

$$\hat{x} = \frac{\sum_j w_{j,1} x}{\sum_j w_{j,1}} \tag{2.78}$$

$$\lim_{N\to+\infty} \hat{x} = \frac{\int_{-\infty}^{\infty} w_1(x) x f_{t=0}(x) dx}{\int_{-\infty}^{\infty} w_1(x) f_{t=0}(x) dx} \tag{2.79}$$

$$= \frac{\int_{-\infty}^{\infty} \exp\left[-\frac{x}{a\sqrt{e}}\right] x \frac{1}{\sqrt{2\pi e}} \exp\left[-\frac{x^2}{2e}\right] dx}{\int_{-\infty}^{\infty} \exp\left[-\frac{x}{a\sqrt{e}}\right] \frac{1}{\sqrt{2\pi e}} \exp\left[-\frac{x^2}{2e}\right] dx} \tag{2.80}$$

$$= -\frac{1}{a}\sqrt{e} \tag{2.81}$$

If a is set to 1, the bias will be $-\sqrt{e}$, and the bias will converge with increasing number of data points. On the contrary, if the weighting algorithm is not applied, the probability that the extreme value exceeds $1.65\sqrt{e}$ will be greater than 50% when there are as few as $N > 4$ data points near the ground truth of the endmember, and the bias will get even worse with increasing N.

Second, consider the case $t \geq 1$ The density of the data points can be expressed as a convolution of x^{t-1} and a Gaussian function with variance e.

$$f_t(x) \propto \int_0^\infty x^{t-1} \frac{1}{\sqrt{2\pi e}} \exp\left[-\frac{(x-s)^2}{2e}\right] ds \tag{2.82}$$

where x^{t-1} is the density of points, which are originally in t dimensional manifold and evenly distributed within a simplex, projected onto one dimensional x axis. Similar to equation 2.79, but let the expected value of position

$$\hat{x} = 0 \tag{2.83}$$

Because the ground truth of the endmember is at zero, the bias is also the expected value of weight-averaged position, calculated as follows,

$$\hat{x} = \frac{\int_{-\infty}^{\infty} w_1(x) x f_t(x) dx}{\int_{-\infty}^{\infty} w_1(x) f_t(x) dx} \tag{2.84}$$

Combine equation 2.77, 2.82, 2.83 and 2.84, gives

$$a = \frac{1}{\sqrt{t}} \tag{2.85}$$

in this condition, the bias is zero.

Now consider the assumptions that the ground truths are in t dimensional manifold and evenly distributed. If the assumptions do not hold, it affects the $\mathbf{x}$ projected density x^{t-1}. Now assume $a = \frac{1}{t_1}$. The real projected density is x^{t_2-1}. (If the assumption that data is evenly distributed is also not true, simply expand the distribution into sum of polynomial terms $x^0, \ldots, x^{t_2-1}$. The numerator and denominator in equation 2.84 will be expanded, the resulting $\hat{x}$ should be in between the ones calculated by individual terms.) Substitute $t = t_1$ into equation 2.82. Substitute $t = t_2$ into equation 2.85. Then combining equation 2.77, 2.82, and 2.84, gives

$$\hat{x} = \frac{t_2 - t_1}{\sqrt{t_1}} \sqrt{e} \tag{2.86}$$

Therefore, no matter the real dimension of the manifold near the endmember is 1 or 2, choosing $a = 1$ or $a = 1/2$ can both guarantee the bias to be within $\pm\sqrt{e}$.

2.4.6 Goodness of Fit

The error analysis is done in the L-dimensional space. Both the χ^2 test and the visualized residual plot are used. In a good fit, reduced χ^2 should be close to 1 and there should be no pattern appearing in the residual plot. Example of the χ^2 statistic and the residual plot are shown in Figure 2.14(n).

2.5 First-Principles Calculations

First-principles calculations are widely used in materials research, and in combination with electron microscopy. First-principles (*Ab-initio*) refers to calculations on the basis of quantum-mechanical considerations without using high-order parameters. The density functional theory (DFT) calculations are heavily used in this research.

2.5.1 Hohenberg-Kohn-Sham Theory

Directly solving the N-body Schrödinger equation is impossible for the coupled electron-ion system in materials. The Born-Oppenheimer approximation considers that the time scales of nuclear and electronic motions are vastly different, so the two can be decoupled. The total wavefunction can be separated into the electron wavefunction $\psi(x, \mathbf{R})$ and the nuclear wavefunction $\chi(\mathbf{R})$.[217]

$$\phi(x, \mathbf{R}) = \psi(x, \mathbf{R})\chi(\mathbf{R}) \tag{2.87}$$

Electronic eigenvalue $\varepsilon_n(\mathbf{R})$ depends parametrically on the ionic positions $\mathbf{R}$. The ions feels the Hellmann-Feynman force, given by the expectation value of the gradient of the electronic Hamiltonian in the ground state. Kohn and Hohenberg proved that the effective single electron potential is uniquely determined by an electron density. The Hohenberg-Kohn-Sham (HKS) theorem states,[218]

(1) The ground-state energy of a many-body system is a unique functional of the particle density

$$E_0 = E[n(\mathbf{r})] \tag{2.88}$$

(2) The functional $E[n(\mathbf{r})]$ has its minimum relative to variations $\delta n(\mathbf{r})$ of the particle density $n(\mathbf{r})$ at the equilibrium density $n_0(\mathbf{r})$,

$$E = E[n_0(\mathbf{r})] = \min\{E[n(\mathbf{r})]\} \tag{2.89}$$

$$\frac{\delta E[n(\mathbf{r})]}{\delta n(\mathbf{r})}\Big|_{n(\mathbf{r})=n_0(\mathbf{r})} = 0 \tag{2.90}$$

which subject to the constraint

$$\int n(\mathbf{r}) d^3r = N \tag{2.91}$$

This gives

$$\frac{\delta}{\delta n(\mathbf{r})}[E[n(\mathbf{r})] - \lambda\left(\int n(\mathbf{r}) d^3r - N\right)]\Big|_{\lambda, n(\mathbf{r})=\lambda_0, n_0(\mathbf{r})} = 0 \tag{2.92}$$

For N-electron system, $V(\mathbf{r})$ is the external potential, $n(\mathbf{r})$ is the electron density. Kohn and Sham give the total energy functional $E[n]$ into the functional of electron density as follows,[219]

$$E[n] = T[n] + E^H[n] + E^{xc}[n] + \int V(\mathbf{r}) n(\mathbf{r}) d^3r \tag{2.93}$$

where $T[n]$ is the kinetic energy term, $E^H[n]$ is the Hartree energy (electron electron repulsion energy), representing the long-range interactions between electrons

$$E^H[n] = \frac{e^2}{2} \iint \frac{n(\mathbf{r})n(\mathbf{r}')}{|\mathbf{r} - \mathbf{r}'|} d^3r d^3r' \tag{2.94}$$

$E^{ex}[n]$ is the exchange-correlation energy. According to Hohenberg-Kohn theorem, variation of the total energy $E[n]$ with electron density $n(\mathbf{r})$ gives all ground-state properties. The problems then turns into finding $T[n]$ and $E^{xc}[n]$.

For electron density n, consider a reference system without electron-electron interaction. The electron density is the sum of square of all single-electron orbitals.[219]

$$n(\mathbf{r}) = \sum_i |\phi_i(\mathbf{r})|^2 \tag{2.95}$$

The non-interaction kinetic energy based on $\phi_i(\mathbf{r})$ is[219]

$$T[n] = T_0[n] = \sum_i \int \phi_i^*(\mathbf{r}) \left(-\frac{\hbar^2}{2m} \nabla^2 \right) \phi_i(\mathbf{r}) d^3r \tag{2.96}$$

E^{xc} can be estimated from the reference system with similar electron density. The Local Density Approximation (LDA) gives,[220]

$$E^{xc}[n(\mathbf{r})] = \int n(\mathbf{r}) \varepsilon_{xc}[n(\mathbf{r})] d^3r \tag{2.97}$$

The Generalized Gradient Approximation (GGA) gives,[220]

$$E^{xc}[n(\mathbf{r})] = \int n(\mathbf{r}) \varepsilon_{xc}[n(\mathbf{r}), \nabla n(\mathbf{r}), \dots] d^3r \tag{2.98}$$

ε_{xc} have a lot of different forms such as PW91[221], PBE[222, 223], etc.

The minimum of energy is achieved by determining the optimal one-electron orbitals using the variational condition under constraint.[219]

$$\delta \left\{ E[n(\mathbf{r})] - \sum_{i,j} \varepsilon_{i,j} \left(\langle \phi_i | \phi_j \rangle - \delta_{i,j} \right) \right\} = 0 \tag{2.99}$$

$$\langle \phi_i | \phi_j \rangle = \delta_{i,j} \tag{2.100}$$

After diagonalizing $\varepsilon_{i,j}$ the Kohn-Sham equations is derived.

$$\left\{-\frac{\hbar^2}{2m}\nabla^2 + V(\mathbf{r}) + e^2\int\frac{n(\mathbf{r})}{|r-r'|}d^3r + \mu_{xc}[n(\mathbf{r})]\right\}\phi_i(\mathbf{r}) = \varepsilon_i\phi_i(\mathbf{r}) \tag{2.101}$$

with the exchange-correlation potential

$$\mu_{xc}[n(\mathbf{r})] = \frac{\delta E_{xc}[n(\mathbf{r})]}{\delta n(\mathbf{r})} \tag{2.102}$$

The total energy can be calculated as

$$E = \sum_i \varepsilon_i - \frac{1}{2}\iint\frac{n(\mathbf{r})(r')}{|r-r'|}d^3rd^3r' + \int n(\mathbf{r})\{\varepsilon_{xc}[n(\mathbf{r})] - \mu_{xc}[n(\mathbf{r})]\}d^3r \tag{2.103}$$

Where the first term is the sum of single electron energy, the second term is the double-counting corrections.

2.5.2 Numerical Solutions of Kohn-Sham Equations and Software Packages

Using the plane-wave basis to expand the wavefunction is convenient. Plane-wave periodic boundary conditions (PBC) and fast fourier transformation (FFT) are used. The efficiency of numerical calculation is high.[224]

According to the Bloch Theorem in crystallography,

$$\psi_{n,k} = u_{n,k}(\mathbf{r})e^{i\vec{k}\cdot\vec{r}} \tag{2.104}$$

$u_{n,k}(\mathbf{r})$ has the same periodicity with lattice potential. Doing Fourier expansion for $u_{n,k}$

$$u_{n,k}(\mathbf{r}) = \frac{1}{\Omega^{1/2}}\sum_G C_{Gnk}e^{i\vec{G}\cdot\vec{r}} \tag{2.105}$$

$$n(\mathbf{r}) = \sum_G n_G e^{i\vec{G}\cdot\vec{r}} \tag{2.106}$$

$$V(\mathbf{r}) = \sum_G V_G e^{i\vec{G}\cdot\vec{r}} \tag{2.107}$$

There are an infinite number of plane waves in the complete basis. However, in reality only the plane waves meeting the following condition are calculated.[224]

$$\frac{\hbar^2}{2m_e}|G+k| < E_{\mathrm{cut-off}} \tag{2.108}$$

Figure 2.15 is the scheme of Kohn-Sham method[225]. It is a self-consistent method. The Hamiltonian in the Kohn-Sham equation is the functional of the electron density. The electron density is calculated from the wavefunction, which is solved from the Kohn-Sham equation.[225]

$$\begin{array}{ccccccc}
V_{ext}(\mathbf{r}) & \underset{HK}{\Leftarrow} & n_0(\mathbf{r}) & \Leftrightarrow & n_0(\mathbf{r}) & \underset{HK}{\Rightarrow} & V_{KS}(\mathbf{r}) \\
\Downarrow KS-eq & & \Uparrow & & \Uparrow & & \Downarrow KS-eq \\
\psi(\{r_i\}) & \Rightarrow & \psi_0(\{r\}) & & \psi_{i=i,\cdots,N}(\{r\}) & \Leftarrow & \psi_i(\mathbf{r})
\end{array}$$

Figure 2.15. Scheme of Kohn-Sham method

HK represents Hartree potential. $KS-eq$ represents the Kohn-Sham equation. This figure is reproduced from Ref.[225]

The real Coulomb potential is very deep near the nucleus, causing the wavefunctions to oscillate near the nucleus. Plane waves with very high k must be included in order to maintain numeric accuracy. There are two approaches to solve this issue. The linearized-augmented plane-wave (LAPW) method and the pseudo-potential method. In this dissertation research, both methods are used.

In the LAPW method, the space is devided into non-overlapping atomic spheres (the muffin-tin (MT) region) and an interstitial region. Inside the atomic sphere with radius R_t, a linear combination of radial functions times spherical harmonics $Y_{lm}(r)$ is

used. In the interstitial region, a plane wave expansion is used.[226, 227] Software packages such as WIEN2k[227] and Elk[228] implement the LAPW method.

The pseudopotential (PP) method can significantly reduce the complexity of numerical calculations. The frozen core approximation is used in which the core electrons are pre-calculated in an atomic environment, and kept frozen in the course of the remaining calculations.[224] Inside the atomic-centred spheres, a "soft" pseudo-wavefunction is used with polynomials[229] or spherical Bessel-functions (by RRKJ in Ref.[230]) The latter is more commonly used. There are different approaches to construct the pseudo-wavefunctions, including normconserving pseudopotentials (NC-PP), ultrasoft pseudopotentials (US-PP) and projector augmented-wave method (PAW). The pseudopotential is "softer" than the Coulomb potential and the wavefunction becomes node-less pseudo-wavefunction. Therefore, a smaller $E_{\mathrm{cut-off}}$ can be used. Software packages such as VASP[231] and QUANTUM-ESPRESSO (QE)[232] implement the pseudopotential method. Usually more than one type of pseudopotential is available for each atomic species in each software package. In this dissertation research, PAW is used for VASP, while GBRV[233], which is a variant of US-PP, is used for QE. The Materials Project[234] and the Standard Solid State Pseudopotentials (SSSP)[235] are taken as reference for choosing pseudopotentials.

2.5.3 Hubbard U Correction

There are limitations for the DFT methods introduced above. The HKS theorem is not valid for excited states so it usually underestimates the band gap. LDA and GGA functionals still neglect strong correlations in d and f electrons so exchange-splitting is usually underestimated. One solution is using hybrid functionals[236], such as

B3LYP[237], PBE0[238] and HSE[239], which incorporate a portion of exact exchange from Hartree-Fock theory. However, calculating the non-local Fock exchange is slow. Another approach is to use empirical parameters U and J to describe the Coulomb repulsive force.[240] The Hubbard-Hamiltonian becomes

$$H = \frac{U}{2} \sum_{m,m',s} n_{m,s} n_{m',-s} + \frac{U-J}{2} \sum_{m \neq m',s} n_{m,s} n_{m',s} \tag{2.109}$$

where $n_{m,s}$ is the number operator for electrons with the magnetic quantum number m and spin s.

For oxygen-deficient $SrTiO_3$, or Mott insulators such as $LaTiO_3$, the LDA+U correction is necessary for predicting the splitting of the $3d$ band, although accurately predicting the gap between O-$2p$ and Ti-$3d$ still requires hybrid functional calculations. Different choices of U sometimes strongly vary the predicted properties of the 2DEG.[30, 48–50, 66, 71, 91, 92] Therefore, calculations with different U values are performed and compared for each atomic structure.

2.5.4 Structural Model

For calculating the interface and surface structure, supercell models with slabs are built. The c axis of the supercell is the film growth direction and is relatively long. a and b of the supercell are the same as the lattice parameter. The substrate material is put at the center of the supercell, the film is built symmetrically above and below the substrate, in order to avoid polarization or electric field buildup. The top and bottom parts of the supercell are vacuum with a thickness of at least 5Å. Considering the periodic boundary condition, the slabs are separated by at least 10Å of vacuum. The short range interaction can be neglected. For structures with $SrTiO_3$ substrate, a and b in the supercell are chosen to be about 5.6Å, which is $\sqrt{2}$ times the cubic $SrTiO_3$

lattice parameter so that possible antiferrodistortion is taken into consideration and oxygen deficiency can be varied.

2.6 Image, Spectrum and Phase Simulation

2.6.1 TEM and STEM Image Simulation

The multi-slice method (described in Ref.[241]) implemented by the Dr.Probe software package[242–244] has been used for both TEM and STEM image simulations. In the multi-slice method, the specimen is split into thin slices. The wave propagation inside each slice is simulated using approximations in equation 2.2 to 2.5. In between slices, the Fresnel propagator is used.

$$f(x, y, z + u) = \frac{1}{i\lambda u} f(x', y', z) \otimes \exp\left(\pi i k \frac{x^2 + y^2}{u}\right) \tag{2.110}$$

where u is the distance between slices.

For thermal diffuse scattering (TDS, discussed in chapter 2.1.2) simulations, the frozen-lattice (or "frozen-phonon") method[245], in which different frozen states of the crystal lattice are calculated using the multi-slice method and then averaged for each pixel and slice, is very time-consuming. A time-efficient implementation of the multi-slice algorithm is applied by Dr.Probe, in which different frozen states are randomly assigned to different pixels and slices.[243] The simulation speed is significantly improved.

2.6.2 Spectrum Simulation

As already mentioned in chapter 2.3.1.1, the shape of the Ti white lines are dominated by the multiplet effect.[198, 199] The Ti-L edge of $SrTiO_3$ is simulated using multiplet simulation implemented by software package multiX[246], taking polarization (for X-Ray), Coulomb, spin-orbit and crystal-field interactions into consideration. MultiX is originally designed for X-ray absorption spectroscopy (XAS) and resonant inelastic x-ray scattering (RIXS) simulations. Considering that ELNES is the counterpart of XAS in electron microscopy, the simulation results from MultiX are also valid for ELNES. In principle, it can also simulate electron magnetic circular dichroism (EMCD, as a counterpart to X-ray magnetic circular dichroism) and momentum-resolved ELNES (as a counterpart of the X-ray linear dichroism).

Since the O-K edge is a good approximation to the projected density of state (PDOS) at the oxygen atom[204], the PDOS of each atom is calculated using DFT and compared with the O-K ELNES.

2.6.3 Electric Potential and Polarization Calculations

Mean Inner Potential

The mean inner potential (MIP, discussed in chapter 2.2.1) can be calculated by averaging the Coulomb potential inside the material using equation 2.39. In chapter 2.5.2, it was discussed that the pseudopotential used in some DFT software packages is not the same as the real Coulomb potential inside the atomic spheres. And there is currently no software interface that can transform the pseudo-wavefunctions back to real wavefunctions. Therefore, the full potential (FP) LAPW method, which

calculates the full Coulomb potential and all-electron wavefunction, is necessary for MIP simulation. A slab model is built and the Coulomb potential in the vacuum far away from the surface is used as the zero reference. This method has been used for calculating the MIP of several II-VI semiconductors[247]. The LAPW5 program[227] in WIEN2k software package can calculate the Coulomb potential (without the exchange-correlation term) in real space. Set IPRINT tag to R2V in input file "case.in0" to allow LAPW0 program to generate the output file "case.vcoul". Then use LAPW5 program to calculate the Coulomb potential in a specific lattice plane. The program GO_LAPW5[248] is a script that run LAPW5 at a series of crystal planes parallel to each other and take the average. Since the script GO_LAPW5 in Ref.[248] is not released in public, a small script that can run LAPW5 in parallel has been written. It averages the Coulomb potential using equation 2.39 inside the vacuum and the material, respectively. This should be exactly the same as GO_LAPW5. The mesh is slightly shifted from the origin in order to avoid any potential singularity at atomic positions.

Born Effective Charge

While the atomic displacements can be estimated from the TEM/STEM images, the Born effective charge links the atomic displacement in the unit cell with the macroscopic polarization. The Born effective charge tensor is defined as[249]

$$Z^*_{\nu,ij} = \frac{\Omega}{|e|}\frac{\partial \mathbf{P}^i_t}{\partial \mathbf{r}^\nu_j} \tag{2.111}$$

where Ω is the unit cell volume, $\mathbf{P}^i_t$ is the total polarization in direction i, and $\mathbf{r}^\nu_j$ is the coordinate of ion v in direction j. The Born effective charge often differs from the nominal ionic charge. In ferroelectric materials, it is often greater than the nominal ionic charge.

The Born effective charge is calculated by using a small displacement method.[232]

$$\frac{\partial \mathbf{P}_t^z}{\partial \mathbf{r}_z^\nu} = \frac{\Delta \mathbf{P}_t^z}{\delta} \approx \frac{\mathbf{P}_t^z(+\delta\hat{z},\nu) - \mathbf{P}_t^z(-\delta\hat{z},\nu)}{2\delta} \tag{2.112}$$

The total polarization difference can be divided into the ionic and electron part

$$\Delta \mathbf{P}_t^z = \Delta \mathbf{P}_{ion}^z + \Delta \mathbf{P}_e^z \tag{2.113}$$

The ionic part is given by

$$\Delta \mathbf{P}_e^z = \frac{|e| Z_\nu \delta}{\Omega} \tag{2.114}$$

where Z_ν is the valence atomic number of pseudoatom ν.

The electronic contribution is calculated using the Berry phase technique.[250] (Details are in the modern theory of polarization.[251])

$$\Delta \mathbf{P}_e^z = \mathbf{P}_e(+\delta\hat{z},\nu) - \mathbf{P}_e(-\delta\hat{z},\nu) \tag{2.115}$$

with

$$\mathbf{P}_e^\lambda = -\frac{if|e|}{8\pi^3} \sum_{n=1}^{M} \int_{BZ} d^3k < u_{nk}^{(\lambda)} | \nabla_k | u_{nk}^{(\lambda)} > \tag{2.116}$$

where λ parameterizes changes in potential such as atomic displacement of δ, $u_{nk}^{(\lambda)}$ is the cell-periodic part of the Bloch wavefunction $\psi_{nk}^{(\lambda)}$, and the sum is over M bands.[252, 253]

In this dissertation research, the Born effective charge in strained $SrTiO_3$ and strained $BaTiO_3$ in $BaTiO_3/SrTiO_3$ system have been calculated. The results are then compared with reported values,[254–256] except that the calculations here cover a larger strain range to fit the epitaxial strain values at $BaTiO_3/SrTiO_3$ and $SrTiO_3$/Ge interfaces.

Lattice relaxation in DFT can give the relative displacements of different atomic species and their ratios. Therefore the atomic displacement for a specific polarization density can be calculated by using the Born effective charge, or vice versa.

As discussed above, the atomic displacement is directly related to polarization density by Born effective charge. In chapter 2.1.3 and 2.6.1, it has already been discussed that the apparent atomic column displacements can be measured from the image and compared with image simulations. In this dissertation, a series of atomic models with different strain has been built. Ionic relaxation of these models are done using DFT and atomic displacements, and the Born effective charges are obtained. The relaxed models are then used as input of image simulation. The simulated images are compared with experimental ones. The predicted polarization density is also calculated and compared with the electrical measurements. Thus, electrical measurements and microscopy measurements are connected together by first-principles calculations.

Chapter 3

INVESTIGATING THE γ-Al_2O_3/$SrTiO_3$ INTERFACE

The γ-Al_2O_3/$SrTiO_3$ interface displays a two-dimensional electron gas (2DEG) depending on growth conditions and film thickness, which however disappears when samples are annealed in oxygen.[28, 55, 57] The 2DEG has high mobility $\sim 10^4 \mathrm{cm}^2\mathrm{V}^{-1}\mathrm{s}^{-1}$ at low temperature and high carrier density $\sim 10^{14}\mathrm{cm}^{-2}$ at room temperature. Samples grown by ALD at low temperature[57] and MBE at high temperature[55] show slightly different electrical behavior These properties will be investigated and explained in this chapter.

The first section of this chapter reports spectrum and phase mapping across the epitaxial γ-Al_2O_3/$SrTiO_3$ interface. The spectrum mapping was done using the conventional MLLS method as described previously. These spectrum and phase mapping results from γ-Al_2O_3/$SrTiO_3$ have already been published[257]. The second part of this chapter involves other techniques and methods that provide further and more detailed analysis, including ELNES hyperspectral unmixing, electron holography, DFT and spectrum simulations. By combining experimental results and simulations, the analysis explains the role of oxygen vacancies in the formation of the high mobility 2DEG, and the origin of the critical thickness.

The samples investigated were provided by our collaborators at the University of Texas-Austin.

3.1 Spectrum and phase mapping across the epitaxial γ-Al_2O_3/$SrTiO_3$ interface

3.1.1 Introduction

In this study, a range of electron microscopy techniques, including aberration-corrected negative-Cs imaging (NCSI), high-angle annular-dark-field (HAADF) imaging, off-axis electron holography, and energy-loss near-edge structure (ELNES) analysis, have been used to characterize the nature of γ-Al_2O_3/$SrTiO_3$ interfaces, for samples grown by atomic layer deposition (ALD) and molecular beam epitaxy (MBE). As described elsewhere,[55, 57] these two techniques span a large growth window for deposition of crystalline γ-Al_2O_3 onto $SrTiO_3$ (001) substrates. The MBE samples were grown in the temperature range of 400-800 °C,[55] while the ALD samples were grown in the range of 200-345°C.[57] Electrical characterization showed that a 6-nm-thick sample grown by MBE at 700 °C had a carrier density of $\sim 8 \times 10^{13}\text{cm}^{-2}$ and electron mobility of $22\text{cm}^{-2}\text{V}^{-1}\text{s}^{-1}$ at room temperature[55] and corresponding values of $3 \times 10^{13}\text{cm}^{-2}$ and $560\text{cm}^2\text{V}^{-1}\text{s}^{-1}$ at 15 K, while a 2.1-nm-thick sample grown by ALD at 345°C had a carrier density of $\sim 6 \times 10^{13}\text{cm}^{-2}$ and an electron mobility of $4\text{cm}^2\text{V}^{-1}\text{s}^{-1}$ at room temperature, and corresponding values of $\sim 5 \times 10^{12}\text{cm}-2$ and $3000\text{cm}^2\text{V}^{-1}\text{s}-1$ at 15 K.[57] Post-deposition annealing of these samples under oxygen-rich conditions suppressed the interfacial conductivity and the Ti^{3+} photo-emission signal was no longer visible.

3.1.2 Methods

Cross-sectional samples suitable for electron microscope observation were prepared by mechanical polishing, followed by Ar-ion-milling. The NCSI studies were performed with an FEI Titan 80-300 image-corrected TEM operated at 300 keV with the spherical aberration coefficient fixed at -13 μm and the objective lens defocus set at +6 nm. Under these imaging conditions, the oxygen atomic columns can be seen with high intensity due to enhancement of both the phase contrast and the amplitude contrast.[141, 143] Electron holograms were recorded at 300 keV with the FEI Titan 80-300, using a biprism voltage of $\sim$200 V, corresponding to an interference-fringe spacing of $\sim$0.14 nm. Electron-energy-loss spectroscopy (EELS) and spectrum mapping were carried out using a JEOL ARM 200F operated at 200 kV with dispersion set at 0.25 eV/channel.

3.1.3 Results

Figure 3.1 shows an NCSI image of a 2.1-nm-thick γ-Al_2O_3 layer grown by ALD on a TiO_2-terminated $SrTiO_3$ (001) substrate at 345 °C. This sample had demonstrated enhanced interfacial conductivity, which was attributed to the presence of a quasi-2DEG at the interface.[28] As shown by comparison with the inset structural model, and confirmed by image simulations, the positions of the Sr and O mixed atomic columns in the substrate are identified by the strong bright spots, the O atomic-column positions correspond to the weak bright spots, and the intensities of the Ti atomic columns are in between.

Off-axis electron holography is a TEM-based technique that is well-suited to

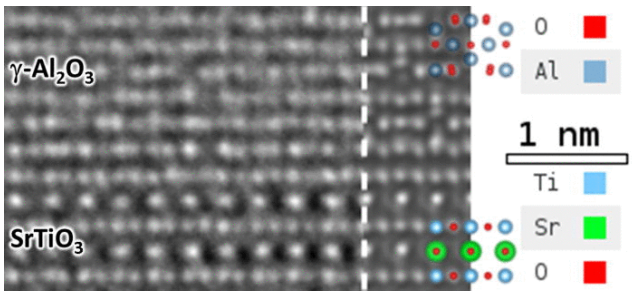

Figure 3.1. NCSI of sample grown by ALD

Left: Aberration-corrected NCSI showing γ-Al_2O_3/$SrTiO_3$ interface for sample grown by ALD at 345 °C, previously shown to have a quasi-2DEG at the interface. $SrTiO_3$ in [110]-type projection. The intensity of spots in γ-Al_2O_3 appears random because of inherent disorder in Al site occupancy. Right: image simulated using Dr. Probe software.[242] Image conditions were: sample tilt 0.3° in x and 0.6° in y directions. Spherical aberration coefficient C_3 = -10 μm, Defocus = +5 nm. Other residual aberrations were ignored. A super-cell with varying local Al tetrahedral site occupancy is used to simulate the structure disorder of γ-Al_2O_3.

quantifying electrostatic and magnetic fields within electron-transparent specimens with nanometer-scale resolution.[258] The technique was previously used to quantify the 2DEG present in a GaN/InAlN/AlN high-electron-mobility transistor device,[188] and the approach was used in the current studies to investigate the quasi-2DEG at the γ-Al_2O_3/$SrTiO_3$ interface. Figure 3.2 shows off-axis electron holography results for the sample shown in Figure 3.1, which was grown by ALD at 345 °C. Figures 3.2(a) and 3.2(b) show reconstructed thickness and phase images, where the former is calibrated in units of inelastic mean free path. Some diffraction contrast is apparent near the edge of the field of view, which could have some effect on the amplitude image profile. The phase profile is less affected. Figures 3.2(c) and 3.2(d) show line profiles from (a) and (b), averaged over the boxes, as shown, to decrease the effects of signal noise. The periodic oscillations, most notably visible in the thickness profile, correspond to unit-cell spacings in the $SrTiO_3$ substrate. The different heights of the amplitude and phase profile shown in red and blue, respectively, on either side of the

interface indicated by the vertical line in Figures 3.2(c) and 3.2(d), can be attributed to differences both in the mean inner potential (MIP) and the inelastic mean-free-path between γ-Al_2O_3 and $SrTiO_3$.

What is significant here is that the amplitude profile on the $SrTiO_3$ side of the interface rises abruptly within a distance of about one unit cell moving away from the interface, whereas the phase profile relatively rises more slowly. Any oxygen vacancies present in this region would have the immediate effect of reducing the mean inner potential. However, a simple calculation based on the atomic number of $SrTiO_3$ ($38 + 22 + 3 \times 8 = 84$) compared with $SrTiO_2$ ($38 + 22 + 2 \times 8 = 76$) suggests that the presence of oxygen vacancies would have a relatively small effect ($\sim$9.5%) on the phase profile compared with the much larger drop ($\sim$25% - 30%) measured experimentally. The additional reduction is consistent with the presence of excess negative charge associated with a quasi-2DEG that is highly confined to within $\sim$1 nm of the interface plane. The situation here is clearly different from the previously mentioned example of the 2DEG occurring in nitride/nitride heterostructures that was induced by polar discontinuity, where the presence of the 2DEG was identifiable from the positive curvature in the phase profile near the interface on the substrate side.[188] Further holography studies of samples with and without the quasi-2DEG are needed to evaluate whether the curvature of the interfacial phase profile can be used to quantify the magnitude of the quasi-2DEG.

Energy-loss near-edge fine structure contains rich information about the local density of states.[259] The technique can be used to determine the oxidation state of Ti atoms within the $SrTiO_3$ layer. Figure 3.3(a) shows spectra averaged along the interface direction, summarizing the results of the EELS analysis. These spectra were collected over an energy range between about 250 eV and 762 eV. The Ti-L edge

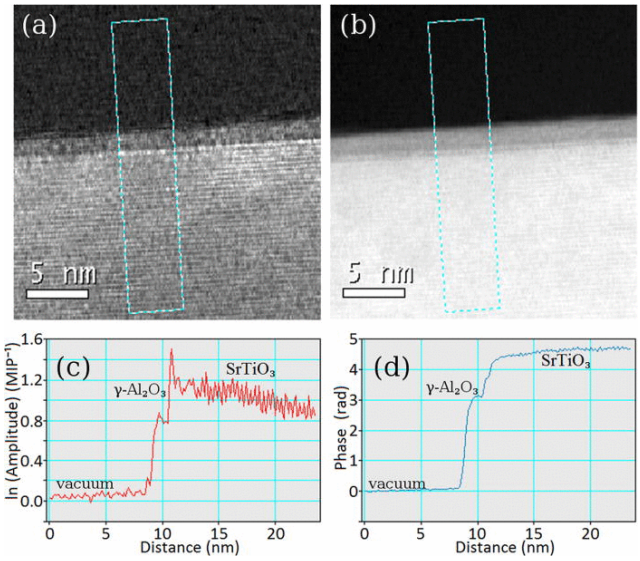

Figure 3.2. Electron holography of sample grown by ALD

Off-axis electron holography of the same γ-Al_2O_3/$SrTiO_3$ sample shown in Figure 3.1: (a) Thickness image reconstructed from the hologram, in units of mean free path; (b) Reconstructed phase image. (c) and (d) Line profiles from (a) and (b), averaged horizontally. Interface position indicated. Note abrupt rise in phase profile over a distance of $\sim$1 nm within the γ-Al_2O_3, which is unlike the behavior of the amplitude profile, which shows an abrupt increase.

and O-K edge were then investigated in more detail. For the Ti-L edge, the energy range between 342 eV and 450 eV was used to remove the background via power-law fitting.[259] In spectra taken from within one unit cell ($<$0.5 nm) of the interface, the Ti-L edge shows mostly two peaks, whereas spectra taken at locations away from the interface clearly show four peaks. This difference in peak shapes is direct evidence for substantial reduction in the Ti oxidation state at the interface from Ti^{4+} to Ti^{3+}.[156]

Two-dimensional spectrum mapping across the γ-Al_2O_3/$SrTiO_3$ interface was also carried out. Figure 3.4(a) is a HAADF image from the same sample already shown in Figure 3.1, indicating the area used for mapping purposes. Multiple linear least-square (MLLS) fitting was performed on the extracted ELNES spectrum map between 455 eV

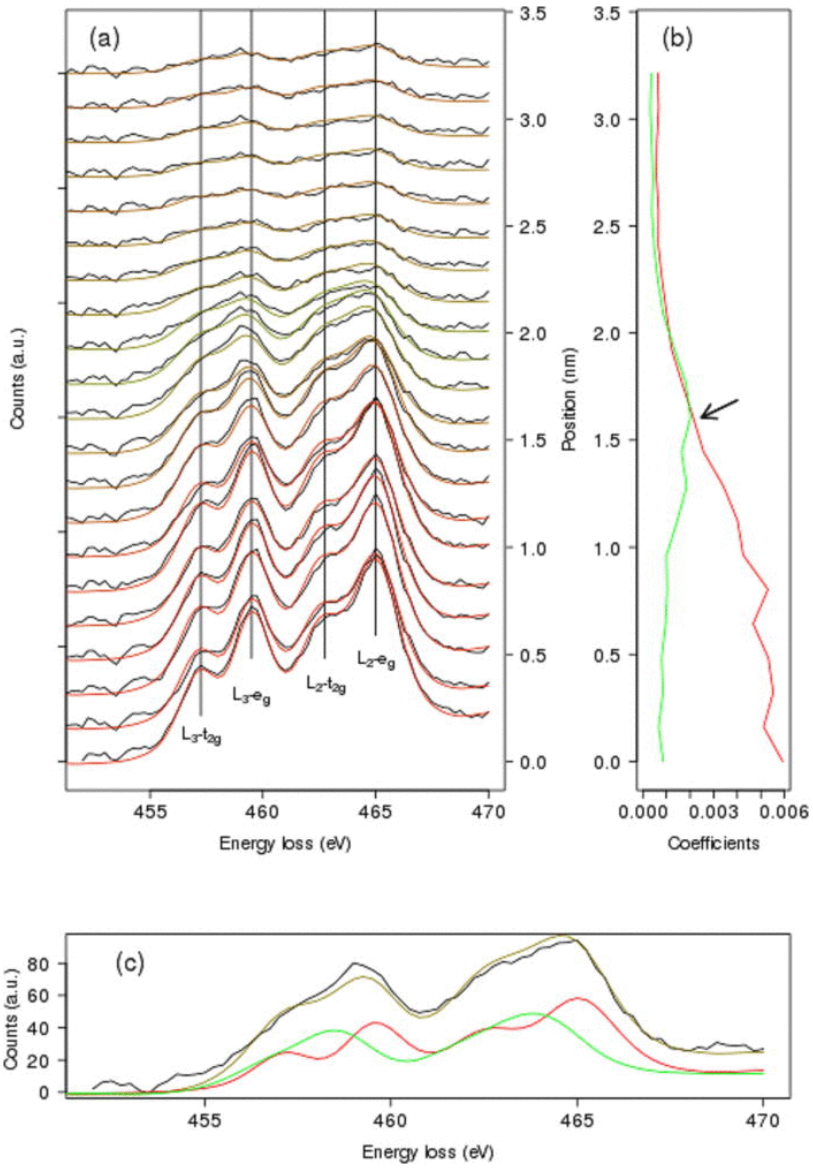

Figure 3.3. Ti-L edge near the γ-Al_2O_3/$SrTiO_3$ interface.

ELNES spectra taken from near the γ-Al_2O_3/$SrTiO_3$ interface on the $SrTiO_3$ side showing variation of the Ti-L edge as the distance from the interface increases: (a) Line-averaged spectra over the box indicated in Figure 3.4(b). Black lines are experimental spectra and color lines are fitted data. Vertical lines show positions of eg peak and t_{2g} peak in L_2 and L_3 edges in the bulk. (b) Corresponding fitting coefficient of $SrTiO_3$ (Ti^{3+}-rich) in green and $SrTiO_3$ (Ti^{4+}) in red. (c) Spectra acquired at the location indicated by the arrow in Figure 3.4(b) where Ti^{3+} has the maximum concentration. Black line is the experimental spectrum, the mixed color line is the fitted spectrum, the red line is the component of $SrTiO_3$ (Ti^{3+}-rich), and the green line is the component of $SrTiO_3$ (Ti^{4+}).

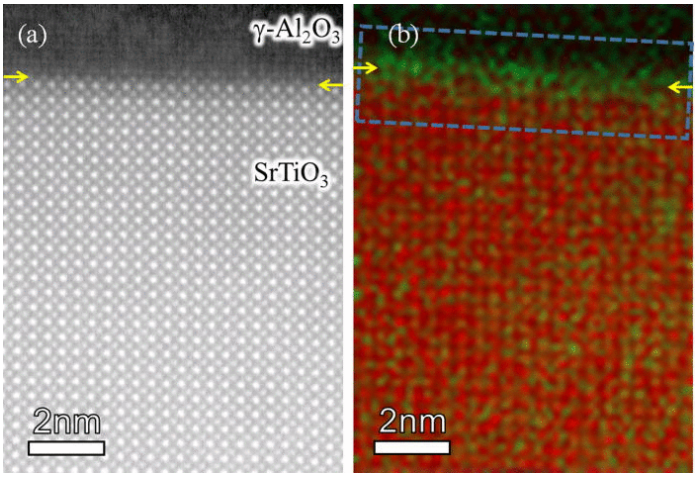

Figure 3.4. HAADF image and 2D map on Ti-L edge at γ-Al_2O_3/$SrTiO_3$ interface. (a) HAADF STEM image of γ-Al_2O_3/$SrTiO_3$ interface showing region where the EELS spectra were later collected. Gamma value adjusted in order to show both $SrTiO_3$ and γ-Al_2O_3. Interface indicated by arrows; (b) False color map showing distribution of Ti^{3+} and Ti^{4+}. Green is fitting coefficient of the Ti-L edge in $SrTiO_3$ (Ti^{3+}-rich), and red is fitting coefficient of the Ti-L edge in $SrTiO_3$ (Ti^{4+}). Box indicates area used for line-averaged spectra shown in Figure 3.3.

and 467 eV using spectra for $SrTiO_3$ and $SrTiO_{2.75}$ taken from Ref. [156]. Because the instrumental operating conditions in these experiments were different from those used previously, a numerical average (low-pass) filter, scaling and shifting were applied to the reference spectra such that the $SrTiO_3$ reference spectrum had closest agreement (minimum difference) with the spectrum in the bulk $SrTiO_3$. Figure 3.3(b) shows the results of applying the MLLS fitting using the Ti-L edges in Figure 3.3(a). Figure 3.4(b) shows the same fitting over the entire 2-D area. Clearly, reduced Ti species are segregated at the interface and highly confined to within about two unit cells. The fine structure of the O-K edge can also show some differences that reflect local oxygen ordering and/or oxidation state, as demonstrated in Ref. [156].

Figures 3.5(a) and 3.5(b) show line profiles of the different atomic species as a function of position. All of the fitting coefficients are on the same scale except that

the Ti-L edges and the O-K edge are on different scales. The reference spectrum for γ-Al_2O_3 was taken from previously published results,[260, 261] and has been scaled to the same count values here by assuming that the cross-section of the O-K edge in $SrTiO_3$ is the same as in γ-Al_2O_3. In Figure 3.5(b), the thin black line is the sum over all fitting coefficients for the O-K edge of $SrTiO_x$ and γ-Al_2O_3. This line decreases gradually due to the wedge shape of the specimen. The interface position is located at around 10-11 nm along the horizontal axis. No abrupt change in the total O-K edge signal can be identified at the interface, thus indicating that the specimen does not have an abrupt change in thickness across the interface. At the interface, the fitting for the Ti-L edge of $SrTiO_{2.75}$ clearly shows a peak, with a FWHM of 1.0 nm. The fitting for the O-K edge of $SrTiO_{2.75}$ also shows a peak, although it is much noisier due to the lower overall signal count, and the difference in fine structure is less obvious. The reduced χ^2 statistic for the O-K edge to indicate the goodness of the fit is shown in Figure 3.5(c). These two peaks directly show that the reduction in oxidation state of Ti occurs right at the interface and must be highly confined to a distance of no more than 2 unit cells. This result is consistent with the electron holography analysis of the same sample, which also showed that the phase change happened over similar specimen dimensions. ELNES spectrum mapping and MLLS fitting has also been applied to an MBE-grown sample, and the results (not shown here) again confirmed the presence of a reduced Ti oxidation state in the region immediately adjacent to the γ-Al_2O_3/$SrTiO_3$ interface.

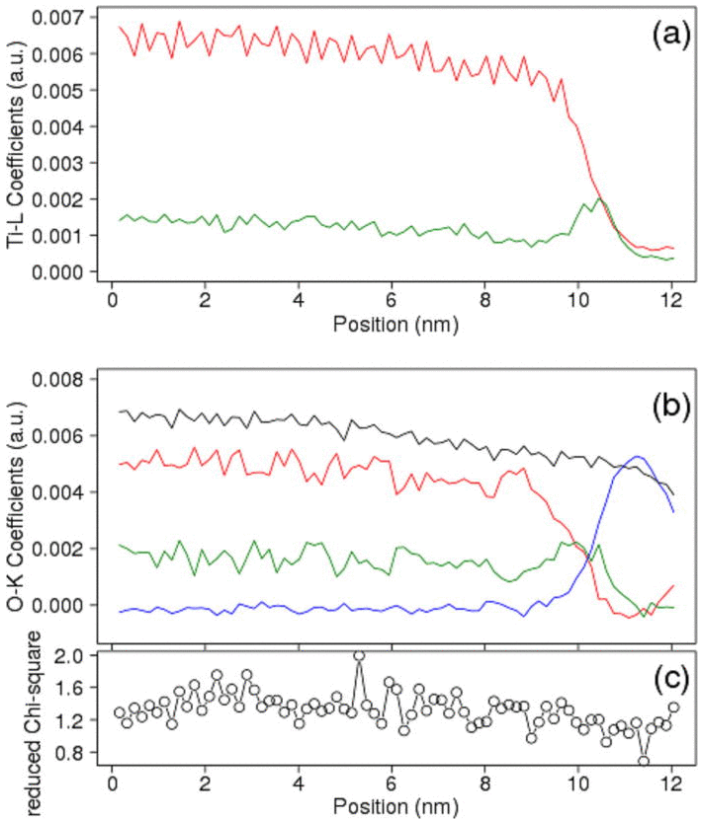

Figure 3.5. O-K edge near the γ-Al_2O_3/$SrTiO_3$ interface

Line profile of the ELNES MLLS fitting coefficients using the same color as the false color map in arbitrary units. (a) Ti-L edge and (b) O-K edge. Red lines are fitting coefficients of $SrTiO_3$, green lines are fitting coefficients of $SrTiO_{2.75}$, green line is the fitting coefficients of γ-Al_2O_3, black line in (b) is the sum of the three colored lines. The line of dots below (b) shows the reduced χ^2 statistic for the O-K edge as a measure of goodness of fit ($\chi^2 = 1$ is a good fit). Underfitting ($\chi^2 > 1$) is probably related to the plural scattering.

3.1.4 Summary

These electron holography studies of the γ-$Al_2O_3/SrTiO_3$ interface suggested the presence of a quasi-2DEG that was closely confined to the $SrTiO_x$ side of the interfacial region. This result differs from previous holography studies of the AlN/GaN system, where the observed 2DEG had been introduced by polar discontinuity.[188] Moreover, the EELS results provided direct evidence for a reduction in the overall oxidation state at the interfacial layer. Further studies of samples grown by MBE and ALD at different temperatures are still needed, in particular to facilitate quantitative comparisons between the quasi-2DEG measured by electron holography with the Ti^{3+} concentrations measured by ELNES, and with electrical measurements.

3.2 ELNES Hyperspectral Unmixing

The MLLS fitting method was used for the EELS analysis in chapter 3.1. However, this approach has several drawbacks:

1. Reference spectra are always required. However, the interfacial region may actually have an unknown spectral component.

2. Reference spectra found in the literature are likely to have been acquired under operating conditions that are quite different from those used in this research, including differences in beam energy spread, acceleration voltage, convergence angle, collection angle, and sample thickness. These differences will cause differences in energy resolution, monopole or quadrupole transitions, anisotropic effects, electron channeling, plural scattering, and etc. The resulting spectral shape is also likely to be slightly different. These differences may cause large errors in MLLS fitting, especially

considering that the differences in the different spectral components (such as Ti^{4+} and Ti^{3+}) are not large.

Unsupervised hyperspectral unmixing methods, which do not require any external reference spectra, have been developed as part of this dissertation research. This approach allows these problems and difficulties to be avoided.

3.2.1 Comparison between samples with and without 2DEG

Table 3.1. Information of samples with and without 2DEG

Temperature	Substrate Termination	P_{O_2}	Thickness	Post-deposit anneal
700°C	Mixed TiO_2/SrO	10^-6 Torr	2 nm	No
600°C	Crystec TiO_2	10^-6 Torr	3 nm	400 °C in air for 1hr

Ti-L edge

The sample used in this comparison are listed in Table 3.1. The results shown in Figures 3.6(a)-(d) are taken from a 2-nm γ-Al_2O_3 film on $SrTiO_3$ sample grown by MBE at 700°C under the oxygen partial pressure of 1×10^{-6} Torr. In Figure 3.6(a), the green spectrum with 2 peaks instead of 4 peaks shows the partially reduced Ti^{3+}-rich $SrTiO_3$, which appears at the interface, as shown in Figures 3.6(b) and (c). Figures 3.6(e)-(h) are from a 3-nm γ-Al_2O_3/$SrTiO_3$ sample grown by MBE at 600°C under the oxygen partial pressure of 1×10^{-6} Torr. The red and green spectra in Figure 3.6(e) show little difference, indicating that the Ti^{3+} has been re-oxidized during the annealing process. In both samples, some Ti has diffused from the $SrTiO_3$

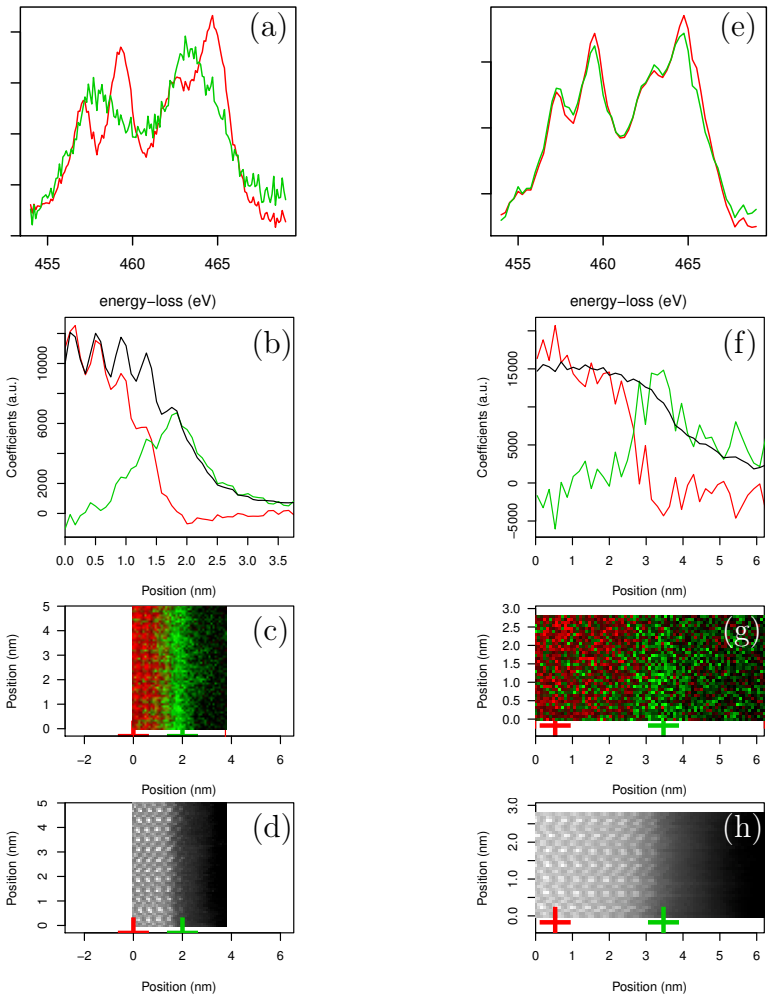

Figure 3.6. Comparison of Ti-L edge between samples with 2DEG and without 2DEG

(a)-(d) are from a sample with 2DEG grown by MBE. (e)-(h) are from an annealed sample without 2DEG. (a)(e) are spectral signatures. (b)(f) are the profiles of fitting coefficients (the abundance) averaged along the in-plane direction and the black lines in each profile is the sum of the color lines. (c)(g) are 2D maps of the fitting coefficients. (d)(h) are HAADF images acquired simultaneously with the spectral map.

substrate into the γ-Al_2O_3 film. From the spectra, it is apparent that Ti in the film has similar oxidation state as at the interface.

O-K edge

Because of the de-localized nature of the ELNES signal, as discussed in Chapter

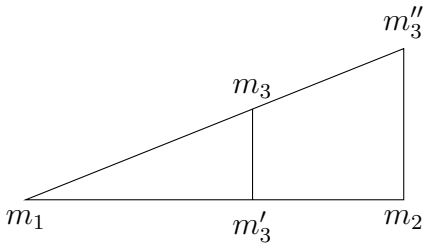

Figure 3.7. Geometry for removing film signal from the interfacial signal.
m_1 m_2 and m_3 are three extracted endmember signatures. m_1 is in the film, m_2 is in the substrate, m_3 is at the interface. The estimated "pure" interfacial spectral siguature is m_3''

2.3.1, the interfacial signal will always be mixed with signal from the film. For the O-K edge, the signal from the film will not be zero because the film is also an oxide. Although the unmixing algorithms can still detect the three different spectral signatures, the interfacial signature does not represent a "pure" interfacial component, i.e., a "pure" interfacial component does not exist in the dataset. The following geometry is used to estimate the "pure" interfacial component by assuming the spectrum at the interface is orthogonal to the bulk. As illustrated in Figure 3.7, m_1 represents signal from the film. m_2 is for the substrate, m_3 is at the interface. Assuming that the line m_1-m_2 is orthogonal to line m_2-m_3'', then the estimated "pure" interfacial spectral siguature is m_3''

Figure 3.8 shows a comparison of the O-K edges from the samples already shown in Figure 3.6. In the sample with 2DEG (Figures 3.8(a)-(d)) there is an interfacial component. The spectrum signature of the interfacial component (green) has a significantly higher t_{2g} peak, whereas only two endmember signatures were detected in the sample without 2DEG (annealed sample) . Figure 3.9 shows a comparison between the error analysis using 3 endmembers (a) and 2 endmembers (b) for the

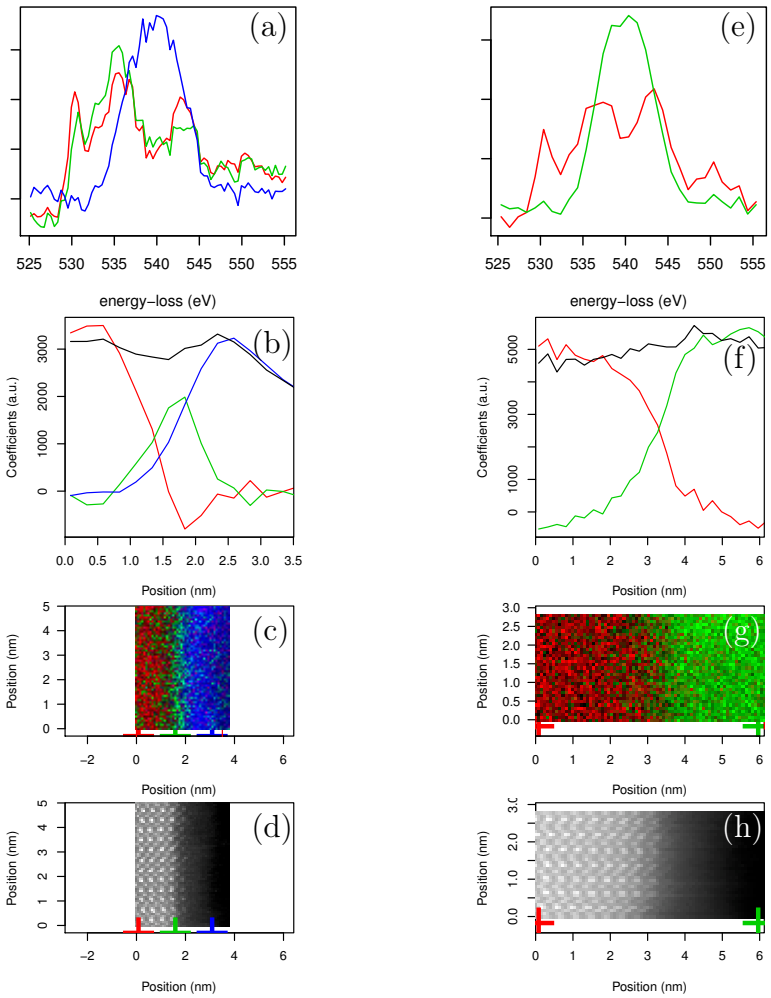

Figure 3.8. Comparison of O-K edge between samples with and without 2DEG

(a)-(d) are from sample with 2DEG grown by MBE. (e)-(h) are from annealed sample without 2DEG. (a)(e) are spectral signatures. (b)(f) are line profiles of fitting coefficients (the abundance) averaged along the in-plane direction and the black lines in each profile is the sum of the color lines. (c)(g) are 2D maps of the fitting coefficients. (d)(h) are HAADF images acquired simultaneously with the spectral map.

annealed sample. The residual at the interface in (b) is clearly abnormal in both χ^2 statistic and residual plot.

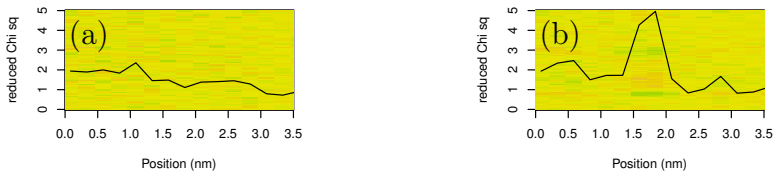

Figure 3.9. Comparison of error analysis using 2 or 3 endmembers for the sample with 2DEG

(a) Error analysis using 3 endmembers. The black line is the χ^2 statistic. The color map is the residual. (b) Error analysis using 2 endmembers. At the interface ($x \sim$ 1.5-2 nm), χ^2 significantly deviates from 1 and there is some pattern in the residual map.

3.2.2 Comparison between sample grown by MBE at high temperature and by ALD at low temperature

Table 3.2. Information of samples grown by MBE and ALD

Temperature	Substrate Termination	Thickness	Resistance (2pt)
700°C	Mixed TiO_2/SrO	2 nm	∼900kΩ
345°C	Crystec TiO_2	2.1 nm	∼20kΩ

O-K edge

The sample used in this comparison are listed in Table 3.2. Differences in the O-K edge interfacial signatures show up in comparisons between the MBE sample grown at 700°C and the ALD sample grown at 600°C. The interfacial component in the MBE sample (green line in Figure 3.10(a)), has smaller A1 (t_2g) peak and smaller C1 O-2p^* peak compared with the ALD sample (Figure 3.10(e)), although both have similar width (∼2nm). This difference indicates higher oxygen vacancy concentration in the MBE sample. The onset energy of the interfacial component in the MBE sample is also slightly higher than in the bulk. This difference does not

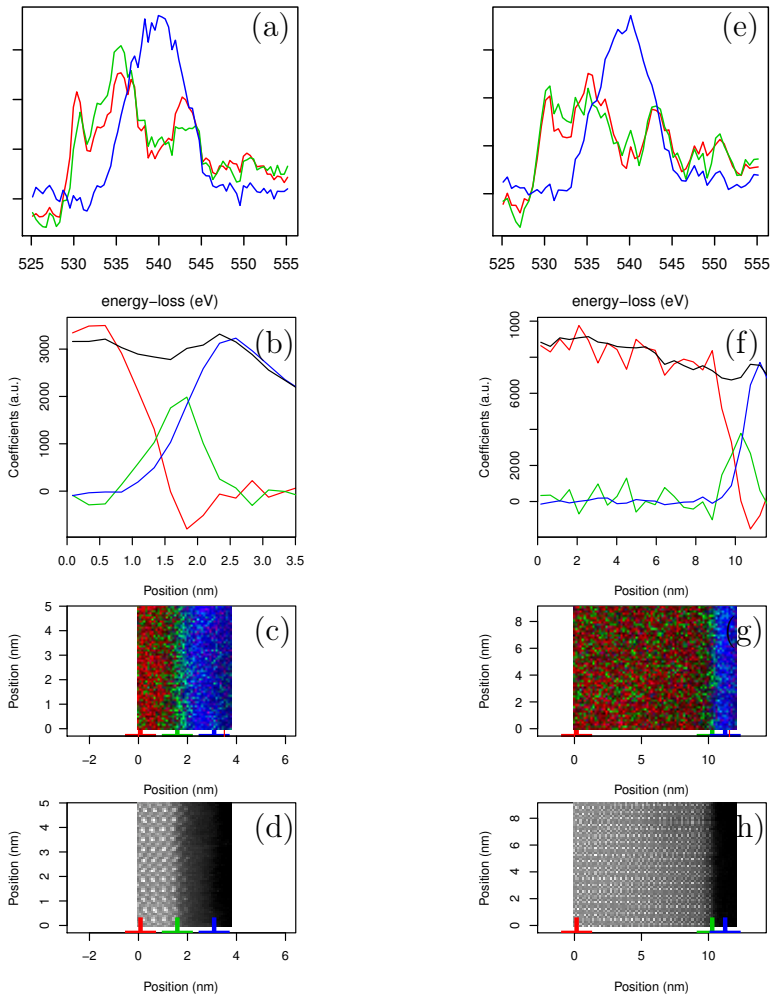

Figure 3.10. Comparison of O-K edge between sample with 2DEG and without 2DEG (a)-(d) are from a sample with 2DEG grown by MBE at 700°C. (e)-(h) are from a sample with 2DEG grown by ALD at 345°C.

appear in the ALD sample. The higher onset energy is indirect evidence for higher 2DEG concentration in the MBE sample. The relationship between the Fermi level and the electrical properties of the 2DEG is further discussed in Chapter 3.6.

3.3 Electrical Measurements

A 4-wire electrical transport measurement using less than 1 lA current at a frequency of 7 or 13 Hz. was made by our collaborators at Case Western Reserve University are summarized in Figure 3.11. Details of the measurement can be found in Ref.[55, 57]. The temperature dependence of resistance and mobility are fitted using the variable range hopping (VRH) model, the electron-electron scattering model, and the electron-phonon scattering. The temperature dependence of the carrier density are fitted using the Arrhenius relationship.

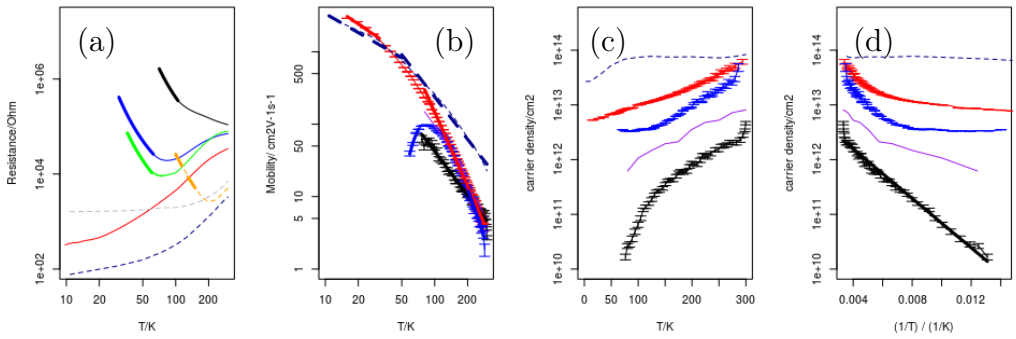

Figure 3.11. Temperature dependence of the Hall mobility and carrier density. Black: ALD sample with 1.3nm γ-Al_2O_3 film grown at 345°C. Red: ALD sample with 2.1nm γ-Al_2O_3 film at 345°C. Blue: ALD sample with 4.3nm γ-Al_2O_3 film at 345°C. Green: ALD sample with 8.5nm γ-Al_2O_3 film at 345°C. Gray: MBE sample with 4nm γ-Al_2O_3 film grown at 400°C. Dark blue: MBE sample with 6nm γ-Al_2O_3 film grown at 700°C. Orange: MBE sample with 6nm γ-Al_2O_3 film grown at 700°C with post-annealing in oxygen. (a) Resistance (b) Mobility (c)(d) Carrier density. Thick lines are fitted curves. Error bars are added when available. This figure uses the same data as in Ref.[57] and Ref.[55], but reproduced with a different axis.

As shown in Figure 3.11(a), in all samples with a negative sheet resistance - temperature relationship at low temperature, the temperature dependence of sheet

resistance can be modeled very well using the VRH model.[262]

$$R_S \propto exp[(T_0/T)^{\nu}] \tag{3.1}$$

In the case of a flat density of states (DOS) near the Fermi energy, the resistance obeys Mott's VRH law with $\nu = 1/(d+1)$, d is the dimension of the system.[263] $\nu = 1$ if there is a simple gap in the DOS and $v = 1/2$ if there is a Coulomb gap.[264]. In Figure 3.11(a), The fitted value of ν for the black, green, blue and orange line are 1.04, 1.27, 0.93, 0.50, respectively. The variation could be due to measurement errors or resistance sources other than VRH.

Figure 3.11(b) shows the temperature dependence of electron mobility. The electron mobility in the low conductive ALD sample (1.3nm γ-Al_2O_3 film), shows $T^{-2.01}$ relationship within the measurable range (76-300K), which is very close to the T^{-2} dependence of electron-electron scattering.[265] The T^2 dependence of resistance has been previously observed in n-doped $SrTiO_3$,[125] although details of the process were not fully understood.[124, 126–128, 266] This behavior differs from conventional semiconductors such as silicon, in which the low temperature mobility is limited by ionized impurity scattering with a temperature dependence of $T^{3/2}$,[267] although impurities may still play an important role in the electron-electron scattering in $SrTiO_3$ by affecting the relaxation rate.[266]

Temperature dependence of electron mobility in other samples ranges from T^{-1} for the high conductive ALD (red line) and MBE (dark blue line) samples at low temperature to $T^{-4.4}$ for the high conductive ALD sample (red line) near room temperature. The T^{-5} dependence could originate from electron-phonon scattering.[268, 269] However, the T^{-1} dependence at low temperature needs further investigation.

The temperature dependence of electron density can be analyzed using classical

theory for a doped semiconductor. At low temperature,

$$n = \sqrt{\frac{N_C N_D}{2}} e^{-\frac{E_C - E_D}{2k_B T}} \ (N_A = 0, n << N_D) \tag{3.2}$$

or

$$n = \frac{N_C(N_D - N_A)}{2N_A} e^{-\frac{E_C - E_D}{k_B T}} \ (N_A > 0, n << N_D, N_A) \tag{3.3}$$

At intermediate temperature,

$$n \approx N_D \tag{3.4}$$

At high temperature,

$$n \approx n_i > N_D \tag{3.5}$$

$$n_i = \sqrt{N_C N_V} e^{-\frac{E_G}{2k_B T}} \tag{3.6}$$

where n is the electron density, N_C is the density of states in the conduction band, N_D is the donor concentration, N_A is the acceptor conecntration, E_C is the conduction band energy level, E_D is the donor level, E_A is the acceptor level, E_F is the Fermi energy level, K_B is the Boltzmann constant, and T is temperature. By plotting $log\, n$ vs $1/T$, $E_C - E_D$ or E_G can be derived from the slope.[270, 271]

In Figure 3.11(d), the calculated E_G from the low conductive ALD sample (the black line) is about 1-2eV near room temperature, which is smaller than the experimental value (3.2eV). However, considering that only a number of data points are used for the fitting, this deviation is within an acceptable range. Below room temperature, the low conductive ALD sample shows a good linear relationship. The calculated $E_C - E_D$ from the Arrhenius plot in Figure 3.11 is 87meV if the acceptor concentration N_A is not zero. In DFT simulations described in Chapter 3.6, it is shown that this value matches the calculated subband gap near the interface. For samples with higher

carrier density, the carrier density varies very slowly with temperature, indicating that the donors are fully ionized ($n = N_D$) or in a degenerate state ($E_C - E_F < 3k_BT$). Considering that the carrier density does not decrease even at temperatures as low as 15K, the latter explanation seems more plausible.

3.4 Electron Holography

Further off-axis electron holography observations were performed on the FEI Titan microscope operated at 300kV in imaging mode. C_S and defocus were set close to zero to optimize information transfer.[137] The sample was tilted along the film-growth direction in order to avoid strong Bragg diffraction. Two MBE samples with 6nm γ-Al_2O_3 grown at 700°C were used in these observations. One was as-deposited, the other had been annealed in oxygen at 500°C for 1 hour. Electrical potential simulations were carried out using methods described in Chapter 2.6.3.

Holography results showed no significant difference in phase profiles between the samples with or without the 2DEG, which is consistent with the DFT calculations. Also, there was no significant differences in the slope of the potential in the γ-Al_2O_3 film between the as-deposited sample and the annealed sample, indicating there was no significant potential gradient difference between the sample with and without 2DEG. Electron holography observations of the potential gradient caused by polar discontinuity has been previously reported[272] The electric field across $LaAlO_3$ in $LaAlO_3/SrTiO_3$ system is reported as large as 0.8V/nm.[61] However, the potential gradient difference was not seen in this experiment. By combining this experimental result with results of DFT simulations, where the system with 2DEG did not show

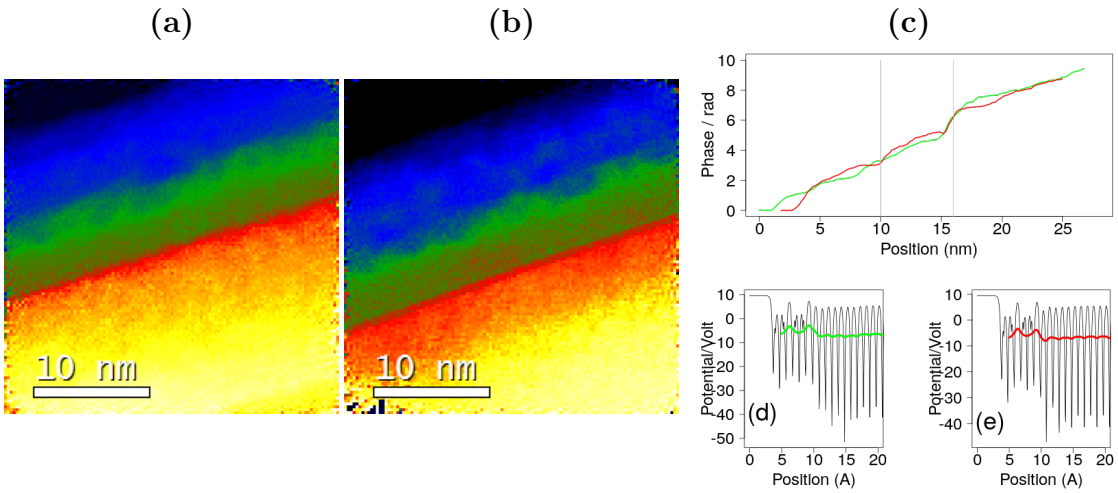

Figure 3.12. Experimental and simulated phase map from electron holography

Holography phase image of (a) sample with 2DEG and (b) sample without 2DEG. Both films are 6nm thick. (c) Phase profile across the interface (Right side is the substrate). Green is the sample with 2DEG. Red is the sample without. (d)(e) Potential profile calculated by DFT for the model with 2DEG (d) and without 2DEG (e). Thick lines are smoothed.

any electric field in the γ-Al_2O_3 film, it is concluded that the polar discontinuity mechanism[58] does not explain formation of the 2DEG in the γ-Al_2O_3/$SrTiO_3$ system.

3.5 Spectrum Simulation

Multiplet simulations using multiX were carried out, using the method described in Chapter 2.6.2. Two structural models were relaxed using DFT, one with oxygen vacancies at the interface and the other without. More details of the structural models are provided later in Chapter 3.6. The Ti atoms in the TiO_2 layer at the interface is chosen as the core atom. The DFT-relaxed structural models were then fed into the multiplet simulation program. Empirical parameters, including the scalars of the Coulomb potential, the crystal field and the spin-orbital coupling were acquired from

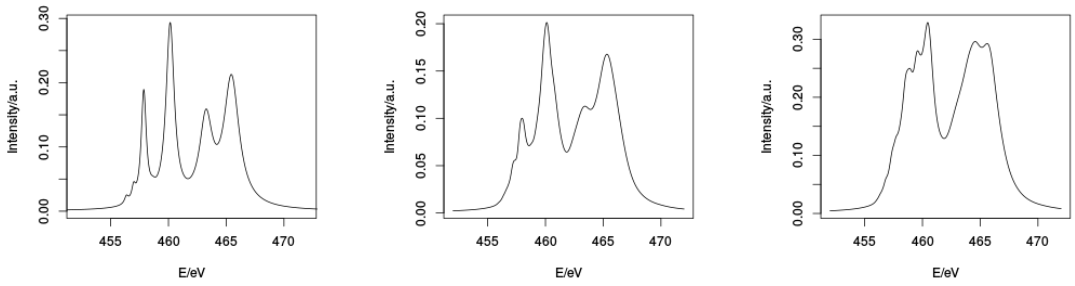

(a) (b) (c)

Figure 3.13. Two structural models (with and without oxygen vacancies) relaxed by DFT were fed into multiplets simulation for the Ti-L edge.

(a) Ti^{4+} in $SrTiO_3$ bulk. (b) Ti^{4+} at the interface without oxygen vacancies, showing the effect of geometrical distortion on ELNES. (c) $Ti^{3.5+}$ at the interface with oxygen vacancies, showing the effect of oxidation state on ELNES.

Ref.[246] in order to match experimental values in the bulk $SrTiO_3$. The result for $Ti^{3.5+}$ was an average of Ti^{4+} and Ti^{3+}.

The results in Figure 3.13 show that both the lattice relaxation near the interface (Figure 3.13(b)) and the oxygen vacancies near the interface (Figure 3.13(c)) smear out the 4 peaks of the Ti-L edge. However, a change in oxidation state has a much greater influence than lattice relaxation. At the oxidation state of $Ti^{3.5+}$, the Ti-L edge shows two major peaks (Figure 3.13(c)), which also matches the experimental result in Ref.[156]. However, 4 peaks remain for Ti^{4+} without oxygen vacancies even when lattice relaxation is taken into consideration (Figure 3.13(b)), although the peaks are slightly broader than in the bulk (Figure 3.13(a)).

By comparing the simulated results in Figure 3.13 with the experimental spectra in Figure 3.6, it can be concluded that the green spectrum in Figure 3.6(a) is introduced by oxygen vacancies, and the green spectrum in Figure 3.6(e) is introduced by lattice relaxation near the interface rather than by oxygen vacancies.

For the O-K edge, since the electron dipole transition is dominant under our experimental conditions using 200keV electrons, in which the convergence semi-angle is 20 mrad and collection semi-angle is 22 mrad, the dipole selection rule $\Delta L = \pm 1$ limits the transition to be O-1s to O-2p.[273] The core state O-1s has a very sharp density of state. Therefore, the projected density of state of the O-2p orbital should be close to the joint density states, which in turn is proportional to the experimentally observed O-K edge.[194]

The DFT-calculated projected O-2p density of state in bulk $SrTiO_3$ (the black line in Figure 3.14) has four major peaks, which is consistent with experimental O-K ELNES (the red lines in Figure 3.8 and Figure 3.10). Meanwhile, the spectral features for the oxygen atoms near the interface, such as decrease of amplitude in the A1 (t_{2g}) peak, and the smearing of the peaks, are visible in both simulated projected density of states (color lines in Figure 3.14) and the experimental spectra (green lines in Figure 3.8). The Fermi level (0eV in Figure 3.14) is just above the bottom of the A1 peak, running through the t_{2g} states in the SrO layer. The bottom of the A1 peak in the second layer (SrO) layer is lower than in the first layer (Al-Ti mixed layer), while there is an extra peak below the Fermi level in the first layer existing only in the spin-up DOS. Because this peak is filled, it cannot be seen in the O-K ELNES. However, the gap above the sub-band peak is about 90meV, which matches the measured $E_C - E_D$ value in the Hall measurement described in the previous section.

3.6 DFT Simulations

Slab models described in Chapter 2.5.4 were build for DFT calculations. The models are set to be centrosymmetric in order to avoid polarization divergence. Charge

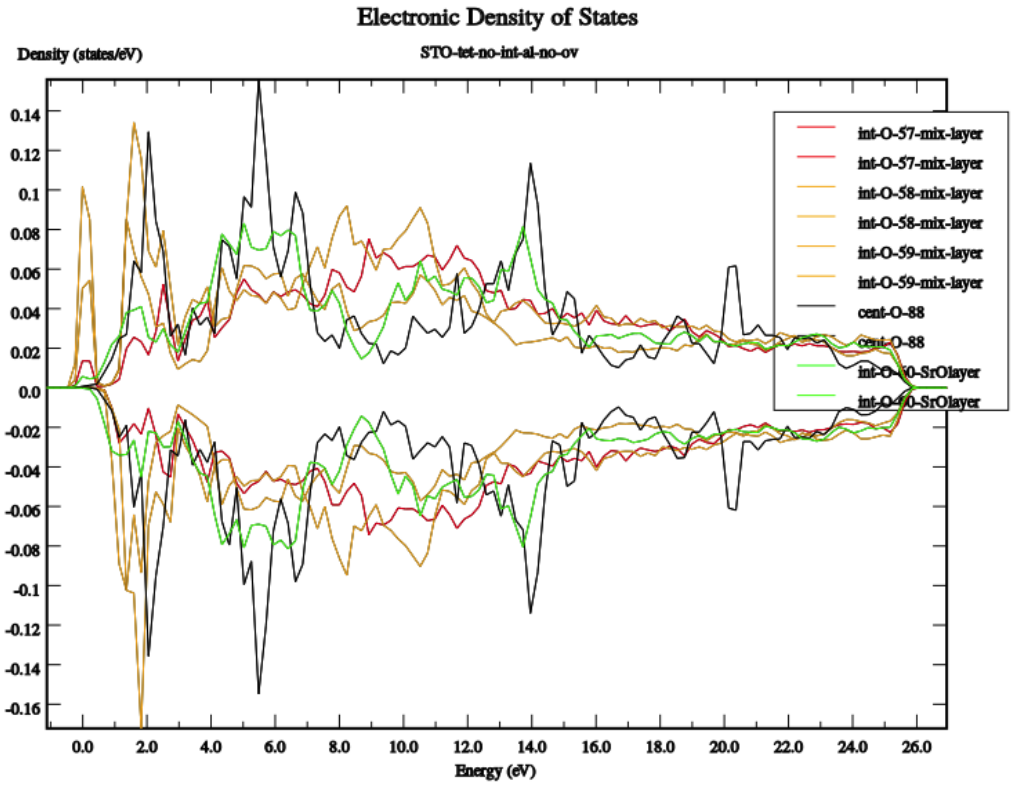

Figure 3.14. LDA+U calculation (with U=5 eV) of projected density of state of oxygen atoms at different positions

Spin-polarized projected density of state using LDA+U for a model with oxygen vacancies at the interface and one layer of Ti-Al intermixing at the interface. Black: bulk O atom. Red, orange and yellow: three oxygen atoms at the interfacial TiO_2 layer occupying different positions. Green: oxygen atom in the SrO layer below the interfacial TiO_2 layer.

neutrality is ensured by making slight changes to the γ-Al_2O_3 layers. Because both the γ-Al_2O_3 crystal structure and the positions of oxygen vacancies can be random, many structural models were built and relaxed with DFT. The starting point of the models is shown in Figure 3.15. Modifications of each model are listed in Table 3.3. The structures with relative lower energy were further processed for LDOS, spectrum and image simulations. In order to balance between the number of structures and our calculation capability, a $\sqrt{2} \times \sqrt{2}$ cell with 10 uc $SrTiO_3$ slab are used in all calculations. The k point density was set to be $4 \times 4 \times 1$.

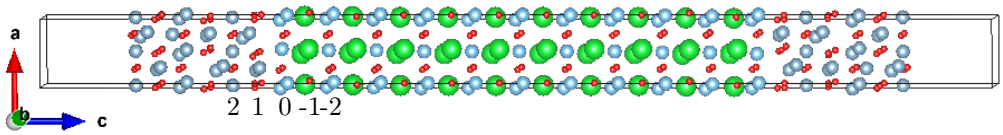

Figure 3.15. Atomic model for the DFT relaxation

Atomic model of γ-Al_2O_3/$SrTiO_3$ interface. Red is O, green is Sr, light blue is Ti, dark blue is Al. Atomic layers are labeled using numbers.

DFT calculations showed that the models with Al atoms at the tetrahedral center between the interfacial TiO_2 layer and the γ-Al_2O_3 layer[274] were not stable. However, the structure with Ti-Al intermixing at the interfacial layer stabilized the oxygen vacancy at the interface.

A gap above the interfacial sub-band and the conduction band minimum (CBM) showed up at the interface in the DFT calculation. This gap is indirectly confirmed in the temperature dependence of the carrier density measured by the Hall effect. The DFT calculation also showed that the Fermi level is running through this gap at the interfacial TiO_2 layer. Therefore, the interfacial TiO_2 layer is not participating in transport at low temperature. DFT calculations show that the Fermi level was above the CBM in the layer below the interfacial TiO_2 layer. Therefore, the high mobility

Table 3.3. Models used in DFT relaxation

#	Atom(s) between layer 0 and 1	layer contain oxygen vacancy	layer with intermixing	free e^- per supercell
A	Al	No	No	0
B	Al	layer 0 at $(1/4, 1/4)$	No	4
C	Al	layer 0 at $3/4, 3/4)$	No	4
D	TiO_2	No	No	0
E	TiO_2	TiO_2 between layer 0 and 1	No	2
F	No	No	No	0
G	No	No	layer 0 at $(0, 0)$	0
H	No	No	layer 0 at $(1/2, 1/2)$	0
I	No	layer 0 at $(1/4, 1/4)$	No	4
J	No	layer 0 at $(3/4, 3/4)$	No	4
K	No	layer 0 at $(3/4, 3/4)$	layer 0 at $(0, 0)$	2
L	No	layer 0 at $(3/4, 3/4)$	layer 0 at $(1/2, 1/2)$	2
M	No	layer -1 at $(0, 0)$	layer 0 at $(0, 0)$	2
N	No	layer -1 at $(1/2, 1/2)$	layer 0 at $(0, 0)$	2
O	No	layer -1 at $(0, 0)$	layer 0 at $(0, 0)$ layer 2 at $(1/2, 1/2)$	2

electrons are actually located below the interfacial layer on the $SrTiO_3$ side. Because the concentration of the oxygen vacancies near the interface in the MBE sample is higher than in the ALD sample, the Fermi level is also higher in the MBE sample, which explains the higher onset energy of the O-K edge at the interface in Figure 3.10(a). More Ti atoms out-diffused into the γ-Al_2O_3 as the film became thicker. DFT calculations showed that the potential at the Ti in the γ-Al_2O_3 film was lower than in the $SrTiO_3$ bulk. Therefore, as the γ-Al_2O_3 film became thicker, the diffused Ti started to deplete the 2DEG, causing a drop in the electron carrier density. On the other hand, for very thin ALD samples, the interface can be "instantly" oxidized once the sample is exposed to air,[76] which would also deplete the 2DEG. Because both thin and thick γ-Al_2O_3 films may deplete the 2DEG, the critical thickness can be explained. At higher temperature, electrons in the sub-band will be thermally excited

into the conduction band, giving the large $10^{13} - 10^{14}\text{cm}^{-2}$ carrier density observed at room temperature.

3.7 Conclusions

This chapter reports a comprehensive investigation of the γ-$Al_2O_3/SrTiO_3$ interface, in particular the high density sheet charge observed in epitaxial films subject to different growth and annealing conditions. The principal observations can be summarized as follows:

1. ELNES hyperspectral unmixing analyses show that there are detectable oxygen vacancies in the sample with the 2DEG whereas none were seen in sample without 2DEG. Thus, oxygen vacancies must be the key to the 2DEG. Electron holography results show no significant potential gradient difference between samples with and without 2DEG. Thus, polar discontinuity is not necessary for the 2DEG in the γ-$Al_2O_3/SrTiO_3$ system. These results are consistent with DFT calculations, as well as spectrum and Coulomb potential simulations.

2. DFT modeling shows that the interfacial Al is not stable, whereas other models with oxygen vacancies and mixed Al atoms occupying different positions have similar energies. Thus, different atomic configurations are likely to coexist at the same time.

3. Intermixing at the interfacial TiO_2 layer can stabilize the oxygen vacancy. Al - Ti interdiffusion causes a drop in the Fermi level that might be responsible for the drop in carrier density for thicker samples and the existence of an optimal γ-Al_2O_3 film thickness.

Chapter 4

$LaTiO_3/SrTiO_3$ INTERFACES

4.1 The $LaTiO_3/SrTiO_3$ interface

The $LaTiO_3/SrTiO_3$ interface displays a 2DEG which has been attributed to charge doping from the Mott insulator $LaTiO_3$ into the band insulator $SrTiO_3$, as discussed in Chapter 1.2.2. However, it can be anticipated that oxygen vacancies will also affect the film quality and the 2DEG.[275]

In this chapter, high-resolution imaging has been used to characterize $LaTiO_3/SrTiO_3$ heterostructures grown by our collaborators at UT-Austin. ELNES hyperspectral unmixing and mapping has also been used to investigate oxidation states and oxygen vacancies in combination with electrical measurement.

4.2 HRTEM imaging

The $LaTiO_3/SrTiO_3$ samples were grown by molecular beam epitaxy (MBE) using 5 mm $\times$ 5 mm $\times$ 0.5 mm TiO_2-terminated $SrTiO_3$ (001) single-crystal substrates. Pre-processing treatment included degreasing (solvent sonication and UV-ozone (UVO) cleaning) followed by ultra-high vacuum (UHV) annealing at 750°C for 30 min. The partial pressure of oxygen during the growth and the annealing process varied between samples, as summarized in the caption of Figure 4.1. The $LaTiO_3$ films in Figures 4.1 (a)(b) and (c) show good crystallinity, but the $LaTiO_3$ films in Figures 4.1 (d)(e) and (f) are amorphous. In contrast, the $SrTiO_3$ substrates in all samples have excellent

cyrstallinity. Thus, it is clear that growth at an oxygen partial pressure of lower than 10^{-7} Torr without post-growth annealing results in amorphous $LaTiO_3$ films.

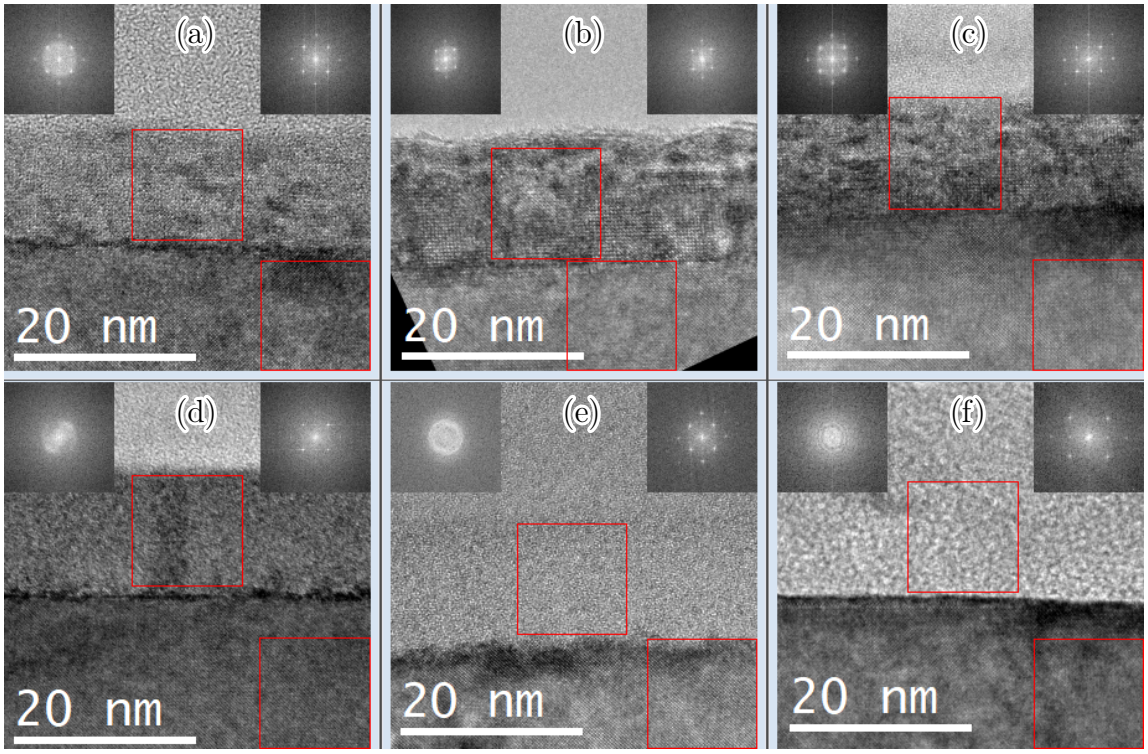

Figure 4.1. HRTEM images and diffractograms of $LaTiO_3$ film grown on $SrTiO_3$ at different conditions

In each figure, the lower part is $SrTiO_3$ substrate. The middle part is the $LaTiO_3$ film. The upper part is the epoxy glue introduced during TEM sample preparation. Diffractograms in the upper left corners are from the $LaTiO_3$ film, indicated by the red box in the middle. Diffractogram in the upper right corners are from the $SrTiO_3$ substrate, indicated by the red box at the bottom right. (a) (b) ~15 nm $LaTiO_3/SrTiO_3$. (c) ~15 nm $LaTiO_3/SrTiO_3$ with post-growth oxygen anneal (10^{-7} Torr O_2, 750°C, 30 min). (d) ~15 nm $LaTiO_3/SrTiO_3$ grown under 10^{-7} Torr O_2. (e) ~15 nm $LaTiO_3/SrTiO_3$ grown under 10^{-8} Torr O_2. (f) ~15 nm $LaTiO_3/SrTiO_3$ grown under 10^{-9} Torr O_2.

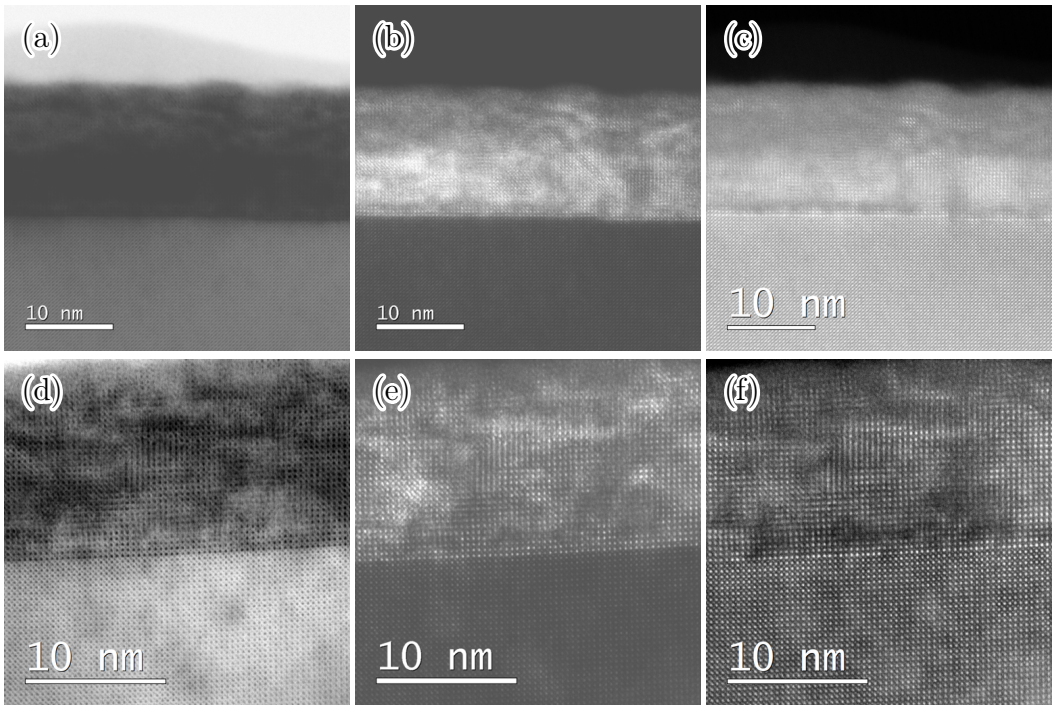

Figure 4.2. Aberration-corrected STEM images for the as-grown and annealed $LaTiO_3/SrTiO_3$ samples.

(a)(b) and (c) are images of the as-grown sample. (d)(e) and (f) are images of the sample with post-growth oxygen anneal (10^{-7} Torr O_2, 750°C, 10min). (a) and (d) are BF images. (b) and (e) are LAADF images. (c) and (f) are HAADF images.

Aberration-corrected STEM imaging was used to investigate the sample crystallinity in more detail. BF, HAADF and LAADF images were collected as described in Chapter 2.1.2. The BF, LAADF and HAADF images for the as-grown $LaTiO_3/SrTiO_3$ sample and the post-growth oxygen-annealed sample are compared in Figure 4.2. Differences between the as-grown sample and the annealed sample are not obvious. The $LaTiO_3$ near the interface has good crystallinity, but defects starts to appear after several unit cells above the interface. The defects gives significant

contrast in the LAADF images. In the upper part of the film, both crystalline and amorphous structure seem to coexist. The diagonal stripes along the (110) plane in the upper part of the film are very similar to the reported structure of $La_2Ti_2O_7$,[276] suggesting that significant Ti^{4+} may be present in the film.

4.4 ELNES hyperspectral unmixing and mapping

To further investigate the relationship between the structural, chemical and electrical properties of the $LaTiO_3/SrTiO_3$ interface, the ELNES hyperspectral unmixing and mapping method, as discussed in Chapter 2.4, was carried out for the as-deposited and annealed samples.

4.4.1 As-deposited $LaTiO_3/SrTiO_3$ sample

Figure 4.3 shows the hyperspectral unmixing results for the as-deposted $LaTiO_3/SrTiO_3$ sample. As discussed in Chapter 2.3.1.1, and simulated in Chapter 3.5, the Ti-L edge is sensitive to the Ti oxidation state: Ti^{4+} shows 4 peaks, whereas $Ti^{3+/2+}$ shows 2 peaks. (Although local lattice distortion also affects the shape of the Ti-L edge.) The green spectra in Figures 4.3 (a)(b) and (c) show reduction of Ti (Ti^{3+}) at the $LaTiO_3/SrTiO_3$ interface. Comparing these spectra with a reported spectrum[276] indicates that $LaTiO_3$ is almost (but not fully) Ti^{3+}. In particular, the blue spectrum is a mixture of 2 peaks and 4 peaks, indicating that the upper part of the sample (right part in the profile and map) has more Ti^{4+}.

The O-K edge is sensitive to cation type and oxidation state, and oxygen sub-lattice ordering. Peaks in reduced $SrTiO_3$ are "smeared". The result in the as-deposited

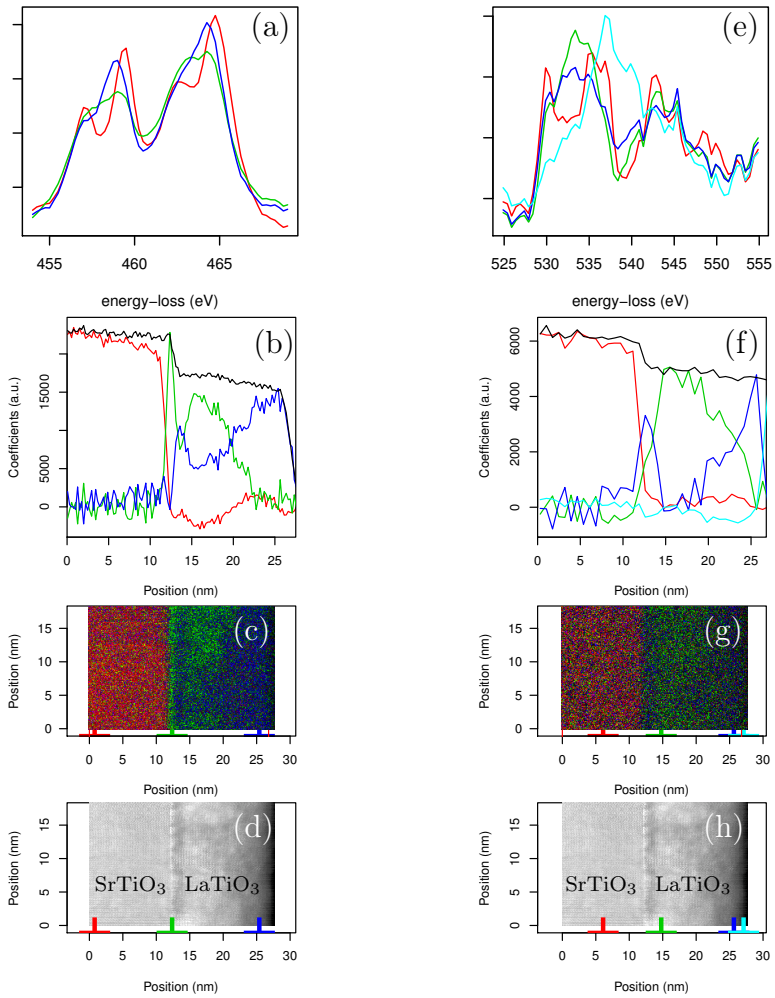

Figure 4.3. ELNES hyperspectral unmixing for Ti-L and O-K edges of as-deposited $LaTiO_3$ film on $SrTiO_3$.

(a)-(d) are from Ti-L edge. (e)-(h) are from O-K edge. (a)(e) are spectral signatures. (b)(f) are profiles of fitting coefficients (the abundance) averaged along the in-plane direction and the black lines in each profile is the sum of the color lines. (c)(g) are 2D maps of the fitting coefficients. (d)(h) are HAADF images acquired simultaneously with the spectral map. The substrate is at the left part of each profile or map.

sample is different from the reported $LaTiO_3/SrTiO_3$ interface where no oxygen vacancies are seen.[53] Comparing our spectra with reported spectra indicates that the dark blue spectrum is close to $SrTiO_{2.75}$ in Ref.[156], indicating that there is oxygen

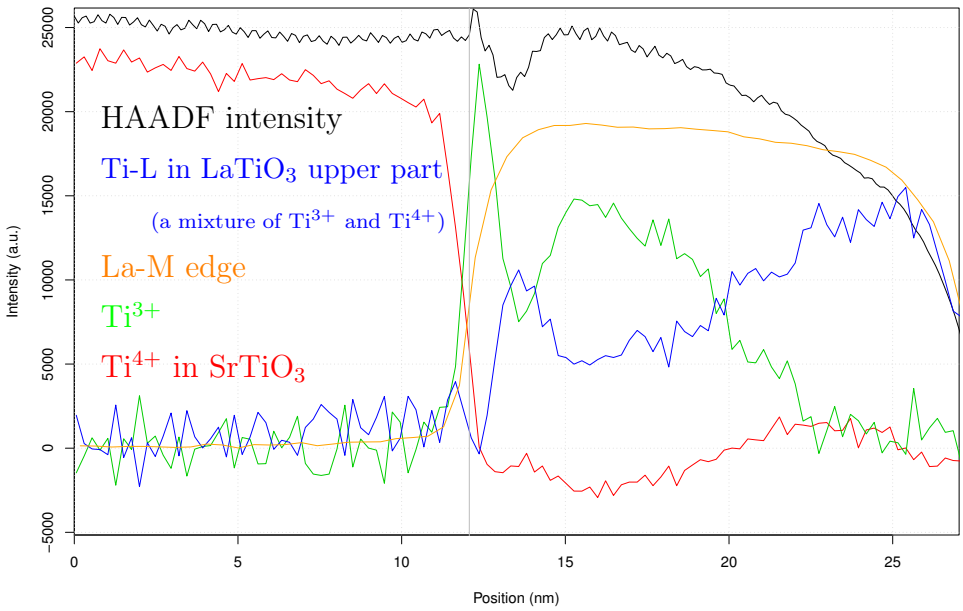

Figure 4.4. Summary of profiles from different ionization edges for the as-deposited sample.

sublattice disordering in the interface and in the upper part (left part in the profile and the map) of the $LaTiO_3$ film.

Figure 4.4 summarized the comparison between results from different ionization edges. The peak in the HAADF intensity corresponds to the LaO layer right at the interface. According to this peak, the position of the interface is labeled by the gray vertical line. The Ti^{3+} profile (green line) goes deeper into $SrTiO_3$ (to the left of the gray line) than the La profile (orange line), indicating the presence of the 2DEG at the interface on the STO side. This result is consistent with the previous report.[26]

From this hyperspectral unmixing study, it can be concluded that $LaTiO_3$ is not very uniform in the as-deposited sample, since both Ti^{3+} and Ti^{4+} are present in $LaTiO_3$. Moreover, there is a Ti^{3+} peak at the $LaTiO_3/SrTiO_3$ interface. Oxygen

sublattice disorder exists at the interface and in the upper part of the $LaTiO_3$. Oxygen vacancies may exist at the interface and may contribute to the conductivity. This is different from the reported LTO/STO system where the 2DEG was attributed to modulation doping.[26, 53]

4.4.2 Oxygen-annealed $LaTiO_3/SrTiO_3$ sample

Figures 4.5(a)-(d) shows the Ti-L ELNES hyperspectral unmixing result for the oxygen-annealed $LaTiO_3/SrTiO_3$ sample. Comparing our spectra with reported spectra, the $LaTiO_3$ film is actually a mixture of Ti^{3+} and Ti^{4+}. In comparison with the as-deposited sample shown in 4.3, the spectra in the Ti-L edge in the $LaTiO_3$ (green and blue) are closer to 4 peaks rather than 2 peaks. The spectrum in the upper part of the film (the right side in the profiles and maps in Figure 4.5) is closer to 2 peaks because it has more of the blue spectrum, and the blue spectrum is closer to 2 peaks rather than 4 peaks. This result is different from the as-deposited sample. In the as-deposited sample, the interface had more 2-peak component, whereas the interface had more 4-peak component in the oxygen-annealed sample. Increase in oxidation state or crystallinity can change the spectrum from 2 peaks into 4 peaks. In the case of the as-deposited sample, the area near the interface showed good crystallinity in the aberration-corrected images. Hence, Ti^{3+} at the interface in the as-deposited sample should be the most reasonable explanation. In the case of the annealed sample, there must be Ti^{4+} in the $LaTiO_3$ film, since Ti^{3+} should always show 2 peaks but 4 peaks were observed,

Figure 4.5(e)-(h) shows the O-K ELNES hyperspectral unmixing results. Compar-

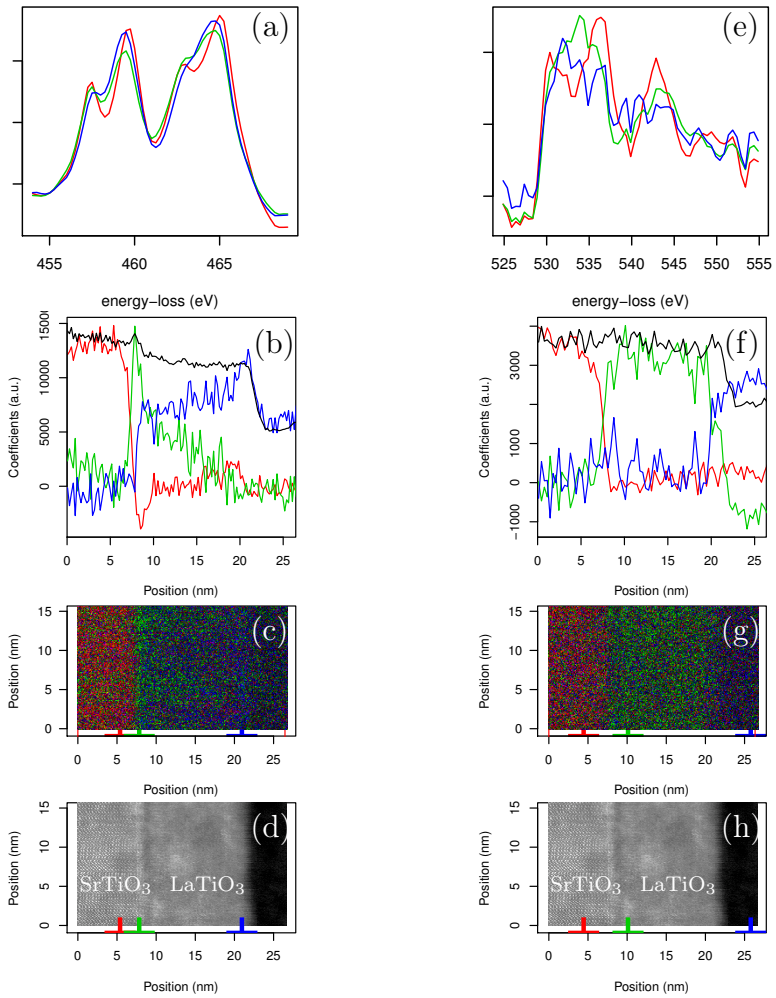

Figure 4.5. ELNES hyperspectral unmixing of Ti-L and O-K edge of the oxygen-annealed $LaTiO_3$ film on $SrTiO_3$.

(a)-(d) are from Ti-L edge. (e)-(h) are from O-K edge. (a)(e) are spectral signatures. (b)(f) are the profiles of fitting coefficients (the abundance) averaged along the in-plane direction and the black lines in each profile is the sum of the color lines. (c)(g) are 2D maps of the fitting coefficients. (d)(h) are HAADF images acquired simultaneously with the spectral map. The substrate is in the left part in each profile or map.

ing our spectra with reported spectra, the dark blue spectrum is close to $SrTiO_{2.75}$ in Ref.[26], indicating there is oxygen sublattice disorder at the upper part (right part of the profile and the map) of the $LaTiO_3$ film. This is different from the as-deposited sample, where the oxygen vacancies are located near the interface.

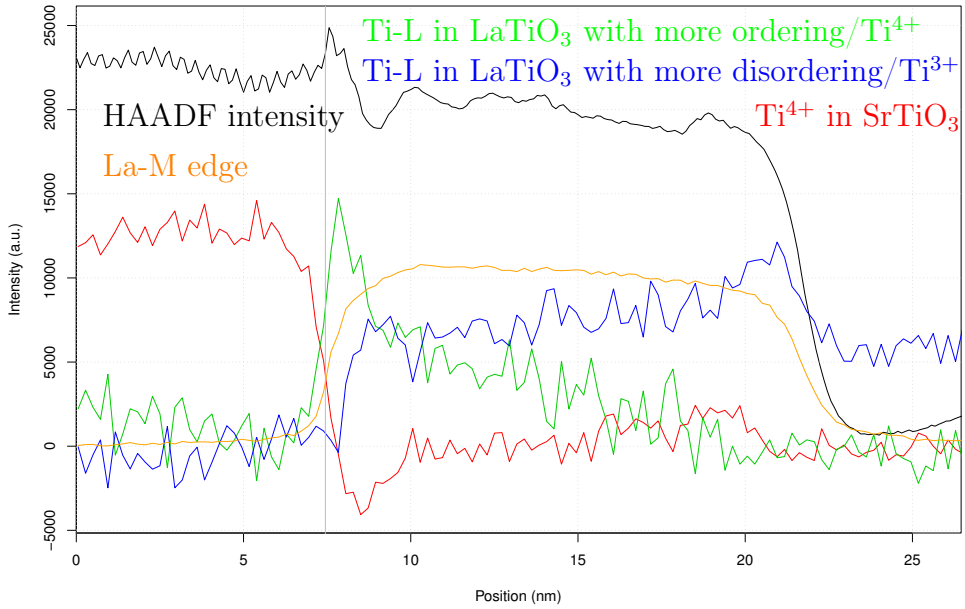

Figure 4.6. Summary of profiles from different ionization edges for the oxygen annealed sample.

Figure 4.6 is the summary of the oxygen-annealed sample from different ionization edges. The Ti^{3+} profile rises later than the La profile from the substrate to the film. This behavior is different than for the as-deposited sample and the reported $LaTiO_3/SrTiO_3$ interface with 2DEG.[26]

From the hyperspectral unmixing analysis, it can be concluded that the oxygen-annealed $LaTiO_3$ film is still not very uniform. ELNES spectra show both Ti^{3+} and Ti^{4+} present in the $LaTiO_3$. Moreover, there is a peak of Ti^{4+} at the $LaTiO_3/SrTiO_3$ interface, suggesting possible removal of the 2DEG as a result of by oxygen annealing.

4.5 Discussion

Both HRTEM and HRSTEM imaging show deterioration in film crystallinity in $LaTiO_3$ films a few unit cells away from the interface. Oxygen annealing did not significantly alter the crystallinity. ELNES hyperspectral unmixing and mapping showed that while the disordered structure in the upper part of $LaTiO_3$ remained largely unchanged, the lower part of the $LaTiO_3$ film changed from Ti^{3+} to Ti^{4+} with removal of oxygen vacancies and possibly 2DEG as well after oxygen annealing. This is consistent with the electrical measurement (not shown here) that the sheet carrier density is $\sim 6 - 7 \times 10^{16}\text{cm}^{-2}$ in the as-deposited sample but reduced to $\sim 4 - 5 \times 10^{16}\text{cm}^{-2}$ after annealing. However, from the line profile in Figure 4.4, the Ti^{3+} region in the $SrTiO_3$ is $\sim$ 1 nm in thickness, corresponding to a sheet carrier density of $\sim 10^{14}$ at most, which is much smaller than the electrical measurement. Hence, carriers deep in the bulk $SrTiO_3$, which might have been introduced by oxygen vacancies or La intermixing, may also contribute to the conductivity. The carrier doping in the bulk $SrTiO_3$, which may have very low volume concentration and large thickness, is below the detection limit of ELNES mapping.

Chapter 5

$EuO/SrTiO_3$ INTERFACES

5.1 The $EuO/SrTiO_3$ interface

The half-filled Eu $4f$ shell in EuO produced a large mangetic moment of $7\mu_B$[277, 278] and EuO shows ferromagnetic ordering below the Curie temperature of 69K.[279] As a ferromagnetic semiconductor, EuO is a promising material for spintronics. Lattice-matched EuO thin films have been grown on Si[280, 281], GaN[280] and yttria-stabilized ziconia (YSZ)[282]. DFT calculations predict a spin-polarized 2DEG at the $LaAlO_3$/EuO interface.[283, 284] However, EuO can be easily oxidized under conditions when crystalline $LaAlO_3$ is deposited.[285] Previous studies on depositing EuO on $SrTiO_3$ required BaO buffer layers in between to avoid the formation of Eu_2O_3, which is a non-magnetic material.[286] In the present study, EuO was grown on $SrTiO_3$ (001) surfaces directly using MBE at low temperature. It has been shown that the out-diffusion of oxygen can leave an oxygen-deficient $SrTiO_3$ layer near the interface even at room temperature.[285] In the following sections, aberration-corrected STEM imaging and ELNES hyperspectral unmixing and mapping are used for characterizing the $EuO/SrTiO_3$ system, and relating the structural and chemical properties to electrical measurements.

5.2 Imaging and ELNES mapping

5.2.1 Aberration-corrected STEM imaging

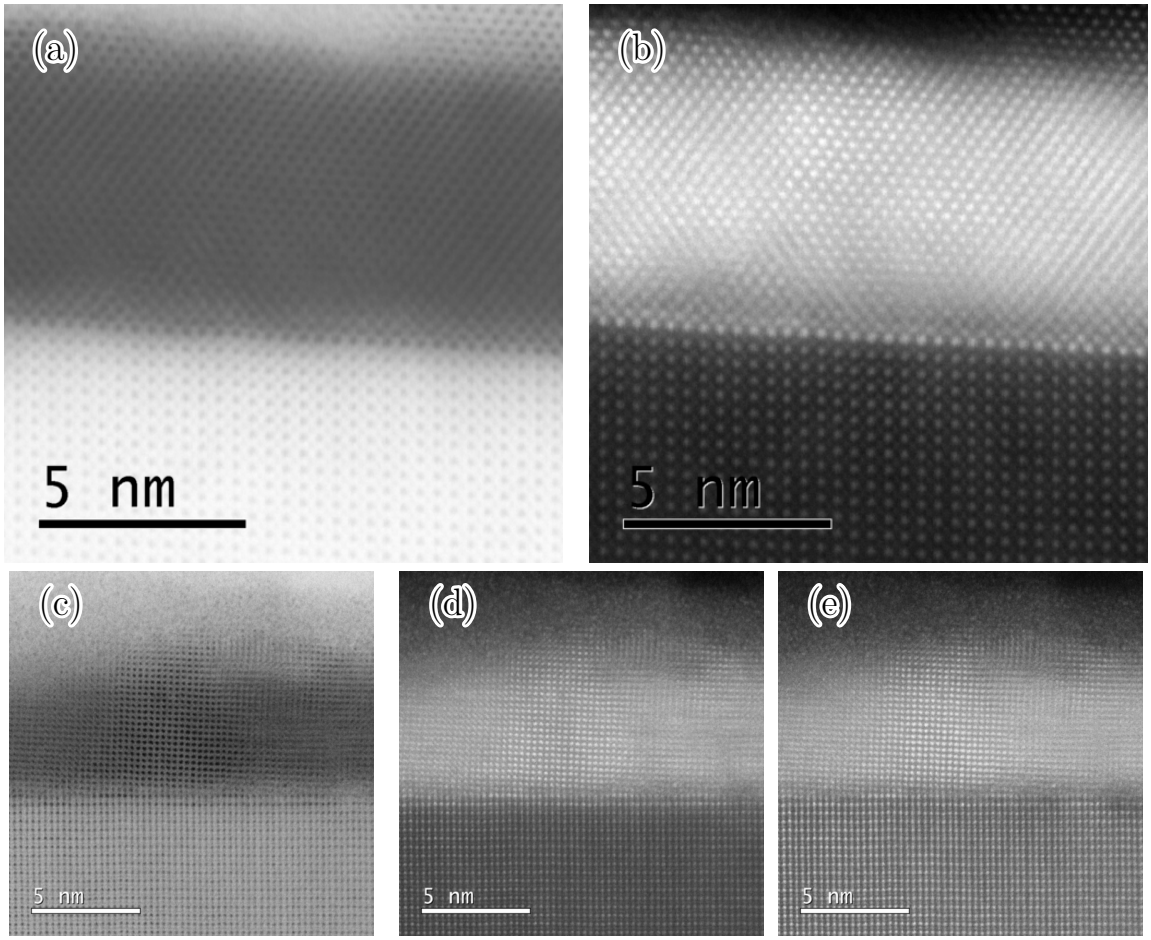

Figure 5.1. Aberration-corrected STEM imaging for the EuO/$SrTiO_3$ interface.

(a)(b) are HR-STEM images for the EuO/$SrTiO_3$ interface viewed along $SrTiO_3$[010] and EuO[110] projections. (c)(d)(e) are HR-STEM images for the EuO/$SrTiO_3$ interface viewed along $SrTiO_3$[110] and EuO[010] projections. (a)(c) are BF images, (b)(e) are HAADF images, (d) is LAADF image. In each image, the lower part is the $SrTiO_3$ substrate, the upper part is the EuO film.

Figure 5.1 shows images of the EuO/$SrTiO_3$ interface. The heavy Eu atoms

give bright contrast in the DF images and dark contrast in the BF images. The cubic lattice in the thin film matches the rock-salt crystal structure of EuO, and the measured out-of-plane lattice parameter matches the reported value of 5.14Å.[287] Lattice mismatch between materials is partially compensated by a small rotation between the $SrTiO_3$ and EuO crystal. Contrast variation in the EuO film indicates the presence of structural defects, which may be due to Eu^{3+}, possibly introduced during film growth or the TEM sample preparation process.

5.2.2 ELNES hyperspectral unmixing and mapping

Figure 5.2 summarizes the Eu-N, Ti-L and O-K ELNES hyperspectral unmixing results. A metallic Ti capping layer was deposited after EuO in the sample shown in order to prevent EuO from oxidation when exposed to air. It has been reported that the Eu-N edge shows two peaks in Eu_2O_3 but only one in EuO.[288] Although two spectral components are detected, in Figures 5.2 (a)-(d) the second peak can only be seen in the green component and it is very small. Therefore, the EuO film is slightly oxidized, which might happen during sample growth or TEM sample preparation. The slight oxidation of EuO film leaves the defects shown in the EuO film in Figure 5.1. The upper part of the film remains as Eu^{2+}. Three spectral components are detected for the Ti-L edge in Figure 5.2(e). The blue is Ti^{4+} in the bulk $SrTiO_3$, and the green is metallic Ti. The red is $Ti^{2+/3+}$, which appears at the top surface (left part in the profile and map in Figures 5.2(f) and (g)) due to oxidation of metallic Ti when the top surface was exposed to air. The red spectrum also appears above and below the EuO layer (about 10 nm and 18 nm in Figure 5.2(f)). The red peak at $\sim$ 10 nm is possibly due to chemical reaction between the metallic Ti and residual Eu^{3+} in the

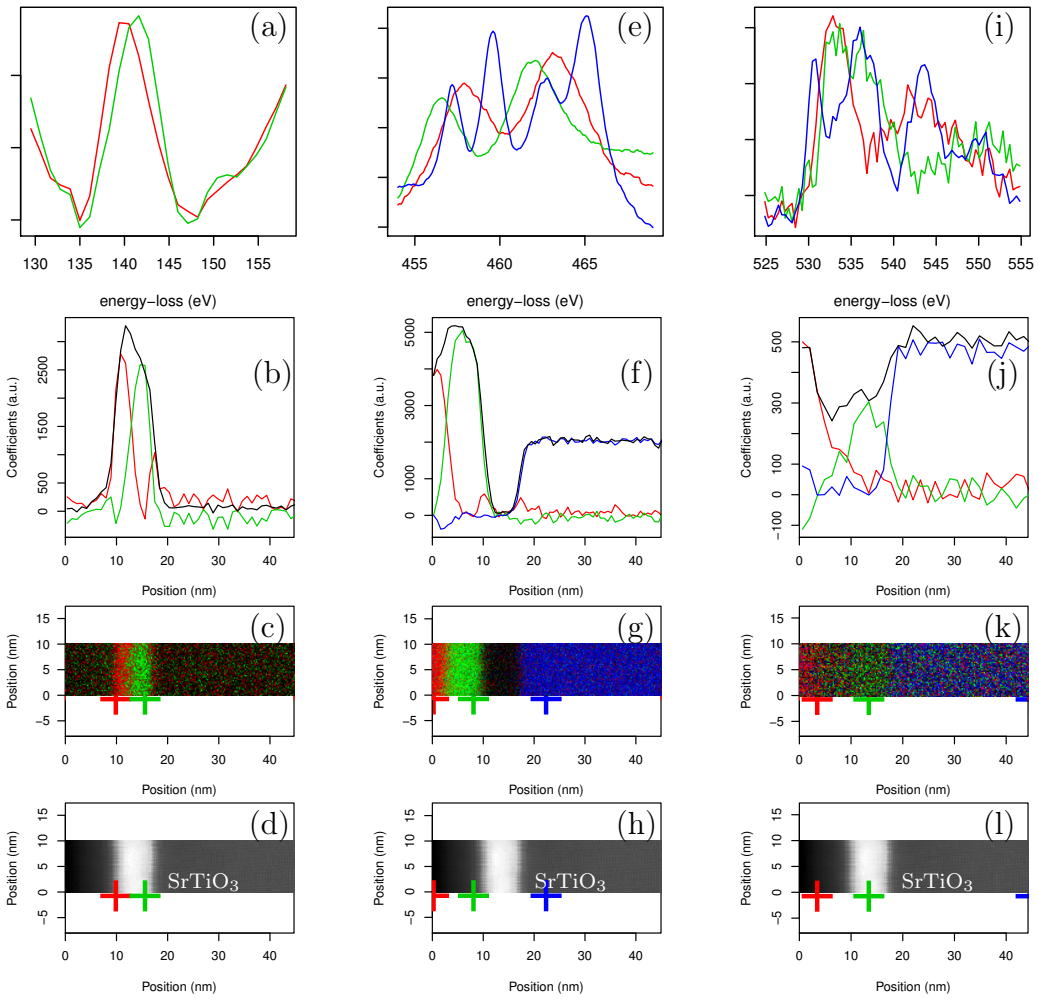

Figure 5.2. ELNES hyperspectral unmixing on Eu-N, Ti-L and O-K edge of the $EuO/SrTiO_3$ interface.

(a)-(d) are from Eu-N edge. (e)-(h) are from Ti-L edge. (i)-(l) are from O-K edge. (a)(e)(i) are spectral signatures. (b)(f)(j) are the profiles of fitting coefficients (the abundance) averaged along the in-plane direction and the black lines in each profile is the sum of the color lines. (c)(g)(k) are 2D maps of the fitting coefficients. (d)(h)(l) are HAADF images acquired simultaneously with the spectral map. The $SrTiO_3$ substrate is in the right part in each profile or map. EuO is at about 10 nm to 17 nm. Metallic Ti capping layer is at about 0 nm to 10nm.

EuO film, which has been reported in Ref.[288] The red peak at $\sim$ 15-20 nm is likely to be due to oxygen vacancies in the $SrTiO_3$ during growth of EuO. Due to SNR limitations in the experiment, and the small concentration of oxygen vacancies, the oxygen vacancies in $SrTiO_3$ are not shown as a separable component in the unmixed O-K edge in Figures 5.2(i)(j) and (k). However, the reduction of Ti in the $SrTiO_3$ (shown in Ti-L edge) proves the existence of 2DEG near the $EuO/SrTiO_3$ interface in the $SrTiO_3$ side.

5.3 Discussion

Large positive linear magnetoresistance (MR) was demonstrated at the $EuO/SrTiO_3$ interface, with the ordinary quadratic MR present below 150K, while the linear component emerges below $\sim$ 80K.[285] This behavior is different from the reported colossal positive magnetoresistance (CPMR) in the $LaAlO_3/SrTiO_3$ system, in which the linear behavior happens at high magnetic field.[37] Soft-x-ray angle-resolved photomission spectroscopy (SX-ARPES) shows the t_{2g} nature of the carriers.[285] The transition region from quadratic to linear dependence coincides with the Curie temperature of EuO. Thus, the origin of the positive linear MR is attributed to spin-polarized oxygen vacancies.[285] Under the magnetic field, d_{xy} shifts downwards. However, the measured electron density is about 3 orders of magnitude larger than the value derived from Hall measurements. This discrepancy could be due to the temperature effect, or because carriers in the bulk and near the interface both participate in the transport. However, the existence of confined oxygen vacancies is confirmed from the reduction of Ti near the interface. Future work on this system

should include measuring the partial occupancy in different bands near the surface below the Curie temperature using the angle-resolved ELNES.

Chapter 6

$BaTiO_3/SrTiO_3$ INTERFACE

6.1 Introduction

$BaTiO_3$ is a promising lead-free candidate material for ferroelectric field-effect transistors due to its large spontaneous polarization (0.26 C/m^2)[289] at room temperature and a Curie temperature (T_C) of between 120 and 130°C. The ferroelectricity and spontaneous polarization behavior are directly linked to the atomic structure. At low temperature, soft phonon modes emerge in $BaTiO_3$. As the phonon frequency is pure imaginary, displacement of Ti atoms from the center of the oxygen octahedra lowers the free energy, which leads to the spontaneous polarization.[290] In all phases of $BaTiO_3$, the Ti atom always displaces along the 8 equivalent <111> directions. In the cubic phase, the partial Ti displacement forms a short-range order-disorder structure along three different <100> directions, whereas the partial displacement in the tetragonal phase along the macro polarization direction $\mathbf{P}$ = [001] is fully ordered.[291] The order-disorder model explains the diffuse scattering observed in electron diffraction and X-ray diffraction patterns.[291, 292]

For device applications, the biaxial epitaxial strain introduced by lattice mismatch between the film and the substrate, affects the Curie temperature and the remanent polarization. For example, $BaTiO_3$ films grown on $DyScO_3$ with -1.7% in-plane strain have a ferroelectric transition temperature nearly 500°C higher and a remanent polarization of 250% higher than bulk $BaTiO_3$.[293] This behavior can be understood

in terms of the piezoelectric and elastic constants[294], and has been studied by DFT in the case of $BaTiO_3$ and $SrTiO_3$.[254–256]

Another phenomenon in the epitaxial system is that many as-deposited ferroelectric films tend to have a preferred polarization direction, commonly called self-polarization. The self-polarization can be affected or even tailored by dislocations, oxygen vacancies or other types of charged defects,[295–299] substrate vicinality,[300, 301] interface bonding,[302] chemical environment at the surface,[303, 304] polar discontinuity,[305] and flexoelectric effect.[298, 306] These effects not only cause changes in the hysteresis loops, but they can also change ferroelectric domain structure[301, 307] or even produce non-switchable interfaces.[308]

This chapter examines an unusually large polarization field and polarization gradient observed at the $BaTiO_3/SrTiO_3$ interface. The $BaTiO_3$ films were grown by MBE by our collaborators at UT-Austin. ELNES hyperspectral unmixing, and HR-STEM image quantification, combined with DFT calculations, were used to investigate this phenomenon.

6.2 Image Quantification

Figure 6.1 shows the ABF and HAADF images of the interface. The lower part is the $SrTiO_3$ substrate and the upper part is the $BaTiO_3$ film. Contrast variations are visible in the $BaTiO_3$ film in the HAADF image (6.1(b)), especially in the region near the interface and about 15 nm above the interface. The contrast variation originates primarily from the dechanneling effect due to the local random strain introduced by defects. Hence, defects in the layer are segregated near the interface and 15 nm above the interface in the $BaTiO_3$ film. An edge dislocation with the extra half-plane in the

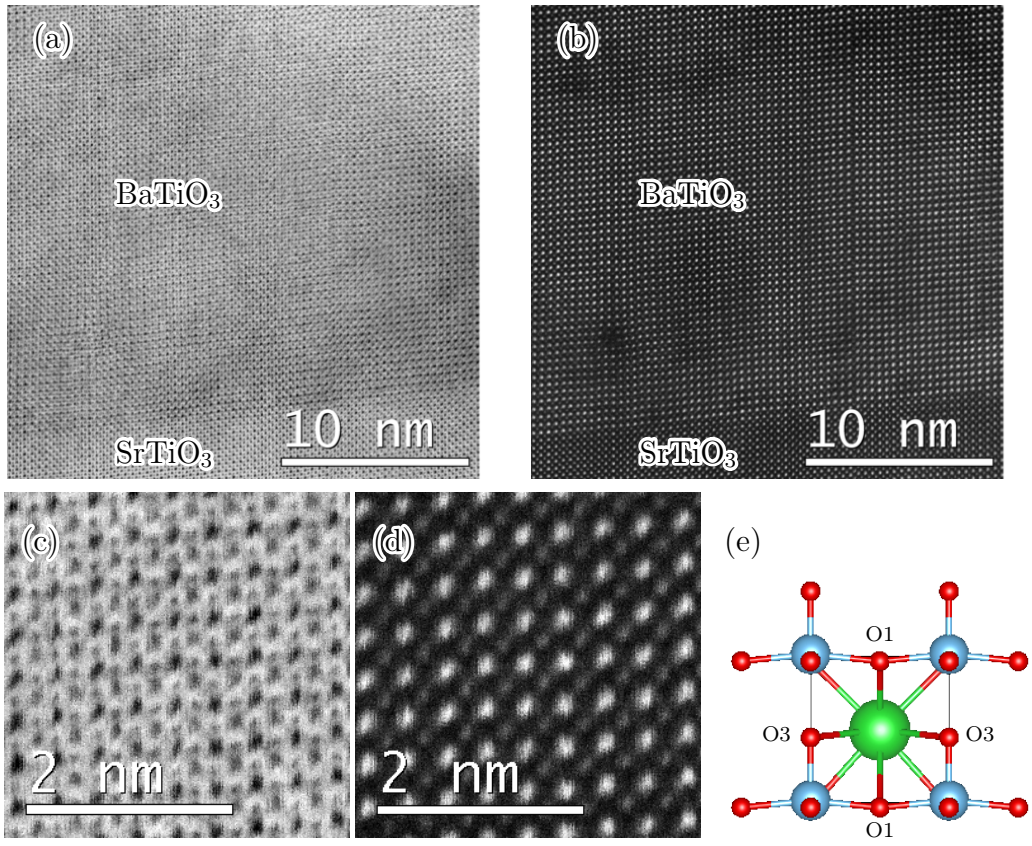

Figure 6.1. Aberration-corrected STEM images for $BaTiO_3/SrTiO_3$ interface. (a) and (c) are the ABF image. (b) and (d) are the HAADF image. (c)(d) magnify a small part of $BaTiO_3$ in (a) and (b). (e) is the atomic model showing the ferroelectric displacement. Green is Sr, blue is Ti, red is O, corresponding to the big, medium and small dots in the ABF and HAADF images, respectively.

lower part is visible at the lower left part of the image, about 5 nm away from the interface. Figure 6.1(e) shows the ferroelectric displacement in the tetragonal phase with the polarization direction pointing up. Atomic displacements can be directly observed from the ABF and HAADF images, as shown in the enlarged images (Figure 6.1(c)(d)). The origin of the defects and the influence on polarization are discussed later in this chapter.

Both the positions of atomic columns and the lattice parameters change with

polarization field in $BaTiO_3$. In order to quantify the polarization field and lattice parameters unit-cell-by-unit-cell, image quantification as described in Chapter 2.1.3 was carried out. The notations are adopted from Ref.[255] in order to be consistent with the literature. The Ti displacement is defined as the relative displacement between the position of the Ti atomic column and the center of the 4 nearest Sr atomic columns. The O displacement is defined as the relative displacement between the position of the O atomic column and the center of the 2 nearest Sr atomic columns. The oxygen atomic column in the TiO_2 layer is labelled as O1, and the oxygen atomic column in the SrO layer is labelled as O3. The lattice parameters were measured from HAADF images for better SNR. The positions of Ti atomic column were also measured from HAADF because image simulations show that the position of Ti atomic columns varies much less significantly with thickness in HAADF images than ABF images.

The image in Figure 6.1 was cropped to avoid the dislocation core on the left part and the blurred part on the right which is due to local sample tilt. Figure 6.2 shows large downward out-of-plane displacements (from the upper surface of the film pointing towards the substrate) of both O1 and O3 atomic columns. This displacement corresponds to a polarization field from the substrate pointing upwards to the surface. This polarization field arises near the interface on the $SrTiO_3$ side and reaches its maximum near the interface on the $BaTiO_3$ side. The field then slowly decaysmoving towards the upper part of the film. The in-plane displacement is significantly smaller than the out-of-plane direction and has much less variance.

Figures 6.3(a)-(d) show that the Ti displacements are similar to that of O1 and O3 except the magnitude is smaller and in the opposite direction, which also gives

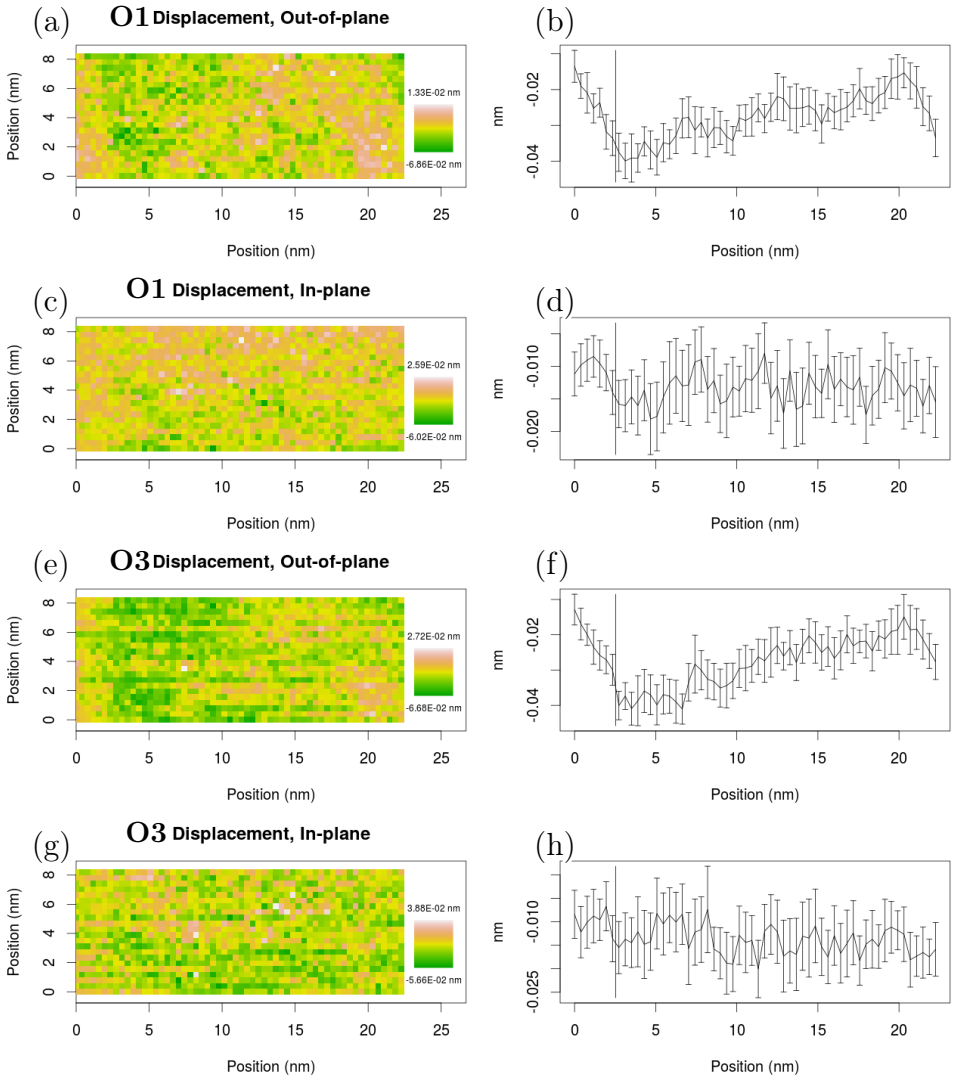

Figure 6.2. O1 and O3 atomic column displacements measured from ABF image.

(a)(c)(e)(g) are false color maps showing atomic displacement. Each pixel represents a unit cell. In each map, the x axis is the position in out-of-plane direction (film growth direction), and y axis is the position in in-plane direction (parallel to the surface). The substrate is on the left side. (b)(d)(f)(h) are displacement profiles averaged in each atomic plane parallel to the surface. The bar associated with each data point shows the 1.96σ (95% confidence) interval in each atomic plane. x axis is the position in film growth direction. The position of the $BaTiO_3/SrTiO_3$ interface is indicated by the vertical line. y axis is the atomic displacement in nanometers. (a)(b)(c)(d) are displacements of O1 atomic columns. (e)(f)(g)(h) are displacements of O3 atomic columns. (a)(b)(e)(f) are displacements in the out-of-plane direction (film growth direction). (c)(d)(g)(h) are displacements in the in-plane direction (parallel to the surface).

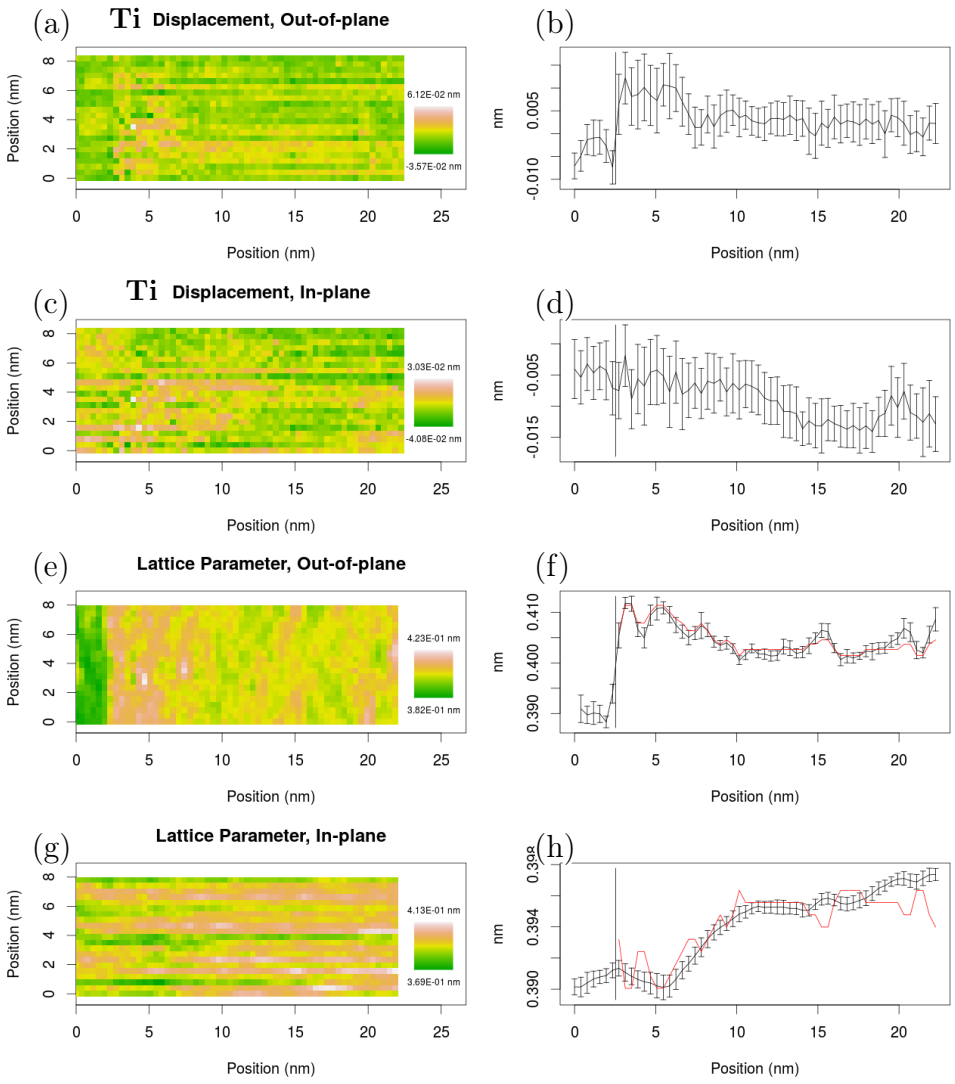

Figure 6.3. Ti atomic column displacements and lattice parameters measured from HAADF image.

(a)(b)(c)(d) are displacements of Ti atomic columns using the same representations as in Figure 6.2. (e)(f)(g)(h) are lattice parameters. (e)(f) are out-of-plane (film growth direction) lattice parameters. (g)(h) are in-plane (parallel to the surface) lattice parameters. In (a)(c)(e)(g) each pixel corresponds to one unit cell. x axis is the out-of-plane direction. y axis is the in-plane direction. The substrate is on the left side. (a)(d)(f)(h) are line profiles averaged along the in-plane direction. In (b)(d)(f)(h), x axis is the out-of-plane direction. The bar associated with each data point shows the 1.96σ (95% confidence) interval in each atomic plane. The red line is the fitted lattice parameters from DFT calculation using the measured c/a ratio as self variable.

a polarization field pointing upwards (from the substrate to the surface) in the out-of-plane direction. Figures 6.3(e)-(h) shows that the out-of-plane lattice parameters have similar trend as Ti displacements. Although the map in Figure 6.3(g) is largely affected by scanning noise, the profile in Figure 6.3(h) still has a narrow confidence interval because of averaging. It shows that the in-plane lattice parameter steadily increases in the $BaTiO_3$ film from the interface up to the surface. Most of the increases are in the 5 nm to 10 nm range. The trend of in-plane lattice parameters indicates strain relaxation. The relaxation is achieved by many misfit dislocations similar to the one shown in the lower left corner of Figure 6.1(a)(b), as well as the anti-phase boundaries (APB)[309].

Because of the presence of the strain gradient (lattice parameter changes with position), sample bending is unavoidable. The relative displacement of the same atomic column (Sr) between HAADF and ABF is sensitive to sample tilt. The sample tilt will give opposite displacement directions in HAADF and ABF[310] whereas the polarization displacement will give the same displacement direction in HAADF and ABF. Figures 6.6 (e)-(h) shows the relative displacement of Sr between HAADF and ABF. The relative displacement is not zero: it reaches its maximum at about 5 nm position due to the strain relaxation from edge dislocations. However, the in-plane displacement and out-of-plane displacement shows the same trend and similar values, which does not appear in Ti, O1 and O3 displacements. Therefore, the variation of Ti, O1 and O3 atomic displacements are not from sample tilt.

The correlation between lattice parameter and atomic displacement is partially due to the piezoelectric effect. The $BaTiO_3$ film near the interface is under compressive biaxial strain in the in-plane directions. The tetragonal $BaTiO_3$ with larger c/a ratio will have larger polarization. If c/a ratio is taken as self-variable, then the lattice

parameters matched the DFT predictions, as shown by the red line in Figure 6.3(f)(h), indicating that the measured Poisson ratio matched the DFT calculations. The small discrepancy near the surface (above 17 nm) is probably because the $BaTiO_3$ turns from tetragonal phase back into cubic phase when eptixial strain is fully relaxed while a tetragonal structure is always used in the DFT calculation. However, the measured displacement is significantly larger than given by DFT predictions. Indeed, it is almost twice as large as DFT predictions near the interface where the displacements reach the maximum. Therefore, the extra polarization field may be induced by electrical field.

6.3 ELNES Hyperspectral Unmixing

The aberration-corrected images in Figures 6.1(a)(b) shows defects in the $BaTiO_3$ film. To characterize these defects, ELNES spectrum mapping was conducted using the aberration-corrected Nion STEM operated at 100kV. The convergence semi-angle for the EELS was 30 mrad. The collection semi-angle was 45 mrad. The ELNES hyperspectral unmixing method, discussed in Chapter 2.4, was carried out for this $BaTiO_3/SrTiO_3$ sample.

Figure 6.4 shows the result of hyperspectral unmixing and mapping. Red and dark blue are spectra from bulk $SrTiO_3$ and $BaTiO_3$, respectively. Sky blue shows spectra from TiN capping electrode. Green is reduced Ti. In the Ti-L edge, the green spectrum is not completely 4 peaks, indicating the existence of Ti^{3+} in the $BaTiO_3$, especially near the interface. The e_g and t_{2g} peaks in O-K edge are not well separated, and the C1 - C3 peaks are also not well separated, suggesting the presence of oxygen vacancies at almost the same place where Ti^{3+} emerges.

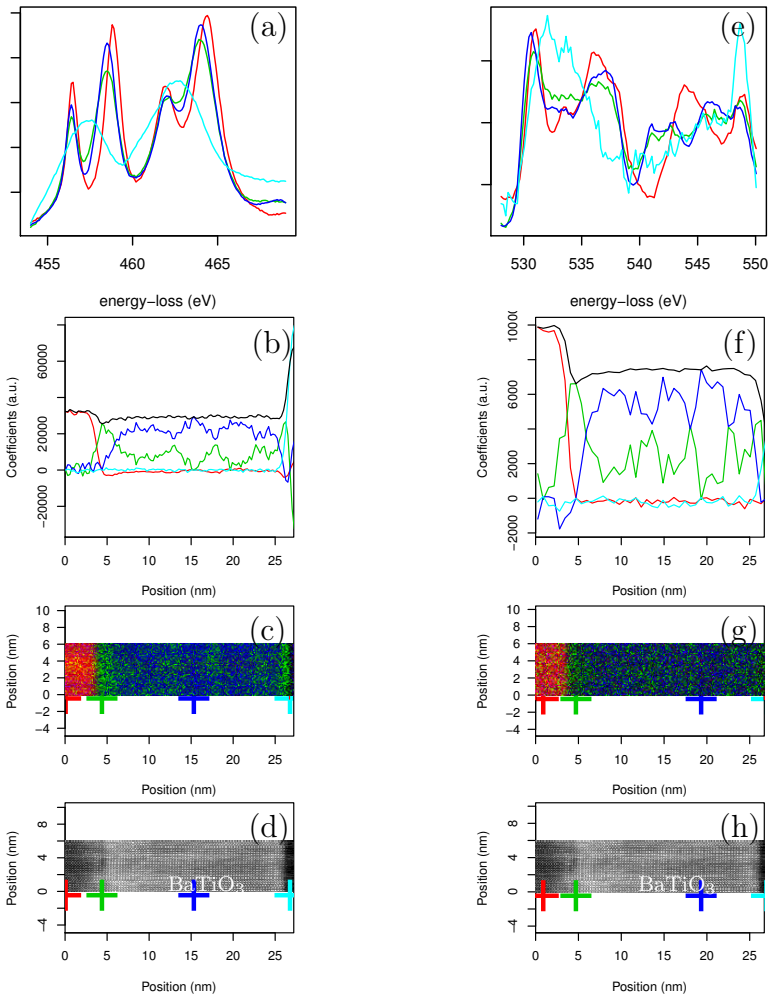

Figure 6.4. ELNES hyperspectral unmixing for Ti-L and O-K edges of the $BaTiO_3$ film on $SrTiO_3$.

(a)-(d) are from Ti-L edge. (e)-(h) are from O-K edge. (a)(e) are spectral signatures. (b)(f) are the profiles of fitting coefficients (the abundance) averaged along the in-plane direction and the black lines in each profile is the sum of the color lines. (c)(g) are 2D maps of fitting coefficients. (d)(h) are HAADF images acquired simultaneously with spectral map. The substrate is on the left side in each profile or map.

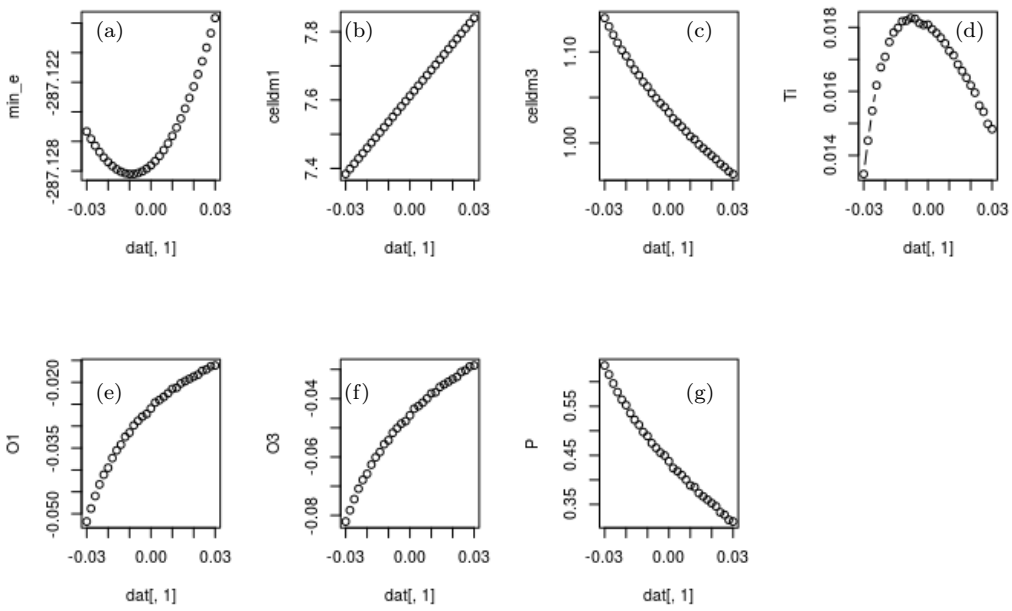

Figure 6.5. Summary of DFT calculations on strained $BaTiO_3$.

In each plot the x axis is the biaxial strain. (a) Minimum energy (in Ry). (b) In-plane lattice parameter (in atomic unit) (c) c/a ratio. (d) Ti atomic position in fractional coordinate. (e) O1 atomic position in fractional coordinate. (f) O3 atomic position in fractional coordinate. (g) Polarization calculated using Berry phase.

6.4 DFT Calculations

DFT calculations were performed using the QUANTUM-ESPRESSO software package.[232] The k point density is set to be $6 \times 6 \times 6$, and a series of Tetragonal $BaTiO_3$ unit cells with biaxial strain from -3% to +3% was built. Energy was minimized by varying atomic displacements in the inner loop and the c/a ratio in the outer loop. The results are summarized in Figure 6.5.

In order to relate the microscopic atomic displacement and the macroscopic polarization field, Born effective charges were adopted from Ref.[311], with Z^*_{Ti}=7.10,

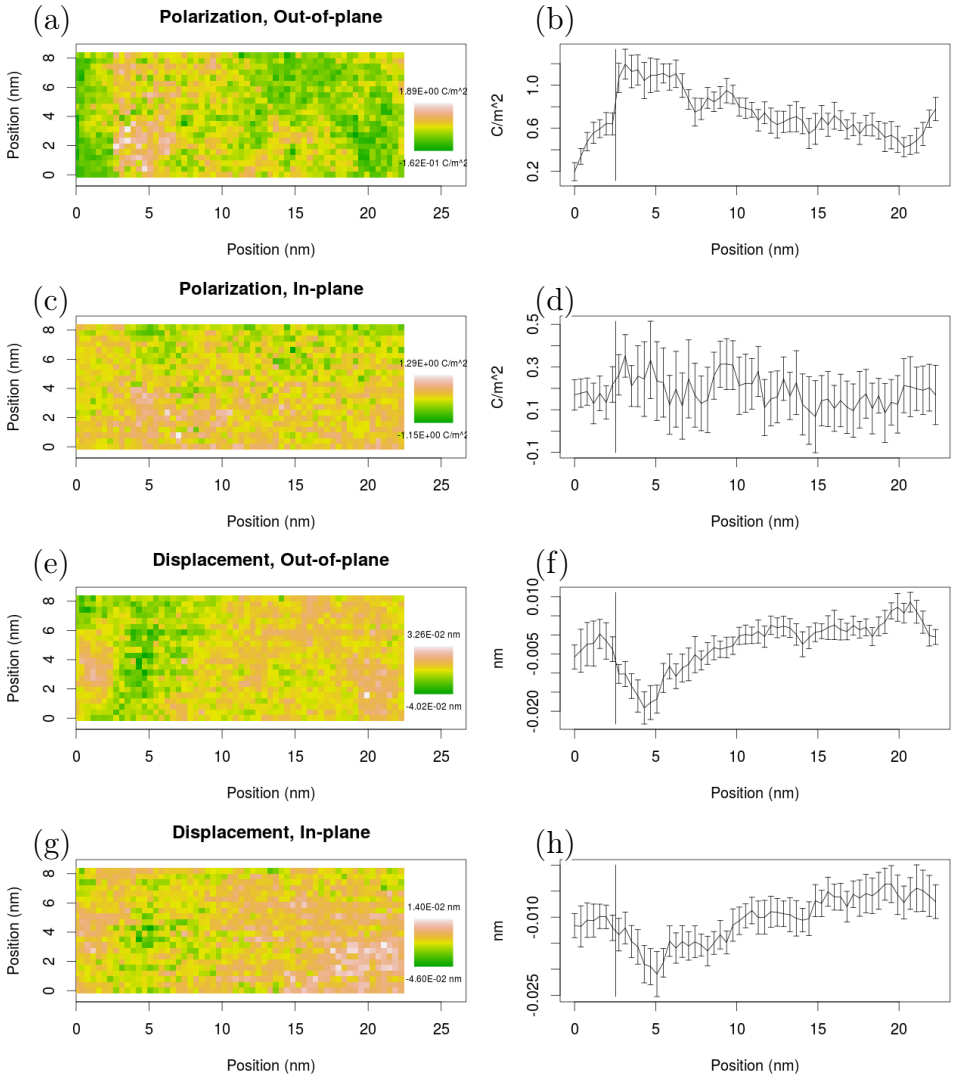

Figure 6.6. Polarization density map and profile

(a)(b) are out-of-plane (film growth direction) polarization density. (c)(d) are in-plane (parallel to the surface) polarization density. (e)(f) are out-of-plane displacement of Sr atomic column between the ABF and HAADF images. (g)(h) are in-plane displacement of Sr atomic column between the ABF and HAADF images. In (a)(c)(e)(g) each pixel corresponds to one unit cell. x axis is the out-of-plane direction. y axis is the in-plane direction. The substrate is on the left side. (b)(d)(f)(h) are line profiles averaged along the in-plane direction. x axis is the out-of-plane direction. y axis is the lattice parameter in nanometers. The bar associated with each data point shows the 1.96σ (95% confidence) interval in each atomic plane.

Z^*_{O1}=-2.12, and Z^*_{O3}=-5.56. The calculated polarization density is shown in Figure. 6.6

6.5 Discussion

The piezoelectric effect and large compressive biaxial strain at the interface contributes half of the unusually high polarization field in $BaTiO_3$ film near the interface. The presence of oxygen vacancies is likely to be responsible for the electric field that contributes the other half of the field. The origin of the oxygen vacancies remains to be investigated. It has been reported that compressive strain will increase the formation energy in perovskite $CaMnO_3$[312] and $BaTiO_3$,[313] and *vice versa*. The migration energy of oxygen vacancies in $BaTiO_3$ will also increase under compressive strain. However, the oxygen vacancies in this sample segregate near the interface where the compressive strain reaches its maximum. The oxygen vacancies are also unlikely to be introduced during sample growth, considering that the temperature is at 600°C while the migration energy is 0.45-0.8eV.[313–315] It has also been reported that $BaTiO_3$ films can be grown on $SrTiO_3$ substrate with automatic feeding of oxygen from the substrate.[316] Even if the oxygen vacancies form during sample growth, they can easily move away from the interface. The oxygen vacancies may be stabilized by the polarization discontinuity from $BaTiO_3$ to $SrTiO_3$. The maximum polarization density in the $BaTiO_3$ film is about $1.2 C/m^2$ near the interface, as shown in Figure 6.6(b). This polarization density corresponds to a charge density of $\sim 1e^-/uc^2$, The Ti oxidation state can be estimated from the Ti-L edge shown in Figure 6.4(a), since $Ti^{3.5+}$ already shows 2 peaks but the green spectrum is still 4 peaks. Therefore, the oxidation state of Ti near the interface is between 3.5+ and 4+. It requires several

unit cells in thickness to fully compensate the 1.2C/m^2 polar discontinuity, which is consistent with the thickness of the reduced Ti at the interface. The defect state introduced by oxygen vacancies can charge or discharge depending on the Fermi level. Therefore, the oxygen vacancies in the $BaTiO_3$, particularly 15 nm above the interface, may also compensate the polarization gradient in the $BaTiO_3$ film.

The possibility of flexoelectricity was also been considered. The out-of-plane polarization density is given by

$$P_3 = \mu_{12} \frac{\partial \varepsilon_{11}}{\partial x_3} \tag{6.1}$$

where ε is the strain tensor. μ_{12} is one of the components of the flexoelectric coefficients. The theoretically predicted flexoelectric coefficients are usually on the order of nC/m.[317–319] By considering that the strain gradient shown in Figure 6.3(h) is on the order of 10^{-3}nm^{-1}, the resulting polarization density is about 10^{-3}C/m, which is pointing in the correct direction but 3 orders of magnitude smaller than the observed value. The experimental flexoelectric coefficients of μ_{12} are much greater than calculated values, ranging from 400nC/m to 50μC/m.[320, 321] Assuming that the other half of the polarization is from the flexoelectric effect, μ_{12} should be $\sim$ 800nC/m, which on the same order as in $SrMnO_3$ film[321]. The discrepancy between the experimental and theoretical predicted flexoelectric coefficients needs to be clarified. If it is not related to other effects such as oxygen vacancy migration, the possibility that the flexoelectric effect caused the self-polarization cannot be ruled out.

In summary, unusually large polarization field was observed at the $BaTiO_3/SrTiO_3$ interface. The polarization field decayed when moving away from the interface, and became almost constant at 15 nm above the interface. Oxygen vacancies were observed in the $BaTiO_3$ film and separated near the interface. The piezoelectric effect contributes about half of the unusually large polarization field, The other half may

from oxygen vacancies or a flexoelectric effect. Oxygen vacancies are stabilized near the interface as it compensates the polar discontinuity across the interface. Future work should include a comparison between the as-deposited sample and annealed sample, and relating the electric properties with local atomic structure.

Chapter 7

SUMMARY AND FUTURE WORK

As discussed in Chapter 1, complex oxide interfaces exhibit a wide variety of properties such as ferromagnetism, magnetoresistance, conductivity, and superconductivity. Electron microscopy is a very useful tool for characterization, and not only provides structural information, but also provides chemical, or even electrical information at high spatial resolution. Chapter 2 discussed the microscopy methods used in this dissertation research, as well as other methods used in combination with microscopy. The γ-$Al_2O_3/SrTiO_3$ system was investigated in Chapter 3. The 2DEG at the interface is attributed to oxygen vacancies. The critical thickness is attributed to the out-diffusion of Ti that changes the Fermi level. Chapter 4 discussed the role of oxygen vacancies at the $LaTiO_3/SrTiO_3$ interface. The oxygen vacancies may also contribute to the conductivity besides the charge doping model, and they can be removed by oxygen annealing. In Chapter 5, a confined layer of oxygen vacancies is shown at the $EuO/SrTiO_3$ interface. The role of oxygen vacancies and their relationship with large positive linear magnetoresistance are discussed. Chapter 6 shows mapping of the unusually large polarization and polarization gradient found in $BaTiO_3$ films grown on $SrTiO_3$. The possible origins of the polarization are discussed.

There are problems still remaining unresolved or under debate. For example, how does the partial occupancy of the sub-bands at the interface between $SrTiO_3$ and other oxides relate to the conductivity, superconductivity and ferromagnetism? Would an interface free from oxygen vacancies lose all of the interesting interfacial effects discussed above? At what conditions will the polar discontinuity be compensated?

What is the origin of the large discrepancy between the experimental and theoretical predicted flexoelectric coefficients? Microscopy analysis already gave some hints to these questions. However, more microscopy techniques should be used to investigate these problems. Because properties such as ferromagnetism only exist at low temperature, cooling holders for *in situ* TEM may be used to investigate whether or not there is a phase transition. For the ferromagnetism and partial occupation of certain d orbitals, EMCD and angular-resolved EELS can be used. *In situ* TEM with electrical bias applied to the film can also be considered. The signal might be too weak if only kinetic effects are taken into consideration. Therefore, the experimental conditions must be tuned so that dynamic effects[322] can give good SNR.

The image or spectrum analysis methods can also be improved. The core of the problem is data reduction. For image processing, methods described in Chapter 2.1.3 use Gaussian fitting or moment method to reduce information from the image to positions and intensities of individual atomic columns, under the assumption that every atomic column is a Gaussian peak. If this assumption is not valid then bias will emerge. A better way to solve this issue might be two-dimensional PCA,[323] which has been used in human face representation and recognition. It has already been shown that only 2 eigen-images are needed to describe changes in thickness t and defocus Z.[324] Therefore, PCA eigen-images should be able to present the features on images better than Gaussian peaks. For hyperspectral analysis, only linear unmixing are currently considered. For non-linearly mixed spectra, such as a continuous shift of a peak, linear unmixing can only be an approximation. Manifold learning[325] is a promising method for non-linear dimensionality reduction and should be used. Moreover, noise modeling should be more carefully considered to avoid potential overfitting. For electron-beam-sensitive samples, electron dose is a problem. Real-

time data analysis should be implemented and provide feedback to the scanning and acquisition system in order to save electrons for regions or collection ranges that give the most variance from the sample.

[1]M. Imada, A. Fujimori, and Y. Tokura, "Metal-insulator transitions", Reviews of modern physics **70**, 1039 (1998).

[2]H. Hwang, Y Iwasa, M Kawasaki, B Keimer, N Nagaosa, and Y Tokura, "Emergent phenomena at oxide interfaces", Nature materials **11**, 103–113 (2012).

[3]H. Nishikawa, N. Iwata, T. Endo, Y. Takamura, G. Lee, and P. Mele, *Correlated functional oxides: nanocomposites and heterostructures* (Springer International Publishing, 2016).

[4]S Denev, A Kumar, M. Biegalski, H. Jang, C. Folkman, A Vasudevarao, Y Han, I. Reaney, S Trolier-McKinstry, C.-B. Eom, et al., "Magnetic color symmetry of lattice rotations in a diamagnetic material", Physical review letters **100**, 257601 (2008).

[5]T Riste, E. Samuelsen, K Otnes, and J Feder, "Critical behaviour of $SrTiO_3$ near the 105 k phase transition", Solid state communications **9**, 1455–1458 (1971).

[6]S. Hayward and E. Salje, "Cubic-tetragonal phase transition in $SrTiO_3$ revisited: landau theory and transition mechanism", Phase Transitions: A Multinational Journal **68**, 501–522 (1999).

[7]O. Tufte and P. Chapman, "Electron mobility in semiconducting strontium titanate", Physical Review **155**, 796 (1967).

[8]J. Goral and J. Greedan, "The magnetic structures of $LaTiO_3$ and $CeTiO_3$", Journal of magnetism and magnetic materials **37**, 315–321 (1983).

[9]G. Meijer, W Henggeler, J Brown, O.-S. Becker, J. Bednorz, C Rossel, and P Wachter, "Reduction of ordered moment in strongly correlated $LaTiO_{3+\delta}$ upon band filling", Physical Review B **59**, 11832 (1999).

[10]M Cwik, T Lorenz, J Baier, R Müller, G André, F Bourée, F Lichtenberg, A Freimuth, R Schmitz, E Müller-Hartmann, et al., "Crystal and magnetic structure of $LaTiO_3$: evidence for nondegenerate t_{2g} orbitals", Physical Review B **68**, 060401 (2003).

[11]J. Goodenough, *Magnetism and the chemical bond*, Interscience monographs on chemistry: Inorganic chemistry section (Interscience Publishers, 1963).

[12]M Arao, Y Inoue, and Y Koyama, "Features of the Jahn–Teller displacements in $LaTiO_3$", Journal of Physics and Chemistry of Solids **63**, 995–997 (2002).

[13]J Hemberger, H.-A. K. von Nidda, V Fritsch, J Deisenhofer, S Lobina, T Rudolf, P Lunkenheimer, F Lichtenberg, A Loidl, D Bruns, et al., "Evidence for Jahn-Teller distortions at the antiferromagnetic transition in $LaTiO_3$", Physical review letters **91**, 066403 (2003).

[14]T. Kiyama and M. Itoh, "Presence of $3d$ quadrupole moment in $LaTiO_3$ studied by Ti 47, 49 NMR", Physical review letters **91**, 167202 (2003).

[15]M. Mochizuki and M. Imada, "Orbital-spin structure and lattice coupling in $RTiO_3$ where R=La, Pr, Nd, and Sm", Physical review letters **91**, 167203 (2003).

[16]E Pavarini, S Biermann, A Poteryaev, A. Lichtenstein, A Georges, and O. Andersen, "Mott transition and suppression of orbital fluctuations in orthorhombic $3d^1$ perovskites", Physical review letters **92**, 176403 (2004).

[17]M. Haverkort, Z Hu, A. Tanaka, G Ghiringhelli, H Roth, M Cwik, T Lorenz, C Schüßler-Langeheine, S. Streltsov, A. Mylnikova, et al., "Determination of the orbital moment and crystal-field splitting in $LaTiO_3$", Physical review letters **94**, 056401 (2005).

[18]R. Schmitz, O. Entin-Wohlman, A. Aharony, A. B. Harris, and E. Müller-Hartmann, "Magnetic structure of the Jahn-Teller system $LaTiO_3$", Physical Review B **71**, 144412 (2005).

[19]I. Solovyev, "Lattice distortion and magnetism of $3d$-t_{2g} perovskite oxides", Physical Review B **74**, 054412 (2006).

[20]B Keimer, D Casa, A Ivanov, J. Lynn, M. v. Zimmermann, J. Hill, D Gibbs, Y Taguchi, and Y Tokura, "Spin dynamics and orbital state in $LaTiO_3$", Physical review letters **85**, 3946 (2000).

[21]G Khaliullin and S Maekawa, "Orbital liquid in three-dimensional mott insulator: $LaTiO_3$", Physical review letters **85**, 3950 (2000).

[22]C Ulrich, L. Ament, G Ghiringhelli, L Braicovich, M. M. Sala, N Pezzotta, T Schmitt, G Khaliullin, J Van Den Brink, H Roth, et al., "Momentum dependence of orbital excitations in Mott-insulating titanates", Physical review letters **103**, 107205 (2009).

[23]C Ulrich, G Khaliullin, M Guennou, H Roth, T Lorenz, and B Keimer, "Spin-orbital excitation continuum and anomalous electron-phonon interaction in the mott insulator $LaTiO_3$", Physical review letters **115**, 156403 (2015).

[24]M. Iliev, A. Litvinchuk, M. Abrashev, V. Popov, J Cmaidalka, B Lorenz, and R. Meng, "Phonons and magnetic excitations in the mott insulator $LaTiO_3$", Physical Review B **69**, 172301 (2004).

[25]J.-G. Cheng, Y Sui, J.-S. Zhou, J. B. Goodenough, and W. Su, "Transition from orbital liquid to Jahn-Teller insulator in orthorhombic perovskites $RTiO_3$", Physical review letters **101**, 087205 (2008).

[26]A. Ohtomo, D. Muller, J. Grazul, and H. Y. Hwang, "Artificial charge-modulationin atomic-scale perovskite titanate superlattices", Nature **419**, 378–380 (2002).

[27]A Ohtomo and H. Hwang, "A high-mobility electron gas at the $LaAlO_3/SrTiO_3$ heterointerface", Nature **427**, 423–426 (2004).

[28]Y. Chen, N Bovet, F. Trier, D. Christensen, F. Qu, N. H. Andersen, T. Kasama, W. Zhang, R Giraud, J Dufouleur, et al., "A high-mobility two-dimensional electron gas at the spinel/perovskite interface of γ-al2o3/srtio3", Nature communications **4**, 1371 (2013).

[29]N. Nakagawa, H. Y. Hwang, and D. A. Muller, "Why some interfaces cannot be sharp", Nature materials **5**, 204–209 (2006).

[30]R. Pentcheva and W. E. Pickett, "Charge localization or itineracy at $LaAlO_3/SrTiO_3$ interfaces: hole polarons, oxygen vacancies, and mobile electrons", Physical Review B **74**, 035112 (2006).

[31]S. W. LEE, Y. LIU, J. HEO, and R. G. GORDON, "Creation and control of two-dimensional electron gas using Al-based amorphous oxides/$SrTiO_3$ heterostructures grown by atomic layer deposition", Nano letters **12**, 4775–4783 (2012).

[32]J. Mannhart and D. Schlom, "Oxide interfaces—an opportunity for electronics", Science **327**, 1607–1611 (2010).

[33]N. Reyren, S Thiel, A. Caviglia, L. F. Kourkoutis, G Hammerl, C Richter, C. Schneider, T Kopp, A.-S. Rüetschi, D. Jaccard, et al., "Superconducting interfaces between insulating oxides", Science **317**, 1196–1199 (2007).

[34]K Ueno, S Nakamura, H Shimotani, A Ohtomo, N Kimura, T Nojima, H Aoki, Y Iwasa, and M Kawasaki, "Electric-field-induced superconductivity in an insulator", Nature materials **7**, 855–858 (2008).

[35]J Biscaras, N Bergeal, A Kushwaha, T Wolf, A Rastogi, R. Budhani, and J Lesueur, "Two-dimensional superconductivity at a mott insulator/band insulator interface $LaTiO_3/SrTiO_3$", Nature Communications **1**, 89 (2010).

[36]T Fujii, M Kawasaki, A Sawa, Y Kawazoe, H Akoh, and Y Tokura, "Electrical properties and colossal electroresistance of heteroepitaxial sr ru o 3/ sr ti 1- x nb x o 3 ($0.0002 \leqslant x \leqslant 0.02$) schottky junctions", Physical Review B **75**, 165101 (2007).

[37]A. David, Y. Tian, P. Yang, X. Gao, W. Lin, A. B. Shah, J.-M. Zuo, W. Prellier, and T. Wu, "Colossal positive magnetoresistance in surface-passivated oxygen-deficient strontium titanite", Scientific reports **5** (2015).

[38]A. Brinkman, M Huijben, M Van Zalk, J Huijben, U Zeitler, J. Maan, W. Van der Wiel, G Rijnders, D. Blank, and H Hilgenkamp, "Magnetic effects at the interface between non-magnetic oxides", Nature materials **6**, 493–496 (2007).

[39]J.-S. Lee, Y. Xie, H. Sato, C Bell, Y Hikita, H. Hwang, and C.-C. Kao, "Titanium d_{xy} ferromagnetism at the $LaAlO_3/SrTiO_3$ interface", Nature materials **12**, 703–706 (2013).

[40]S. Thiel, G. Hammerl, A Schmehl, C. Schneider, and J. Mannhart, "Tunable quasi-two-dimensional electron gases in oxide heterostructures", Science **313**, 1942–1945 (2006).

[41]C. Cen, S Thiel, G Hammerl, C. Schneider, K. Andersen, C. Hellberg, J Mannhart, and J Levy, "Nanoscale control of an interfacial metal–insulator transition at room temperature", Nature materials **7**, 298–302 (2008).

[42]M. Huijben, G. Rijnders, D. H. Blank, S. Bals, S. Van Aert, J. Verbeeck, G. Van Tendeloo, A. Brinkman, and H. Hilgenkamp, "Electronically coupled complementary interfaces between perovskite band insulators", Nature materials **5**, 556–560 (2006).

[43]W. Harrison, E. Kraut, J. Waldrop, and R. Grant, "Polar heterojunction interfaces", Physical Review B **18**, 4402 (1978).

[44]G. Baraff, J. A. Appelbaum, and D. Hamann, "Self-consistent calculation of the electronic structure at an abrupt GaAs-Ge interface", Physical Review Letters **38**, 237 (1977).

[45]J. Lee and A. A. Demkov, "Charge origin and localization at the n-type $SrTiO_3/LaAlO_3$ interface", Physical Review B **78**, 193104 (2008).

[46]C. Bark, D. Felker, Y. Wang, Y Zhang, H. Jang, C. Folkman, J. Park, S. Baek, H Zhou, D. Fong, et al., "Tailoring a two-dimensional electron gas at the laalo3/srtio3 (001) interface by epitaxial strain", Proceedings of the National Academy of Sciences **108**, 4720–4724 (2011).

[47]Y Tokura, Y Taguchi, Y Okada, Y Fujishima, T Arima, K Kumagai, and Y Iye, "Filling dependence of electronic properties on the verge of metal–Mott-insulator transition in $Sr_{1-x}La_xTiO_3$", Physical review letters **70**, 2126 (1993).

[48]S. Okamoto and A. J. Millis, "Electronic reconstruction at an interface between a mott insulator and a band insulator", Nature **428**, 630–633 (2004).

[49]S. Okamoto, A. J. Millis, and N. A. Spaldin, "Lattice relaxation in oxide heterostructures: $LaTiO_3/SrTiO_3$ superlattices", Physical review letters **97**, 056802 (2006).

[50]R. Pentcheva and W. E. Pickett, "Correlation-driven charge order at the interface between a mott and a band insulator", Physical review letters **99**, 016802 (2007).

[51]J. S. Kim, S. S. A. Seo, M. F. Chisholm, R. Kremer, H.-U. Habermeier, B. Keimer, and H. N. Lee, "Nonlinear Hall effect and multichannel conduction in $LaTiO_3/SrTiO_3$ superlattices", Physical Review B **82**, 201407 (2010).

[52]H. Zhou and J. Goodenough, "Localized or itinerant tio3 electrons in rtio3 perovskites", Journal of Physics: Condensed Matter **17**, 7395 (2005).

[53]H. Jang, D. Felker, C. Bark, Y Wang, M. K. Niranjan, C. Nelson, Y Zhang, D Su, C. Folkman, S. Baek, et al., "Metallic and insulating oxide interfaces controlled by electronic correlations", Science **331**, 886–889 (2011).

[54]Y. Chen, N Bovet, T. Kasama, W. Gao, S. Yazdi, C Ma, N. Pryds, and S. Linderoth, "Room temperature formation of high-mobility two-dimensional electron gases at crystalline complex oxide interfaces", Advanced Materials **26**, 1462–1467 (2014).

[55]K. J. Kormondy, A. B. Posadas, T. Q. Ngo, S. Lu, N. Goble, J. Jordan-Sweet, X. P. Gao, D. J. Smith, M. R. McCartney, J. G. Ekerdt, et al., "Quasi-two-dimensional electron gas at the epitaxial alumina/srtio3 interface: control of oxygen vacancies", Journal of Applied Physics **117**, 095303 (2015).

[56]C. Schneider, M Esposito, I Marozau, K Conder, M Doebeli, Y. Hu, M Mallepell, A Wokaun, and T Lippert, "The origin of oxygen in oxide thin films: role of the substrate", Applied Physics Letters **97**, 192107 (2010).

[57]T. Q. Ngo, N. J. Goble, A. Posadas, K. J. Kormondy, S. Lu, M. D. McDaniel, J. Jordan-Sweet, D. J. Smith, X. P. Gao, A. A. Demkov, et al., "Quasi-two-dimensional electron gas at the interface of γ-al2o3/srtio3 heterostructures grown by atomic layer deposition", Journal of Applied Physics **118**, 115303 (2015).

[58]M. Warusawithana, C Richter, J. Mundy, P Roy, J Ludwig, S Paetel, T Heeg, A. Pawlicki, L. Kourkoutis, M Zheng, et al., "$LaAlO_3$ stoichiometry is key to electron liquid formation at $LaAlO_3/SrTiO_3$ interfaces", Nature communications **4** (2013).

[59]P. Tasker, "The stability of ionic crystal surfaces", Journal of Physics C: Solid State Physics **12**, 4977 (1979).

[60]P Schütz, F Pfaff, P Scheiderer, Y. Chen, N. Pryds, M. Gorgoi, M Sing, and R Claessen, "Band bending and alignment at the spinel/perovskite γ- al 2 o 3/srtio 3 heterointerface", Physical Review B **91**, 165118 (2015).

[61]G. Singh-Bhalla, C. Bell, J. Ravichandran, W. Siemons, Y. Hikita, S. Salahuddin, A. F. Hebard, H. Y. Hwang, and R. Ramesh, "Built-in and induced polarization across laalo3/srtio3 heterojunctions", Nature Physics **7**, 80–86 (2011).

[62]A. Kalabukhov, R. Gunnarsson, J. Börjesson, E. Olsson, T. Claeson, and D. Winkler, "Effect of oxygen vacancies in the $SrTiO_3$ substrate on the electrical properties of the $LaAlO_3/SrTiO_3$ interface", Physical Review B **75**, 121404 (2007).

[63]G. Herranz, M. Basletić, M. Bibes, C Carrétéro, E. Tafra, E Jacquet, K. Bouzehouane, C Deranlot, A. Hamzić, J.-M. Broto, et al., "High mobility in $LaAlO_3/SrTiO_3$ heterostructures: origin, dimensionality, and perspectives", Physical review letters **98**, 216803 (2007).

[64]A. Caviglia, S. Gariglio, C. Cancellieri, B. Sacepe, A. Fete, N. Reyren, M. Gabay, A. Morpurgo, and J.-M. Triscone, "Two-dimensional quantum oscillations of the conductance at laalo 3/srtio 3 interfaces", Physical review letters **105**, 236802 (2010).

[65]J. N. Eckstein, "Oxide interfaces: watch out for the lack of oxygen", Nature materials **6**, 473–474 (2007).

[66]N Pavlenko, T Kopp, E. Tsymbal, J Mannhart, and G. Sawatzky, "Oxygen vacancies at titanate interfaces: two-dimensional magnetism and orbital reconstruction", Physical Review B **86**, 064431 (2012).

[67]A. Santander-Syro, O Copie, T Kondo, F Fortuna, S Pailhes, R Weht, X. Qiu, F Bertran, A Nicolaou, A Taleb-Ibrahimi, et al., "Two-dimensional electron gas with universal subbands at the surface of srtio3", Nature **469**, 189–193 (2011).

[68]Y Aiura, I Hase, H Bando, T Yasue, T Saitoh, and D. Dessau, "Photoemission study of the metallic state of lightly electron-doped srtio 3", Surface science **515**, 61–74 (2002).

[69]W Meevasana, P. King, R. He, S. Mo, M Hashimoto, A. Tamai, P Songsiriritthigul, F. Baumberger, and Z. Shen, "Creation and control of a two-dimensional electron liquid at the bare srtio3 surface", Nature materials **10**, 114–118 (2011).

[70]R. C. Hatch, K. D. Fredrickson, M. Choi, C. Lin, H. Seo, A. B. Posadas, and A. A. Demkov, "Surface electronic structure for various surface preparations of nb-doped srtio3 (001)", Journal of Applied Physics **114**, 103710 (2013).

[71]Z. Hou and K. Terakura, "Defect states induced by oxygen vacancies in cubic srtio3: first-principles calculations", Journal of the Physical Society of Japan **79**, 114704 (2010).

[72]C. Lin and A. A. Demkov, "Electron correlation in oxygen vacancy in $SrTiO_3$", Physical review letters **111**, 217601 (2013).

[73]G Herranz, F Sánchez, N Dix, M Scigaj, and J Fontcuberta, "High mobility conduction at (110) and (111) laalo3/srtio3 interfaces", Scientific Reports **2**, 758 (2012).

[74]Y. Chen, N. Pryds, J. E. Kleibeuker, G. Koster, J. Sun, E. Stamate, B. Shen, G. Rijnders, and S. Linderoth, "Metallic and insulating interfaces of amorphous srtio3-based oxide heterostructures", Nano Letters **11**, 3774–3778 (2011).

[75]Z. Liu, C. Li, W. Lü, X. Huang, Z Huang, S. Zeng, X. Qiu, L. Huang, A Annadi, J. Chen, et al., "Origin of the two-dimensional electron gas at laalo 3/srtio 3 interfaces: the role of oxygen vacancies and electronic reconstruction", Physical Review X **3**, 021010 (2013).

[76]A. B. Posadas, K. J. Kormondy, W. Guo, P. Ponath, J. Geler-Kremer, T. Hadamek, and A. A. Demkov, "Scavenging of oxygen from $SrTiO_3$ during oxide thin film deposition and the formation of interfacial 2degs", Journal of Applied Physics **121**, 105302 (2017).

[77]S. A. Chambers, M. H. Engelhard, V Shutthanandan, Z. Zhu, T. C. Droubay, L. Qiao, P. Sushko, T. Feng, H. D. Lee, T. Gustafsson, et al., "Instability, intermixing and electronic structure at the epitaxial heterojunction", Surface Science Reports **65**, 317–352 (2010).

[78]L. Qiao, T. C. Droubay, V Shutthanandan, Z. Zhu, P. Sushko, and S. A. Chambers, "Thermodynamic instability at the stoichiometric laalo3/srtio3 (001) interface", Journal of Physics: Condensed Matter **22**, 312201 (2010).

[79]L. Qiao, T. C. Droubay, T. C. Kaspar, P. Sushko, and S. A. Chambers, "Cation mixing, band offsets and electric fields at $LaAlO_3/SrTiO_3$ (001) heterojunctions with variable La: Al atom ratio", Surface Science **605**, 1381–1387 (2011).

[80]P. Willmott, S. Pauli, R Herger, C. Schlepütz, D Martoccia, B. Patterson, B Delley, R Clarke, D Kumah, C Cionca, et al., "Structural basis for the conducting interface between laalo 3 and srtio 3", Physical Review Letters **99**, 155502 (2007).

[81]S. A. Chambers, "Understanding the mechanism of conductivity at the $LaAlO_3/SrTiO_3$ (001) interface", Surface Science **605**, 1133–1140 (2011).

[82]L. Yu and A. Zunger, "A polarity-induced defect mechanism for conductivity and magnetism at polar–nonpolar oxide interfaces", Nature Communications **5** (2014).

[83]V Vonk, J Huijben, D Kukuruznyak, A Stierle, H Hilgenkamp, A Brinkman, and S Harkema, "Polar-discontinuity-retaining a-site intermixing and vacancies at srtio 3/laalo 3 interfaces", Physical Review B **85**, 045401 (2012).

[84]S. Y. Moon, C. W. Moon, H. J. Chang, T. Kim, C.-Y. Kang, H.-J. Choi, J.-S. Kim, S.-H. Baek, and H. W. Jang, "Comprehensive study on critical role of surface oxygen vacancies for 2deg formation and annihilation in laalo3/srtio3 heterointerfaces", Electronic Materials Letters **12**, 243–250 (2016).

[85]L. Qiao, T. C. Droubay, T. Varga, M. E. Bowden, V Shutthanandan, Z. Zhu, T. C. Kaspar, and S. A. Chambers, "Epitaxial growth, structure, and intermixing at the laalo 3/srtio 3 interface as the film stoichiometry is varied", Physical Review B **83**, 085408 (2011).

[86]E Breckenfeld, N Bronn, J Karthik, A. Damodaran, S Lee, N Mason, and L. Martin, "Effect of growth induced (non) stoichiometry on interfacial conductance in laalo 3/srtio 3", Physical review letters **110**, 196804 (2013).

[87]R Ohtsuka, M Matvejeff, K Nishio, R Takahashi, and M Lippmaa, "Transport properties of $LaTiO_3/SrTiO_3$ heterostructures", Applied Physics Letters **96**, 192111 (2010).

[88]J Biscaras, N Bergeal, S Hurand, C Grossetête, A Rastogi, R. Budhani, D LeBoeuf, C Proust, and J Lesueur, "Two-dimensional superconducting phase in latio 3/srtio 3 heterostructures induced by high-mobility carrier doping", Physical review letters **108**, 247004 (2012).

[89]R. Pentcheva and W. E. Pickett, "Ionic relaxation contribution to the electronic reconstruction at the *n*-type $LaAlO_3/SrTiO_3$ interface", Physical Review B **78**, 205106 (2008).

[90]R. Pentcheva and W. E. Pickett, "Avoiding the polarization catastrophe in laalo 3 overlayers on srtio 3 (001) through polar distortion", Physical review letters **102**, 107602 (2009).

[91]Z. Zhong and P. J. Kelly, "Electronic-structure–induced reconstruction and magnetic ordering at the $LaAlO_3/SrTiO_3$ interface", EPL (Europhysics Letters) **84**, 27001 (2008).

[92]Z. S. Popović, S. Satpathy, and R. M. Martin, "Origin of the two-dimensional electron gas carrier density at the $LaAlO_3$ on $SrTiO_3$ interface", Physical review letters **101**, 256801 (2008).

[93]Z Huang, X. R. Wang, Z. Liu, W. Lü, S. Zeng, A Annadi, W. Tan, X. Qiu, Y. Zhao, M Salluzzo, et al., "Conducting channel at the laalo 3/srtio 3 interface", Physical Review B **88**, 161107 (2013).

[94]M Salluzzo, J. Cezar, N. Brookes, V Bisogni, G. De Luca, C Richter, S Thiel, J Mannhart, M Huijben, A Brinkman, et al., "Orbital reconstruction and the two-dimensional electron gas at the $LaAlO_3/SrTiO_3$ interface", Physical review letters **102**, 166804 (2009).

[95]M Salluzzo, S. Gariglio, X Torrelles, Z. Ristic, R Di Capua, J Drnec, M. M. Sala, G Ghiringhelli, R Felici, and N. Brookes, "Structural and electronic reconstructions at the laalo3/srtio3 interface", Advanced Materials **25**, 2333–2338 (2013).

[96]S. S. A. Seo, Z. Marton, W. Choi, G. Hassink, D. Blank, H. Y. Hwang, T. W. Noh, T. Egami, and H. N. Lee, "Multiple conducting carriers generated in laalo 3/srtio 3 heterostructures", Applied Physics Letters **95**, 082107 (2009).

[97]B. Jalan, S. Stemmer, S. Mack, and S. J. Allen, "Two-dimensional electron gas in δ-doped srtio 3", Physical Review B **82**, 081103 (2010).

[98]C Bell, S Harashima, Y Kozuka, M Kim, B. G. Kim, Y Hikita, and H. Hwang, "Dominant mobility modulation by the electric field effect at the laalo 3/srtio 3 interface", Physical review letters **103**, 226802 (2009).

[99]M. B. Shalom, A Ron, A Palevski, and Y Dagan, "Shubnikov–de haas oscillations in srtio 3/laalo 3 interface", Physical review letters **105**, 206401 (2010).

[100]V. K. Guduru, A McCollam, J. Maan, U Zeitler, S Wenderich, M. Kruize, A Brinkman, M Huijben, G Koster, D. Blank, et al., "Multi-band conduction behaviour at the interface of laalo3/srtio3 heterostructures", Journal of the Korean Physical Society **63**, 437–440 (2013).

[101]S. Banerjee, O. Erten, and M. Randeria, "Ferromagnetic exchange, spin-orbit coupling and spiral magnetism at the $LaAlO_3/SrTiO_3$ interface", Nature physics **9**, 626–630 (2013).

[102]M Salluzzo, S. Gariglio, D. Stornaiuolo, V Sessi, S Rusponi, C Piamonteze, G. De Luca, M Minola, D Marré, A Gadaleta, et al., "Origin of interface magnetism in bimno 3/srtio 3 and laalo 3/srtio 3 heterostructures", Physical review letters **111**, 087204 (2013).

[103]J. Park, B.-G. Cho, K. Kim, J Koo, H Jang, K.-T. Ko, J.-H. Park, K.-B. Lee, J.-Y. Kim, D. Lee, et al., "Oxygen-vacancy-induced orbital reconstruction of ti ions at the interface of laalo 3/srtio 3 heterostructures: a resonant soft-x-ray scattering study", Physical review letters **110**, 017401 (2013).

[104]L. Li, C Richter, J Mannhart, and R. Ashoori, "Coexistence of magnetic order and two-dimensional superconductivity at laalo3/srtio3 interfaces", Nature physics **7**, 762–766 (2011).

[105]M. R. Fitzsimmons, N. Hengartner, S Singh, M Zhernenkov, F. Bruno, J Santamaria, A. Brinkman, M. Huijben, H. Molegraaf, J de La Venta, et al., "Upper limit to magnetism in laalo 3/srtio 3 heterostructures", Physical review letters **107**, 217201 (2011).

[106]Z Salman, O Ofer, M Radovic, H Hao, M. B. Shalom, K. Chow, Y Dagan, M. Hossain, C. Levy, W. MacFarlane, et al., "Nature of weak magnetism in srtio 3/laalo 3 multilayers", Physical review letters **109**, 257207 (2012).

[107]X Wang, G Baskaran, Z. Liu, J Huijben, J. Yi, A Annadi, A. R. Barman, A Rusydi, S Dhar, Y. Feng, et al., "Electronic phase separation at the laalo3/srtio3 interface", Nature communications **2**, 188 (2011).

[108]K. Han, N Palina, S. W Zeng, Z. Huang, C. J Li, W. X Zhou, D. Y Wan, L. C Zhang, X. Chi, and R. Guo, "Controlling kondo-like scattering at the srtio3-based interfaces:" Scientific Reports **6**, 25455 (2016).

[109]D. Dikin, M Mehta, C. Bark, C. Folkman, C. Eom, and V Chandrasekhar, "Coexistence of superconductivity and ferromagnetism in two dimensions", Physical Review Letters **107**, 056802 (2011).

[110]M. Mehta, D. Dikin, C. W. Bark, C. Folkman, C.-B. Eom, and V. Chandrasekhar, "Hysteretic magneto-resistance at the laalo3-srtio3 interface-interplay between superconducting and ferromagnetic properties", in Aps meeting abstracts (2011).

[111]K. Michaeli, A. C. Potter, and P. A. Lee, "Superconducting and ferromagnetic phases in srtio 3/laalo 3 oxide interface structures: possibility of finite momentum pairing", Physical review letters **108**, 117003 (2012).

[112]Y. Nakamura and Y. Yanase, "Multi-orbital superconductivity in $SrTiO_3$/$LaAlO_3$ interface and $SrTiO_3$ surface", Journal of the Physical Society of Japan **82**, 083705 (2013).

[113]J. A. Bert, B. Kalisky, C. Bell, M. Kim, Y. Hikita, H. Y. Hwang, and K. A. Moler, "Direct imaging of the coexistence of ferromagnetism and superconductivity at the laalo3/srtio3 interface", Nature Physics **7**, 2079 (2011).

[114]M. Lee, J. Williams, S. Zhang, C. D. Frisbie, and D Goldhaber-Gordon, "Electrolyte gate-controlled kondo effect in srtio 3", Physical review letters **107**, 256601 (2011).

[115]G. Liu, J Qiu, Y. Jiang, R Zhao, J. Yao, M Zhao, Y Feng, and J Gao, "Light induced suppression of kondo effect at amorphous laalo3/srtio3 interface", Applied Physics Letters **109**, 031110 (2016).

[116]M. B. Shalom, C. Tai, Y Lereah, M Sachs, E Levy, D Rakhmilevitch, A Palevski, and Y Dagan, "Anisotropic magnetotransport at the srtio 3/laalo 3 interface", Physical Review B **80**, 140403 (2009).

[117]A. Fête, S. Gariglio, A. Caviglia, J.-M. Triscone, and M Gabay, "Rashba induced magnetoconductance oscillations in the laalo 3-srtio 3 heterostructure", Physical Review B **86**, 201105 (2012).

[118]M Diez, A. Monteiro, G Mattoni, E Cobanera, T Hyart, E Mulazimoglu, N Bovenzi, C. Beenakker, and A. Caviglia, "Giant negative magnetoresistance driven by spin-orbit coupling at the laalo 3/srtio 3 interface", Physical review letters **115**, 016803 (2015).

[119]M. Yang, K. Han, O. Torresin, M. Pierre, S. Zeng, Z. Huang, T. Venkatesan, M. Goiran, J. Coey, Ariando, et al., "High field magneto-transport in two-dimensional electron gas laalo3/srtio3", Applied Physics Letters **109**, 122106 (2016).

[120]B. Kalisky, E. M. Spanton, H. Noad, J. R. Kirtley, K. C. Nowack, C. Bell, H. K. Sato, M. Hosoda, Y. Xie, Y. Hikita, et al., "Locally enhanced conductivity due to the tetragonal domain structure in laalo3/srtio3 heterointerfaces", Nature Materials **12**, 1091–1095 (2013).

[121]A. Caviglia, S. Gariglio, N. Reyren, D. Jaccard, T Schneider, M Gabay, S Thiel, G Hammerl, J. Mannhart, and J.-M. Triscone, "Electric field control of the laalo3/srtio3 interface ground state", Nature **456**, 624–627 (2008).

[122]C. Koonce, M. L. Cohen, J. Schooley, W. Hosler, and E. Pfeiffer, "Superconducting transition temperatures of semiconducting srti o 3", Physical Review **163**, 380 (1967).

[123]G Binnig, A Baratoff, H. Hoenig, and J. Bednorz, "Two-band superconductivity in nb-doped srti o 3", Physical Review Letters **45**, 1352 (1980).

[124]D. Van Der Marel, J. L. M. van Mechelen, and I. Mazin, "Common fermi-liquid origin of t 2 resistivity and superconductivity in n-type srtio 3", Physical Review B **84**, 205111 (2011).

[125]X. Lin, B. Fauqué, and K. Behnia, "Scalable t2 resistivity in a small single-component fermi surface", Science **349**, 945–948 (2015).

[126]E. Mikheev, S. Raghavan, J. Y. Zhang, P. B. Marshall, A. P. Kajdos, L. Balents, and S. Stemmer, "Carrier density independent scattering rate in srtio3-based electron liquids", Scientific reports **6** (2016).

[127]M. Swift and C. G. Van de Walle, "Conditions for T^2 resistivity from electron-electron scattering", arXiv preprint arXiv:1701.04744 (2017).

[128]E. Mikheev, B. Himmetoglu, A. P. Kajdos, P. Moetakef, T. A. Cain, C. G. Van de Walle, and S. Stemmer, "Limitations to the room temperature mobility of two-and three-dimensional electron liquids in srtio3", Applied Physics Letters **106**, 062102 (2015).

[129]C Cancellieri, A. Mishchenko, U Aschauer, A Filippetti, C Faber, O. Barišić, V. Rogalev, T Schmitt, N Nagaosa, and V. Strocov, "Polaronic metal state at the $LaAlO_3/SrTiO_3$ interface", Nature communications **7** (2016).

[130]S. Saraf, M. Markovich, and A. Rothschild, "Defect chemistry of p n junctions in complex oxides", Physical Review B **82**, 245208 (2010).

[131]B. F, H. M, R. S, L. H, B. CW, E. CB, I. P, and L. J, "Room-temperature electronically-controlled ferromagnetism at the $LaAlO_3/SrTiO_3$ interface", Nature Communications **5**, 5019 (2014).

[132]A. Caviglia, M Gabay, S. Gariglio, N. Reyren, C. Cancellieri, and J.-M. Triscone, "Tunable rashba spin-orbit interaction at oxide interfaces", Physical review letters **104**, 126803 (2010).

[133]D. Stornaiuolo, S. Gariglio, A. Fête, M Gabay, D. Li, D Massarotti, and J.-M. Triscone, "Weak localization and spin-orbit interaction in side-gate field effect devices at the laalo 3/srtio 3 interface", Physical Review B **90**, 235426 (2014).

[134]D Stornaiuolo, C Cantoni, G. De Luca, R Di Capua, E Di Gennaro, G Ghiringhelli, B. Jouault, D Marrè, D Massarotti, F. M. Granozio, et al., "Tunable spin polarization and superconductivity in engineered oxide interfaces", Nature materials **15**, 278 (2016).

[135]M. B. Shalom, M Sachs, D Rakhmilevitch, A Palevski, and Y Dagan, "Tuning spin-orbit coupling and superconductivity at the srtio 3/laalo 3 interface: a magnetotransport study", Physical review letters **104**, 126802 (2010).

[136]G. Herranz, G. Singh, N. Bergeal, A. Jouan, J. Lesueur, J. Gázquez, M. Varela, M. Scigaj, N. Dix, F. Sánchez, et al., "Engineering two-dimensional superconductivity and rashba spin–orbit coupling in laalo3/srtio3 quantum wells by selective orbital occupancy", Nature communications **6** (2015).

[137]H. Lichte, "Optimum focus for taking electron holograms", Ultramicroscopy **38**, 13–22 (1991).

[138]O Scherzer, "The theoretical resolution limit of the electron microscope", Journal of Applied Physics **20**, 20–29 (1949).

[139]O. Scherzer, "Über einige fehler von elektronenlinsen", Zeitschrift für Physik A Hadrons and Nuclei **101**, 593–603 (1936).

[140]M. Haider, S. Uhlemann, E. Schwan, H. Rose, B. Kabius, and K. Urban, "Electron microscopy image enhanced", Nature **392**, 768 (1998).

[141]M Lentzen, B Jahnen, C. Jia, A Thust, K Tillmann, and K Urban, "High-resolution imaging with an aberration-corrected transmission electron microscope", Ultramicroscopy **92**, 233–242 (2002).

[142]K. W. Urban, C.-L. Jia, L. Houben, M. Lentzen, S.-B. Mi, and K. Tillmann, "Negative spherical aberration ultrahigh-resolution imaging in corrected transmission electron microscopy", Philosophical Transactions of the Royal Society of London A: Mathematical, Physical and Engineering Sciences **367**, 3735–3753 (2009).

[143]C. Jia, M Lentzen, and K Urban, "Atomic-resolution imaging of oxygen in perovskite ceramics", Science **299**, 870–873 (2003).

[144]S. J. Pennycook, F Bassani, G. Leidl, and P Wyder, "Encyclopedia of condensed matter physics (6 volume set)", MRS BULLETIN **31**, 240–247 (2006).

[145]S. Pennycook and P. Nellist, *Scanning transmission electron microscopy: imaging and analysis* (Springer New York, 2011).

[146]S. Findlay, N Shibata, H Sawada, E Okunishi, Y Kondo, and Y Ikuhara, "Dynamics of annular bright field imaging in scanning transmission electron microscopy", Ultramicroscopy **110**, 903–923 (2010).

[147]H Rose, "Phase contrast in scanning transmission electron microscopy", Optik **39**, 416–436 (1974).

[148]T. Komoda, "Electron microscopic observation of crystal lattices on the level with atomic dimension", Japanese Journal of Applied Physics **5**, 603 (1966).

[149]R. Ishikawa, E. Okunishi, H. Sawada, Y. Kondo, F. Hosokawa, and E. Abe, "Direct imaging of hydrogen-atom columns in a crystal by annular bright-field electron microscopy", Nature materials **10**, 278 (2011).

[150]J. M. Cowley, "Image contrast in a transmission scanning electron microscope", Applied Physics Letters **15**, 58–59 (1969).

[151]E Zeitler and M. Thomson, "Scanning transmission electron microscopy. 2.", Optik **31**, 359–+ (1970).

[152]T. Aoki, J. Lu, M. R. McCartney, and D. J. Smith, "Bright-field imaging of compound semiconductors using aberration-corrected scanning transmission electron microscopy", Semiconductor Science and Technology **31**, 094002 (2016).

[153]X. Peirong, E. J. Kirkland, J. Silcox, and R. Keyse, "High-resolution imaging of silicon (111) using a 100 kev stem", Ultramicroscopy **32**, 93–102 (1990).

[154]K Watanabe, Y Kikuchi, T Yamazaki, E Asano, N Nakanishi, Y Kotaka, E Okunishi, and I Hashimoto, "Lattice imaging in low-angle and high-angle bright-field scanning transmission electron microscopy", Acta Crystallographica Section A: Foundations of Crystallography **60**, 591–597 (2004).

[155]J. Sharp, J. Barnard, K Kaneko, K Higashida, and P. Midgley, "Dislocation tomography made easy: a reconstruction from adf stem images obtained using automated image shift correction", in Journal of physics: conference series, Vol. 126, 1 (IOP Publishing, 2008), p. 012013.

[156]D. A. Muller, N. Nakagawa, A. Ohtomo, J. L. Grazul, and H. Y. Hwang, "Atomic-scale imaging of nanoengineered oxygen vacancy profiles in $SrTiO_3$", Nature **430**, 657–661 (2004).

[157]S. Hillyard and J. Silcox, "Detector geometry, thermal diffuse scattering and strain effects in adf stem imaging", Ultramicroscopy **58**, 6–17 (1995).

[158]D. Perovic, C. Rossouw, and A Howie, "Imaging elastic strains in high-angle annular dark field scanning transmission electron microscopy", Ultramicroscopy **52**, 353–359 (1993).

[159]P. J. Phillips, M De Graef, L. Kovarik, A Agrawal, W Windl, and M. Mills, "Atomic-resolution defect contrast in low angle annular dark-field stem", Ultramicroscopy **116**, 47–55 (2012).

[160]A. C. Johnston-Peck, J. P. Winterstein, A. D. Roberts, J. S. DuChene, K. Qian, B. C. Sweeny, W. D. Wei, R. Sharma, E. A. Stach, and A. A. Herzing, "Oxidation-state sensitive imaging of cerium dioxide by atomic-resolution low-angle annular dark field scanning transmission electron microscopy", Ultramicroscopy **162**, 52–60 (2016).

[161]Z. Yu, D. A. Muller, and J. Silcox, "Study of strain fields at a-si/c-si interface", Journal of Applied Physics **95**, 3362–3371 (2004).

[162]W Hoppe, R Langer, G Knesch, and C. Poppe, "Protein-kristallstrukturanalyse mit elektronenstrahlen", Naturwissenschaften **55**, 333–336 (1968).

[163]S. Pennycook and D. Jesson, "High-resolution z-contrast imaging of crystals", Ultramicroscopy **37**, 14–38 (1991).

[164]S. Pennycook and D. Jesson, "High-resolution incoherent imaging of crystals", Physical Review Letters **64**, 938 (1990).

[165]A Howie, "Image contrast and localized signal selection techniques", Journal of Microscopy **117**, 11–23 (1979).

[166]E. J. Kirkland, R. F. Loane, and J. Silcox, "Simulation of annular dark field stem images using a modified multislice method", Ultramicroscopy **23**, 77–96 (1987).

[167]C Dwyer and J Etheridge, "Scattering of å-scale electron probes in silicon", Ultramicroscopy **96**, 343–360 (2003).

[168]D. G. Rickerby, G. Valdrè, and U. Valdrè, *Impact of electron and scanning probe microscopy on materials research*, Vol. 364 (Springer Science & Business Media, 2012), pp. 161–207.

[169]Z Yu, D. Muller, and J Silcox, "Effects of specimen tilt in adf-stem imaging of a-si/c-si interfaces", Ultramicroscopy **108**, 494–501 (2008).

[170]L Fitting, S Thiel, A Schmehl, J Mannhart, and D. Muller, "Subtleties in adf imaging and spatially resolved eels: a case study of low-angle twist boundaries in srtio 3", Ultramicroscopy **106**, 1053–1061 (2006).

[171]M Haruta, H Kurata, H Komatsu, Y Shimakawa, and S Isoda, "Effects of electron channeling in haadf-stem intensity in la 2 cusno 6", Ultramicroscopy **109**, 361–367 (2009).

[172]D. Williams and C. Carter, *Transmission electron microscopy: a textbook for materials science*, Cambridge library collection v. 2 (Springer, 2009).

[173]J. Hwang, J. Y. Zhang, A. J. D'Alfonso, L. J. Allen, and S. Stemmer, "Three-dimensional imaging of individual dopant atoms in srtio 3", Physical review letters **111**, 266101 (2013).

[174]C. Jia, S. Mi, J Barthel, D. Wang, R. Dunin-Borkowski, K. Urban, and A Thust, "Determination of the 3d shape of a nanoscale crystal with atomic resolution from a single image", Nature materials **13**, 1044–1049 (2014).

[175]M. Hÿtch and W. Stobbs, "Quantitative comparison of high resolution tem images with image simulations", Ultramicroscopy **53**, 191–203 (1994).

[176]J. Shao, *Mathematical statistics*, Springer Texts in Statistics (Springer New York, 2008).

[177]V. Voinov, *Unbiased estimators and their applications: volume 1: univariate case* ().

[178]C. M. Anderson, G. N. Georgiou, I. Morrison, G. Stevenson, and R. J. Cherry, "Tracking of cell surface receptors by fluorescence digital imaging microscopy using a charge-coupled device camera. low-density lipoprotein and influenza virus receptor mobility at 4 degrees c", Journal of cell science **101**, 415–425 (1992).

[179]L Houben, A Thust, and K Urban, "Atomic-precision determination of the reconstruction of a 90° tilt boundary in yba2cu3o7-δ by aberration corrected hrtem", Ultramicroscopy **106**, 200–214 (2006).

[180]S. M. Anthony and S. Granick, "Image analysis with rapid and accurate two-dimensional gaussian fitting", Langmuir **25**, 8152–8160 (2009).

[181]S. Tang, Z. Zhou, X. Guo, and Y. Xiao, "Improved iteration centroid algorithm based on linear ccd light-spot location", in Electronic measurement & instruments, 2009. icemi'09. 9th international conference on (IEEE, 2009), pp. 4–438.

[182]B. M. Quine, V. Tarasyuk, H. Mebrahtu, and R. Hornsey, "Determining star-image location: a new sub-pixel interpolation technique to process image centroids", Computer Physics Communications **177**, 700–706 (2007).

[183]M. K. Cheezum, W. F. Walker, and W. H. Guilford, "Quantitative comparison of algorithms for tracking single fluorescent particles", Biophysical journal **81**, 2378–2388 (2001).

[184]E. Völkl, L. Allard, and D. Joy, *Introduction to electron holography* (Springer US, 2013).

[185]M. McCartney, D. J. Smith, R. Hull, J. Bean, E Voelkl, and B Frost, "Direct observation of potential distribution across si/si p-n junctions using off-axis electron holography", Applied physics letters **65**, 2603–2605 (1994).

[186]R. E. Dunin-Borkowski, M. R. McCartney, R. B. Frankel, D. A. Bazylinski, M. Pósfai, and P. R. Buseck, "Magnetic microstructure of magnetotactic bacteria by electron holography", Science **282**, 1868–1870 (1998).

[187]M. McCartney, F. Ponce, J. Cai, and D. Bour, "Mapping electrostatic potential across an algan/ingan/algan diode by electron holography", Applied Physics Letters **76**, 3055–3057 (2000).

[188]L. Zhou, D. A. Cullen, D. Smith, M. R. McCartney, A. Mouti, M. Gonschorek, E. Feltin, J.-F. Carlin, N. Grandjean, et al., "Polarization field mapping of $Al_{0.85}In_{0.15}N$/AlN/GaN heterostructure", Applied Physics Letters **94**, 121909–121909 (2009).

[189]D. Saldin and J. Spence, "On the mean inner potential in high-and low-energy electron diffraction", Ultramicroscopy **55**, 397–406 (1994).

[190]M O'Keeffe and J. Spence, "On the average coulomb potential Φ_0 and constraints on the electron density in crystals", Acta Crystallographica Section A: Foundations of Crystallography **50**, 33–45 (1994).

[191]R. S. Pennington, J. J. Mortensen, T. Kasama, C. Boothroyd, and R. E. Dunin-Borkowski, "Theoretical and experimental factors affecting measurements of semiconductor mean inner potentials", in Journal of physics: conference series, Vol. 209, 1 (IOP Publishing, 2010), p. 012030.

[192]R. S. Pennington, "Factors influencing mean inner potentials as studied using electron holography and density functional theory", PhD thesis (Technical University of Denmark, 2012).

[193]P Schattschneider, M Nelhiebel, and B Jouffrey, "Density matrix of inelastically scattered fast electrons", Physical Review B **59**, 10959 (1999).

[194]D. A. Muller, D. J. Singh, and J. Silcox, "Connections between the electron-energy-loss spectra, the local electronic structure, and the physical properties of a material: a study of nickel aluminum alloys", Physical Review B **57**, 8181 (1998).

[195]R. Egerton, *Electron energy-loss spectroscopy in the electron microscope*, SpringerLink : Bücher (Springer US, 2011).

[196]H. L. Xin, C. Dwyer, and D. A. Muller, "Is there a stobbs factor in atomic-resolution stem-eels mapping?", Ultramicroscopy **139**, 38–46 (2014).

[197]E Stoyanov, F Langenhorst, and G Steinle-Neumann, "The effect of valence state and site geometry on Ti $L_{3,2}$ and O K electron energy-loss spectra of Ti_xO_y phases", American Mineralogist **92**, 577–586 (2007).

[198]F. De Groot, J. Fuggle, B. Thole, and G. Sawatzky, "L 2, 3 x-ray-absorption edges of d 0 compounds: k+, ca 2+, sc 3+, and ti 4+ in o h (octahedral) symmetry", Physical Review B **41**, 928 (1990).

[199]F. De Groot, J. Fuggle, B. Thole, and G. Sawatzky, "2p x-ray absorption of 3d transition-metal compounds: an atomic multiplet description including the crystal field", Physical Review B **42**, 5459 (1990).

[200]J. Zhang, "Application of electron energy-loss spectroscopy to ferroelectric thin films", PhD thesis (Dissertation, Martin-Luther Universität Halle-Wittenberg, 2004).

[201]F. De Groot, M Grioni, J. Fuggle, J Ghijsen, G. Sawatzky, and H Petersen, "Oxygen 1s x-ray-absorption edges of transition-metal oxides", Physical Review B **40**, 5715 (1989).

[202]M. Yoshiya, I. Tanaka, K. Kaneko, and H. Adachi, "First principles calculation of chemical shifts in elnes/nexafs of titanium oxides", Journal of Physics: Condensed Matter **11**, 3217 (1999).

[203]H Kurata, E Lefevre, C Colliex, and R Brydson, "Electron-energy-loss near-edge structures in the oxygen k-edge spectra of transition-metal oxides", Physical Review B **47**, 13763 (1993).

[204]F. De Groot, J. Faber, J. Michiels, M. Czyżyk, M Abbate, and J. Fuggle, "Oxygen 1s x-ray absorption of tetravalent titanium oxides: a comparison with single-particle calculations", Physical Review B **48**, 2074 (1993).

[205]C. Chang, *Hyperspectral data processing: algorithm design and analysis* (Wiley, 2013).

[206]F. A. Kruse et al., "Comparison of aviris and hyperion for hyperspectral mineral mapping", in 11th jpl airborne geoscience workshop, Vol. 4, 8 (2002).

[207]W. M. Porter and H. T. Enmark, "A system overview of the airborne visible/infrared imaging spectrometer (aviris)", (1987).

[208]J. M. Bioucas-Dias, A. Plaza, N. Dobigeon, M. Parente, Q. Du, P. Gader, and J. Chanussot, "Hyperspectral unmixing overview: geometrical, statistical, and sparse regression-based approaches", IEEE journal of selected topics in applied earth observations and remote sensing **5**, 354–379 (2012).

[209]M. E. Winter, "N-findr: an algorithm for fast autonomous spectral end-member determination in hyperspectral data", in Spie's international symposium on optical science, engineering, and instrumentation (International Society for Optics and Photonics, 1999), pp. 266–275.

[210]R. E. Kalman et al., "A new approach to linear filtering and prediction problems", Journal of basic Engineering **82**, 35–45 (1960).

[211]P. Trebbia and N. Bonnet, "Eels elemental mapping with unconventional methods i. theoretical basis: image analysis with multivariate statistics and entropy concepts", Ultramicroscopy **34**, 165–178 (1990).

[212]M. R. Keenan and P. G. Kotula, "Accounting for poisson noise in the multivariate analysis of tof-sims spectrum images", Surface and Interface Analysis **36**, 203–212 (2004).

[213]F. B. Lavoie, N. Braidy, and R. Gosselin, "Including noise characteristics in mcr to improve mapping and component extraction from spectral images", Chemometrics and Intelligent Laboratory Systems **153**, 40–50 (2016).

[214]J. M. Nascimento and J. M. Dias, "Vertex component analysis: a fast algorithm to unmix hyperspectral data", IEEE transactions on Geoscience and Remote Sensing **43**, 898–910 (2005).

[215]N. S. Altman, "An introduction to kernel and nearest-neighbor nonparametric regression", The American Statistician **46**, 175–185 (1992).

[216]F. Jackson, "Polytopes in euclidean n-space", Bulletin of the Institute of Mathematics and Its Applications **29**, 172–173 (1993).

[217]J Hafner, *Ab-initio simulations in materials science*, 2008.

[218]P. Hohenberg and W. Kohn, "Inhomogeneous electron gas", Physical review **136**, B864 (1964).

[219]J Hafner, "Foundations of density-functional theory", Center for Computational Materials Science, Wien, Austria (2003).

[220]R. HIRSCHL, "Dft in depth the exchange-correlation term",

[221]J. P. Perdew, J. Chevary, S. Vosko, K. A. Jackson, M. R. Pederson, D. Singh, and C. Fiolhais, "Atoms, molecules, solids, and surfaces: applications of the generalized gradient approximation for exchange and correlation", Physical Review B **46**, 6671 (1992).

[222]J. P. Perdew, K. Burke, and M. Ernzerhof, "Generalized gradient approximation made simple", Physical review letters **77**, 3865–3868 (1996).

[223]A. Roldán, J. M. Ricart, and F. Illas, "Influence of the exchange–correlation potential on the description of the molecular mechanism of oxygen dissociation by au nanoparticles", Theoretical Chemistry Accounts **123**, 119–126 (2009).

[224]L. Bollmann, "Density functional theory study of the thermodynamics of catalytic remediation of nitrate in water", (2014).

[225]R. Martin, *Electronic structure: basic theory and practical methods* (Cambridge University Press, 2004).

[226]G. K. Madsen, P. Blaha, K. Schwarz, E. Sjöstedt, and L. Nordström, "Efficient linearization of the augmented plane-wave method", Physical Review B **64**, 195134 (2001).

[227]P. Blaha, K. Schwarz, G. Madsen, D. Kvasnicka, and J. Luitz, "Wien2k", An augmented plane wave+ local orbitals program for calculating crystal properties (2001).

[228]K. Dewhurst, S. Sharma, L Nordstrom, F Cricchio, F Bultmark, H Gross, C Ambrosch-Draxl, C Persson, C Brouder, R Armiento, et al., "The elk fp-lapw code", ELK, http://elk. sourceforge. net (2016).

[229]N. Troullier and J. L. Martins, "Efficient pseudopotentials for plane-wave calculations", Physical review B **43**, 1993 (1991).

[230]A. M. Rappe, K. M. Rabe, E. Kaxiras, and J. Joannopoulos, "Optimized pseudopotentials", Physical Review B **41**, 1227 (1990).

[231]G Kresse and J Furhmuller, "Software vasp, vienna (1999); g. kresse, j. hafner", Phys. Rev. B **47**, R558 (1993).

[232]P. Giannozzi, S. Baroni, N. Bonini, M. Calandra, R. Car, C. Cavazzoni, D. Ceresoli, G. L. Chiarotti, M. Cococcioni, I. Dabo, et al., "Quantum espresso: a modular and open-source software project for quantum simulations of materials", Journal of physics: Condensed matter **21**, 395502 (2009).

[233]K. F. Garrity, J. W. Bennett, K. M. Rabe, and D. Vanderbilt, "Pseudopotentials for high-throughput dft calculations", Computational Materials Science **81**, 446–452 (2014).

[234]A. Jain, G. Hautier, C. J. Moore, S. P. Ong, C. C. Fischer, T. Mueller, K. A. Persson, and G. Ceder, "A high-throughput infrastructure for density functional theory calculations", Computational Materials Science **50**, 2295–2310 (2011).

[235]I. Castelli et al., "Standard solid state pseudopotentials (sssp)", http://materialscloud.org/sssp/.

[236]A. D. Becke, "A new mixing of hartree–fock and local density-functional theories", The Journal of chemical physics **98**, 1372–1377 (1993).

[237]P. Stephens, F. Devlin, C. Chabalowski, and M. J. Frisch, "Ab initio calculation of vibrational absorption and circular dichroism spectra using density functional force fields", The Journal of Physical Chemistry **98**, 11623–11627 (1994).

[238]J. P. Perdew, M. Ernzerhof, and K. Burke, "Rationale for mixing exact exchange with density functional approximations", The Journal of Chemical Physics **105**, 9982–9985 (1996).

[239]J. Heyd, G. E. Scuseria, and M. Ernzerhof, "Hybrid functionals based on a screened coulomb potential", The Journal of Chemical Physics **118**, 8207–8215 (2003).

[240]S. Dudarev, G. Botton, S. Savrasov, C. Humphreys, and A. Sutton, "Electron-energy-loss spectra and the structural stability of nickel oxide: an lsda+ u study", Physical Review B **57**, 1505 (1998).

[241]J. M. Cowley, *Diffraction physics* (Elsevier, 1995).

[242]J Barthel, *Dr. probe-stem simulation software*, 2013.

[243]A. Rosenauer, M. Schowalter, J. T. Titantah, and D. Lamoen, "An emission-potential multislice approximation to simulate thermal diffuse scattering in high-resolution transmission electron microscopy", Ultramicroscopy **108**, 1504–1513 (2008).

[244]C Dwyer, R Erni, and J Etheridge, "Measurement of effective source distribution and its importance for quantitative interpretation of stem images", Ultramicroscopy **110**, 952–957 (2010).

[245]R. F. Loane, P. Xu, and J. Silcox, "Thermal vibrations in convergent-beam electron diffraction", Acta Crystallographica Section A: Foundations of Crystallography **47**, 267–278 (1991).

[246]A Uldry, F Vernay, and B Delley, "Systematic computation of crystal-field multiplets for x-ray core spectroscopies", Physical Review B **85**, 125133 (2012).

[247]M Schowalter, D Lamoen, A Rosenauer, P Kruse, and D Gerthsen, "First-principles calculations of the mean inner coulomb potential for sphalerite type ii–vi semiconductors", Applied physics letters **85**, 4938–4940 (2004).

[248]PhD thesis ().

[249]R. M. Pick, M. H. Cohen, and R. M. Martin, "Microscopic theory of force constants in the adiabatic approximation", Physical Review B **1**, 910 (1970).

[250]M. V. Berry, "Quantal phase factors accompanying adiabatic changes", in Proceedings of the royal society of london a: mathematical, physical and engineering sciences, Vol. 392, 1802 (The Royal Society, 1984), pp. 45–57.

[251]R. Resta, "Theory of the electric polarization in crystals", Ferroelectrics **136**, 51–55 (1992).

[252]G Kresse and O Lebacq, "Vasp manual", http://cms.mpi.univie.ac.at/vasp/vasp.pdf. Retrieved April **22** (2013).

[253]R. King-Smith and D. Vanderbilt, "Theory of polarization of crystalline solids", Physical Review B **47**, 1651 (1993).

[254]O. Diéguez, S. Tinte, A Antons, C. Bungaro, J. Neaton, K. M. Rabe, and D. Vanderbilt, "Ab initio study of the phase diagram of epitaxial batio 3", Physical Review B **69**, 212101 (2004).

[255]A. Antons, J. Neaton, K. M. Rabe, and D. Vanderbilt, "Tunability of the dielectric response of epitaxially strained srti o 3 from first principles", Physical Review B **71**, 024102 (2005).

[256]O. Diéguez, K. M. Rabe, and D. Vanderbilt, "First-principles study of epitaxial strain in perovskites", Physical Review B **72**, 144101 (2005).

[257]S. Lu, K. J. Kormondy, T. Q. Ngo, T. Aoki, A. Posadas, J. G. Ekerdt, A. A. Demkov, M. R. McCartney, and D. J. Smith, "Spectrum and phase mapping across the epitaxial γ-Al_2O_3/$SrTiO_3$ interface", Applied Physics Letters **108**, 051606 (2016).

[258]M. R. McCartney and D. J. Smith, "Electron holography: phase imaging with nanometer resolution", Annu. Rev. Mater. Res. **37**, 729–767 (2007).

[259]L. Reimer, "Energy-filtering transmission electron microscopy", Advances in electronics and electron physics **81**, 43–126 (1991).

[260]W.-Y. Ching, L. Ouyang, P. Rulis, and H. Yao, "Ab initio study of the physical properties of γ-Al_2O_3: lattice dynamics, bulk properties, electronic structure, bonding, optical properties, and elnes/xanes spectra", Physical Review B **78**, 014106 (2008).

[261]J. Yang, E Schumann, H Müllejans, and M Rühle, "Chemistry and bonding investigations of interfaces", Journal of Physics D: Applied Physics **29**, 1716 (1996).

[262]N. Mott and E. Davis, *Electronic processes in non-crystalline materials*, Oxford Classic Texts in the Physical Sciences (OUP Oxford, 2012).

[263]N. Mott, "Conduction in non-crystalline materials: iii. localized states in a pseudogap and near extremities of conduction and valence bands", Philosophical Magazine **19**, 835–852 (1969).

[264]V. Y. Butko, J. DiTusa, and P. Adams, "Coulomb gap: how a metal film becomes an insulator", Physical review letters **84**, 1543 (2000).

[265]W. Baber, "The contribution to the electrical resistance of metals from collisions between electrons", Proc. R. Soc. Lond. A **158**, 383–396 (1937).

[266]S. Klimin, J Tempere, D. van der Marel, and J. Devreese, "Microscopic mechanisms for the fermi-liquid behavior of nb-doped strontium titanate", Physical Review B **86**, 045113 (2012).

[267]B. Van Zeghbroeck, "Principles of semiconductor devices", Colarado University (2004).

[268]F Bloch, "Zum elektrischen widerstandsgesetz bei tiefen temperaturen", Zeitschrift für Physik **59**, 208–214 (1930).

[269]E Grüneisen, "Die abhängigkeit des elektrischen widerstandes reiner metalle von der temperatur", Annalen der Physik **408**, 530–540 (1933).

[270]C. Kittel, *Introduction to solid state physics* (Wiley, 2004).

[271]S. Sze and K. Ng, *Physics of semiconductor devices* (Wiley, 2006).

[272]M Nakamura, F Kagawa, T Tanigaki, H. Park, T Matsuda, D Shindo, Y Tokura, and M Kawasaki, "Spontaneous polarization and bulk photovoltaic effect driven by polar discontinuity in $LaFeO_3/SrTiO_3$ heterojunctions", Physical review letters **116**, 156801 (2016).

[273]P. Rez, "Inner-shell spectroscopy: an atomic view", Ultramicroscopy **28**, 16–23 (1989).

[274]Y. Cao, X. Liu, P. Shafer, S. Middey, D. Meyers, M. Kareev, Z. Zhong, J.-W. Kim, P. J. Ryan, E. Arenholz, et al., "Anomalous orbital structure in a spinel–perovskite interface", npj Quantum Materials **1**, 16009 (2016).

[275]H. Hwang, A Ohtomo, N Nakagawa, D. Muller, and J. Grazul, "High-mobility electrons in srtio3 heterostructures", Physica E: Low-dimensional Systems and Nanostructures **22**, 712–716 (2004).

[276]A Ohtomo, D. Muller, J. Grazul, and H. Hwang, "Epitaxial growth and electronic structure of latio x films", Applied Physics Letters **80**, 3922–3924 (2002).

[277]B. Matthias, R. Bozorth, and J. Van Vleck, "Ferromagnetic interaction in euo", Physical Review Letters **7**, 160 (1961).

[278]T. McGuire, B. Argyle, M. Shafer, and J. Smart, "Ferromagnetism in divalent europium salts", Applied Physics Letters **1**, 17–18 (1962).

[279]A Mauger and C Godart, "The magnetic, optical, and transport properties of representatives of a class of magnetic semiconductors: the europium chalcogenides", Physics Reports **141**, 51–176 (1986).

[280]A. Schmehl, V. Vaithyanathan, A. Herrnberger, S. Thiel, C. Richter, M. Liberati, T. Heeg, M. Röckerath, L. F. Kourkoutis, S. Mühlbauer, et al., "Epitaxial integration of the highly spin-polarized ferromagnetic semiconductor euo with silicon and gan", Nature materials **6**, 882 (2007).

[281]C Caspers, M Müller, A. Gray, A. Kaiser, A Gloskovskii, C. Fadley, W Drube, and C. Schneider, "Electronic structure of euo spin filter tunnel contacts directly on silicon", physica status solidi (RRL)-Rapid Research Letters **5**, 441–443 (2011).

[282]R Sutarto, S. Altendorf, B Coloru, M. M. Sala, T Haupricht, C. Chang, Z Hu, C Schüßler-Langeheine, N Hollmann, H Kierspel, et al., "Epitaxy, stoichiometry, and magnetic properties of gd-doped euo films on ysz (001)", Physical Review B **80**, 085308 (2009).

[283]Y. Wang, M. K. Niranjan, J. D. Burton, J. M. An, K. D. Belashchenko, and E. Y. Tsymbal, "Prediction of a spin-polarized two-dimensional electron gas at the laalo 3/euo (001) interface", Physical Review B **79**, 212408 (2009).

[284]J. Lee, N. Sai, and A. A. Demkov, "Spin-polarized two-dimensional electron gas through electrostatic doping in laalo 3/euo heterostructures", Physical Review B **82**, 235305 (2010).

[285]K. Kormondy, L. Gao, X. Li, S. Lu, A. Posadas, S. Shen, M. Tsoi, M. McCartney, D. Smith, J. Zhou, L. Lev, M.-A. Husanu, V. Strocov, and A. Demkov, "Large positive linear magnetoresistance in the two-dimensional t_{2g} electron gas at the $EuO/SrTiO_3$ interface.", Scientific Reports, under revision (2017).

[286]H Miyazaki, H Momiyama, T Hajiri, T Ito, K Imura, M Matsunami, and S Kimura, "Fabrication of single crystalline euo thin film with sro buffer layer on srtio3 substrate", in Journal of physics: conference series, Vol. 391, 1 (IOP Publishing, 2012), p. 012047.

[287]R. Wyckoff, *Crystal structures*, Crystal Structures v. 1 (Wiley, 1963).

[288]T. Mairoser, J. A. Mundy, A. Melville, D. Hodash, P. Cueva, R. Held, A. Glavic, J. Schubert, D. A. Muller, D. G. Schlom, et al., "High-quality euo thin films the easy way via topotactic transformation", Nature communications **6**, 7716 (2015).

[289]J Shieh, J. Yeh, Y. Shu, and J. Yen, "Hysteresis behaviors of barium titanate single crystals based on the operation of multiple 90 switching systems", Materials Science and Engineering: B **161**, 50–54 (2009).

[290]W Cochran, "Crystal stability and the theory of ferroelectricity", Advances in Physics **9**, 387–423 (1960).

[291]R Comes, M Lambert, and A Guinier, "The chain structure of batio3 and knbo3", Solid State Communications **6**, 715–719 (1968).

[292]J. Harada, M. Watanabe, S. Kodera, and G. Honjo, "Diffuse streak diffraction pattern of electron and x-rays due to low frequency optical mode in tetragonal batio3", Journal of the Physical Society of Japan **20**, 630–631 (1965).

[293]K. J. Choi, M Biegalski, Y. Li, A Sharan, J Schubert, R Uecker, P Reiche, Y. Chen, X. Pan, V Gopalan, et al., "Enhancement of ferroelectricity in strained batio3 thin films", Science **306**, 1005–1009 (2004).

[294]C. Ederer and N. A. Spaldin, "Effect of epitaxial strain on the spontaneous polarization of thin film ferroelectrics", Physical review letters **95**, 257601 (2005).

[295]V. Afanasjev, A. Petrov, I. Pronin, E. Tarakanov, E. J. Kaptelov, and J Graul, "Polarization and self-polarization in thin pbzr1-xtixo3 (pzt) films", Journal of Physics: Condensed Matter **13**, 8755 (2001).

[296]C. Jia, S. Mi, K Urban, I Vrejoiu, M Alexe, and D Hesse, "Effect of a single dislocation in a heterostructure layer on the local polarization of a ferroelectric layer", Physical review letters **102**, 117601 (2009).

[297]M. F. Chisholm, W. Luo, M. P. Oxley, S. T. Pantelides, and H. N. Lee, "Atomic-scale compensation phenomena at polar interfaces", Physical review letters **105**, 197602 (2010).

[298]R. Mishra, Y.-M. Kim, J. Salafranca, S. K. Kim, S. H. Chang, A. Bhattacharya, D. D. Fong, S. J. Pennycook, S. T. Pantelides, and A. Y. Borisevich, "Oxygen-vacancy-induced polar behavior in (lafeo3) 2/(srfeo3) superlattices", Nano letters **14**, 2694–2701 (2014).

[299]Q. Qiao, Y. Zhang, R. Contreras-Guerrero, R. Droopad, S. T. Pantelides, S. J. Pennycook, S. Ogut, and R. F. Klie, "Direct observation of oxygen-vacancy-enhanced polarization in a srtio3-buffered ferroelectric batio3 film on gaas", Applied Physics Letters **107**, 201604 (2015).

[300]Y.-H. Chu, M. P. Cruz, C.-H. Yang, L. W. Martin, P.-L. Yang, J.-X. Zhang, K. Lee, P. Yu, L.-Q. Chen, and R. Ramesh, "Domain control in multiferroic bifeo3 through substrate vicinality", Advanced materials **19**, 2662–2666 (2007).

[301]H. W. Jang, D. Ortiz, S.-H. Baek, C. M. Folkman, R. R. Das, P. Shafer, Y. Chen, C. T. Nelson, X. Pan, R. Ramesh, et al., "Domain engineering for enhanced ferroelectric properties of epitaxial (001) bifeo thin films", Advanced materials **21**, 817–823 (2009).

[302]C.-G. Duan, R. F. Sabirianov, W.-N. Mei, S. S. Jaswal, and E. Y. Tsymbal, "Interface effect on ferroelectricity at the nanoscale", Nano letters **6**, 483–487 (2006).

[303]R. Wang, D. Fong, F Jiang, M. Highland, P. Fuoss, C. Thompson, A. Kolpak, J. Eastman, S. Streiffer, A. Rappe, et al., "Reversible chemical switching of a ferroelectric film", Physical review letters **102**, 047601 (2009).

[304]H. Lee, T. H. Kim, J. J. Patzner, H. Lu, J.-W. Lee, H. Zhou, W. Chang, M. K. Mahanthappa, E. Y. Tsymbal, A. Gruverman, et al., "Imprint control of batio3 thin films via chemically induced surface polarization pinning", Nano letters **16**, 2400–2406 (2016).

[305]P Yu, W. Luo, D Yi, J. Zhang, M. Rossell, C.-H. Yang, L You, G Singh-Bhalla, S. Yang, Q He, et al., "Interface control of bulk ferroelectric polarization", Proceedings of the National Academy of Sciences **109**, 9710–9715 (2012).

[306]B. C. Jeon, D. Lee, M. H. Lee, S. M. Yang, S. C. Chae, T. K. Song, S. D. Bu, J.-S. Chung, J.-G. Yoon, and T. W. Noh, "Flexoelectric effect in the reversal of self-polarization and associated changes in the electronic functional properties of bifeo3 thin films", Advanced Materials **25**, 5643–5649 (2013).

[307]R. Guo, L. You, M Motapothula, Z. Zhang, M. B. Breese, L. Chen, D. Wu, and J. Wang, "Influence of target composition and deposition temperature on the domain structure of bifeo3 thin films", AIP Advances **2**, 042104 (2012).

[308]A. Kolpak, F. Walker, J. Reiner, Y Segal, D Su, M. Sawicki, C. Broadbridge, Z Zhang, Y Zhu, C. Ahn, et al., "Interface-induced polarization and inhibition of ferroelectricity in epitaxial srtio 3/si", Physical review letters **105**, 217601 (2010).

[309]H. Wu, S. Lu, T. Aoki, P. Ponath, J. G. Ekerdt, A. A. Demkov, M. R. McCartney, and D. J. Smith, "Integration of ferroelectric batio3 with ge: the role of a srtio3 buffer layer investigated using aberration-corrected stem", Applied Physics Letters **110**, 252901 (2017).

[310]Y Liu, Y. Zhu, Y. Tang, and X. Ma, "An effect of crystal tilt on the determination of ions displacements in perovskite oxides under bf/haadf-stem imaging mode", Journal of Materials Research **32**, 947–956 (2017).

[311]P. Ghosez, X. Gonze, P. Lambin, and J.-P. Michenaud, "Born effective charges of barium titanate: band-by-band decomposition and sensitivity to structural features", Physical Review B **51**, 6765 (1995).

[312]U. Aschauer, R. Pfenninger, S. M. Selbach, T. Grande, and N. A. Spaldin, "Strain-controlled oxygen vacancy formation and ordering in camno 3", Physical Review B **88**, 054111 (2013).

[313]Q Yang, J. Cao, Y Ma, Y. Zhou, L. Jiang, and X. Zhong, "Strain effects on formation and migration energies of oxygen vacancy in perovskite ferroelectrics: a first-principles study", Journal of Applied Physics **113**, 184110 (2013).

[314]S. Shirasaki, H Yamamura, H Haneda, K Kakegawa, and J Moori, "Defect structure and oxygen diffusion in undoped and la-doped polycrystalline barium titanate", The Journal of Chemical Physics **73**, 4640–4645 (1980).

[315]G. Lewis and C. Catlow, "Computer modelling of barium titanate", Radiation Effects **73**, 307–314 (1983).

[316]K. Shimoyama, M. Kiyohara, K. Kubo, A. Uedono, and K. Yamabe, "Epitaxial growth of batio 3/srtio 3 structures on srtio 3 substrate with automatic feeding of oxygen from the substrate", Journal of applied physics **92**, 4625–4630 (2002).

[317]J. Hong, G Catalan, J. Scott, and E Artacho, "The flexoelectricity of barium and strontium titanates from first principles", Journal of Physics: Condensed Matter **22**, 112201 (2010).

[318]R Maranganti and P Sharma, "Atomistic determination of flexoelectric properties of crystalline dielectrics", Physical Review B **80**, 054109 (2009).

[319]Y. Gu, M. Li, A. N. Morozovska, Y. Wang, E. A. Eliseev, V. Gopalan, and L.-Q. Chen, "Flexoelectricity and ferroelectric domain wall structures: phase-field modeling and dft calculations", Physical Review B **89**, 174111 (2014).

[320]W. Ma and L. E. Cross, "Flexoelectricity of barium titanate", Applied Physics Letters **88**, 232902 (2006).

[321]R. Guzmán, L. Maurel, E. Langenberg, A. R. Lupini, P. A. Algarabel, J. A. Pardo, and C. Magén, "Polar-graded multiferroic srmno3 thin films", Nano letters **16**, 2221–2227 (2016).

[322]D. Song, Z. Wang, and J. Zhu, "Effect of the asymmetry of dynamical electron diffraction on intensity of acquired emcd signals", Ultramicroscopy **148**, 42–51 (2015).

[323]J. Yang, D. Zhang, A. F. Frangi, and J.-y. Yang, "Two-dimensional pca: a new approach to appearance-based face representation and recognition", IEEE transactions on pattern analysis and machine intelligence **26**, 131–137 (2004).

[324]A. Thust, J. Barthel, and C.-L. Jia, "Is hrtem image simulation correct? a premise-free calibration approach", Microscopy and Microanalysis **22**, 1390 (2016).

[325]Y. Ma and Y. Fu, *Manifold learning theory and applications* (CRC Press, 2011).

APPENDIX A

JOURNAL PUBLICATIONS DURING PHD RESEARCH

- **Lu, S.**, Kormondy, K.J., Demkov, A.A., and Smith, D.J., (2018). EELS background subtraction algorithm based on subspace division. Ultramicroscopy, submitted.
- Kormondy, K.J., Gao, L., Li, X., **Lu, S.**, Posadas, A.B., Shen, S., Tsoi, M., McCartney, M.R., Smith, D.J., Zhou, J., Lev, L.L., Husanu, M-A., Strocov, V. and Demkov, A.A., (2017). Large positive linear magnetoresistance in the two-dimensional t_{2g} electron gas at the $EuO/SrTiO_3$ interface. Scientific Reports, under revision.
- Smith, D.J., Wu, H., **Lu, S.**, Aoki, T., Ponath, P., Fredrickson, K., McDaniel, M.D., Lin, E., Posadas, A.B., Demkov, A.A. and Ekerdt, J., (2017). Recent studies of oxide-semiconductor heterostructures using aberration-corrected scanning transmission electron microscopy. Journal of Materials Research, 32(5), pp.912-920.
- Wu, H., **Lu, S.**, Aoki, T., Ponath, P., Ekerdt, J.G., Demkov, A.A., McCartney, M.R. and Smith, D.J., 2017. Integration of ferroelectric $BaTiO_3$ with Ge: The role of a $SrTiO_3$ buffer layer investigated using aberration-corrected STEM. Applied Physics Letters, 110(25), p.252901.
- **Lu, S.**, Kormondy, K.J., Ngo, T.Q., Aoki, T., Posadas, A., Ekerdt, J.G., Demkov, A.A., McCartney, M.R. and Smith, D.J., (2016). Spectrum and phase mapping across the epitaxial γ-$Al_2O_3/SrTiO_3$ interface. Applied Physics Letters, 108(5), p.051606.
- Kormondy, K.J., Posadas, A.B., Ngo, T.Q., **Lu, S.**, Goble, N., Jordan-Sweet, J., Gao, X.P., Smith, D.J., McCartney, M.R., Ekerdt, J.G. and Demkov, A.A., (2015). Quasi-two-dimensional electron gas at the epitaxial alumina/$SrTiO_3$ interface: Control of oxygen vacancies. Journal of Applied Physics, 117(9), p.095303.
- Ngo, T.Q., Goble, N.J., Posadas, A., Kormondy, K.J., **Lu, S.**, McDaniel, M.D., Jordan-Sweet, J., Smith, D.J., Gao, X.P., Demkov, A.A. and Ekerdt, J.G., (2015). Quasi-two-dimensional electron gas at the interface of γ-$Al_2O_3/SrTiO_3$ heterostructures grown by atomic layer deposition. Journal of Applied Physics, 118(11), p.115303.
- McDaniel, M.D., Hu, C., **Lu, S.**, Ngo, T.Q., Posadas, A., Jiang, A., Smith, D.J., Yu, E.T., Demkov, A.A. and Ekerdt, J.G., (2015). Atomic layer deposition of crystalline $SrHfO_3$ directly on Ge (001) for high-k dielectric applications. Journal of Applied Physics, 117(5), p.054101.
- McDaniel, M. D., Ngo, T. Q., Posadas, A., Hu, C., **Lu, S.**, Smith, D. J., Yu, E. T., Demkov, A. A. and Ekerdt, J. G. (2014), A Chemical Route to Monolithic Integration of Crystalline Oxides on Semiconductors. Advanced Materials Interfaces, 1(8), 1400081.

APPENDIX B

PUBLISHED CONFERENCE ABSTRACTS DURING PHD STUDY

- **Lu, S.**, Kormondy, K.J., Ngo, T.Q., Ortmann, E., Aoki, T., Posadas, A., Ekerdt, J.G., Demkov, A.A., McCartney, M.R. and Smith, D.J., (2017). ELNES spectrum unmixing and mapping for oxide/oxide interfaces. Microscopy and Microanalysis, 23 (Supp.3), pp.1588-1589
- **Lu, S.**, Kormondy, K.J., Ngo, T.Q., Ortmann, E., Aoki, T., Posadas, A., Ekerdt, J.G., Demkov, A.A., McCartney, M.R. and Smith, D.J., (2016). ELNES analysis of γ-$Al_2O_3/SrTiO_3$ and $LaTiO_3/SrTiO_3$ interfaces. Microscopy and Microanalysis, 22 (Supp.3), p.1660-1661.
- **Lu, S.**, Kormondy, K.J., Ngo, T.Q., Aoki, T., Posadas, A., Ekerdt, J.G., Demkov, A.A., McCartney, M.R. and Smith, D.J., (2015). Characterization of Two-Dimensional Electron Gas at the γ-$Al_2O_3/SrTiO_3$ Interface. Microscopy and Microanalysis, 21 (Supp.3), p.1309-1310.